THE MUTUAL INFLUENCE OF STRAIN FIELDS AND POINT DEFECT DISTRIBUTIONS IN KRYPTON IMPLANTED POLYCRYSTALLINE TITANIUM

Schadrack Nsengiyumva

A dissertation submitted to the Department of Physics of the University of Cape Town in partial fulfilment of the requirements for the degree of Doctor of Philosophy

University of Cape Town
December 2008

Abstract

Stress migration of point and open-volume defects in materials is an important problem in a wide variety of applications, such as degradation of metallic interconnects in semiconductor devices, metal fatigue, and radiation damage profiles in ion implantation and surface modification. From a fundamental research view point, this study aims to contribute to a better understanding of the basic processes underlying the effect of stress assisted diffusion on point defect distributions in metals. The main focus is the study of diffusion of foreign interstitial atoms under stress fields, using Rutherford backscattering to obtain depth profiles, and synchrotron radiation diffraction for the determination of stress fields. This has been achieved by creating a well designed model system of krypton implanted polycrystalline titanium. The particular advantages of this model system are 2-fold: firstly the implantation has been performed at low dose to avoid clustering and larger defect formation, and secondly the choice of inert insoluble species implantation does not bring about any phase change or substitution of the implanted ions into the structure.

The results obtained indicate that both stress induced point defect diffusion and stress relaxation take place during krypton implantation of polycrystalline titanium. This was found to be comparable to other insoluble species in metals. Stress induced point defect diffusion was observed at low fluence, whereas stress relaxation takes place at high fluence. The change in krypton range was found to correlate with the stress gradient, allowing its mobility to be estimated. At low fluence, implantation also introduces a new source of tensile stress, whose origin might be the presence of point and open volume defects. At high fluences, stress relaxation is observed.

Acknowledgements

I would like to express my gratitude to my supervisors Prof. Margit Härting and Prof. David Thomas Britton for their guidance, support, and constant encouragement throughout my PhD programme. This work would not have been achieved without their dedication, time and energy. During the past years I have learnt a lot from their broad experience and expertise in research.

I would like to thank Prof. Craig Comrie, Chris Theron, and all the technicians at the Materials Research Group (iThemba LABS) for their assistance with RBS, Mira Topic for her assistance with microscopy, Tshepo Ntsoane and Remy Bucher, for their assistance with X-ray diffraction experiments. My gratitude to Marc Marteau at the Laboratoire de Physique des Matériaux in France for his assistance with the ion implantation. I would like to thank Gunter Kellermann and the staff at the LNLS synchrotron in Brazil for their assistance with the synchrotron experiment. My sincere thanks to the following people for providing an intellectually and an exciting social environment: Shaun Wyngaardt, Girma Goro Gonfa, Evariste Minani, Mecit Yaman, Abdulrafiu Tunde Raji, Faith October, Martha Nyinawintore, Emmanuel Nsanzubuhoro, Marie Rose Turamwishimiye, and Samuel Usabuwera. My gratitude to all the members of the solid state and materials physics group, and my fellow postgraduate students in the Physics department for their support and encouragement.

I owe my parents an enormous amount. Though far from me, their moral support was felt all the time. Last, but not least, my wife Philomène, my sons Blaise, Robert, Lambert, and my daughter Celine who have been patient and so close to me. Their moral support has been a comfort in challenging times. With this achievement I have answered the question they have asked so many times: when are you finishing your PhD? May the Heavenly Father to whom I owe this success be praised.

TABLES OF CONTENTS

1 INTRODUCTION 5
2 ION - SOLID INTERACTIONS 9
2.1 Ion stopping processes 10
2.1.1 Nuclear stopping 11
2.1.2 Electronic stopping 13
2.1.3 Ion range parameters 13
2.1.4 Simulation of ion profiles 19
2.2 Radiation damage 20
2.2.1 Collision induced defects 21
2.2.2 Thermally induced defects 21
3 STRAIN – STRESS AND RESIDUAL STRESS 23
3.1 Theory of Strain and Stress 23
3.1.1 Deformation and Strain 23
3.1.2 Forces and Stresses 26
3.1.3 Hooke's law and elastic constants 28
3.2 Residual Stress 31
3.2.1 What is Residual Stress? 31
3.2.2 Classification of Residual Stress 32
4 DEFECT DYNAMICS UNDER INFLUENCE OF STRESS 36
4.1 Point defects in a crystal structure 36
4.2 Diffusion and drift processes 37
4.3 Force on a defect 41
4.4 Strain field due to point defects 43
4.5 Defects and ion implantation 44
5 EXPERIMENTAL 46
5.1 Sample preparation and characterization 46
5.2 Rutherford Backscattering Spectrometry 49
5.2.1 Principles of Rutherford Backscattering Spectrometry 49
5.2.2 Resonance RBS for oxygen detection 57

5.2.3 Experimental details 58
5.3 Stress Determination using Synchrotron Diffraction 63
5.3.1 Concept of diffraction stress analysis 63
5.3.2 Experimental details 77
5.3.3 Peak position determination 90
6 RESULTS 93
6.1 Krypton profile 93
6.2 Oxygen profiling.....101
6.3 Stress determination.....106
6.3.1 $\sin^2$ curves 106
6.3.2 Depth analysis of $\sin^2$ curves 111
6.3.3 Principal stresses and asymmetries..... 118
6.3.4 Uniaxial projected strain..... 125
6.3.5 Stress profile 130
7 DISCUSSION..... 145
7.1 Effect of implantation on the oxygen profile 145
7.2 Effect of stress on implanted krypton ions 147
7.3 Effect of implantation on stress. 150
8 CONCLUSIONS.....152
REFERENCES 155
Appendix A Fitting procedure for depth profiling of stress.....183
Appendix B Macro for diffraction measurement.....186
Appendix C RBS simulation procedure for krypton profile 189
Appendix D Resonance scattering simulation procedure 190
Appendix E $\sin^2$ curves 192
Appendix F Polar plots for the (100) reflection for unpolished samples.....198

1 INTRODUCTION

Ion implantation, as a major method of altering the near-surface composition and properties of materials for technological applications, gained its momentum with the development of semiconductor technology. The driving force within the semiconductor research stimulated research into ion implantation in metals, polymers and insulators. Whereas applications of ion implantation into semiconductors most often requires dopant concentrations less than one atomic percent, the near surface modification of metals normally necessitates implant concentrations of several atomic percent to observe changes in materials properties [1.1]. Early surface modification studies of metals were focused on nitrogen implanted-nitriding steels for wear and hardness improvement [1.2-1.4]. Nitrogen implanted hard materials such as Cobalt-cemented tungsten carbide [1.5] and Ti-6Al-4V [1.6] led also to significant wear reduction. Ions other than nitrogen were also used to improve mechanical properties. In copper alloys, high fluence implantation of boron gave better improvements in friction and wear behaviour of phosphor bronze alloys than did nitrogen or carbon implantation [1.7].

Nowadays, ion implantation is a well-established technique, which extends from research laboratory studies of metastable phase formation to production line fabrication of integrated circuits. This widespread application of ion implantation stems from several advantages of this technique: it allows precise control of the total number of injected ions, it permits independent control of the penetration depth, it can use essentially all combinations of ions and target materials, it may achieve concentrations above the equilibrium solid solubility, and above all, it may be used at low or elevated temperatures [1.8].

Ion implantation is intrinsically a nonequilibrium process. One consequence of this fact is that species, which are quite insoluble in metallic matrices, can be

introduced. Once implanted, insoluble species tend to occupy interstitial as well as substitutional sites. Even at low fluence they may form clusters [1.9], contrary to soluble ions, which locate at substitutional sites where they take part in the formation of new phases. The most insoluble species that can be introduced into metals are inert gases, for which the driving force for precipitation is immense [1.10]. When nanoprecipitates are formed, they are under correspondingly large pressure, sufficient to cause them to solidify. Several studies have shown that heavy rare-gases (Ne, Ar, Kr, Xe) condense within high-pressure cavities as a liquid or as a crystalline solid aligned with the lattice of crystalline host material at room temperature [1.11 - 1.16].

The behaviour of inert gases after implantation has been investigated in connection with the development of nuclear technology [1.17]. Helium, produced in fusion reactors, has been the noble gas most investigated in relation with its interaction with defects in materials [1.18-1.20]. As they may be residues of fission reactions, the heavier rare gases Kr and Xe received attention in connection with their containment as fission products. A combined implantation and sputtering technique was developed at the Atomic Energy Research Establishment (AERE), Harwell, in order to store the radioactive ^{85}Kr in metallic matrices [1.21].

Notwithstanding the extensive work done in connection with the high pressure generated by inert gas implantation in solids, there are still open questions on the mechanisms of point defect dynamics and stress evolution after ion implantation in general and inert gas implantation in particular in solid materials. In general the effect of ion implantation on the residual stress has a complicated dependence on fluence, flux, ion implantation energy, implanted species, target material, temperature, and pre-existing stress. For low dose implantation, the effect is generally to relax the existing stress [1.22 - 1.25]. For instance, in argon implanted polycrystalline titanium low dose implantation has shown to reduce

both a pre-existing tensile stress [1.22], and a pre-existing compressive stress [1.23]. In thin films grown by thermal evaporation, ion implantation during thin film growth was used to decrease the amount of pre-existing stress [1.26]. In krypton implanted $Ag_{50}Co_{50}$ films, a pre-existing tensile stress reduction was also observed [1.27]. Various mechanisms have been proposed for stress relaxation, including plastic flow [1.25, 1.29], local melting and concurrent viscous flow in the vicinity of the ion track [1.30], and defect annealing mechanisms [1.24]. At higher doses an additional stress is generated in the material which is also associated with radiation hardening effects and in increase in stiffness [1.31, 1.32]. Generally, the introduced stress is compressive [1.33, 1.34, 1.25], although an increase in tensile stress has been observed in plasma irradiated stainless steel [1.35]. The increase in compressive stress is generally thought to occur because of atomic peening effects [1.25], but changes in the defect and microstructure as well as phase transitions at high doses [1.36] also play an important role.

Whereas the experimental studies carried out to identify the nature and the evolution of the irradiation-induced defects have focused mainly on fcc and bcc metals [1.37], the information on radiation damage effects in hcp materials remains sparse, probably because of the difficulties associated with the anisotropy of the hcp structure [1.38, 1.39].

From a fundamental research view point, this thesis seeks to contribute to a better understanding of the basic processes underlying the effect of stress assisted diffusion on point defect dynamics in a hcp metal by inert gas implantation. Of interest is the mutual influence of strain fields and point defect distributions in krypton-implanted polycrystalline titanium. Both the pre-existing stress and subsequent changes by the implantation constitute the main focus of this work. Two sets of samples were selected to carry out this investigation. The first batch consisted of five samples in their as-received condition, whereas the second batch consisted of five samples polished in order to obtain samples with

a different stress distribution near the surface. Pairs of samples, one from each batch, were implanted at the same fluence. The experimental studies rely mainly on ion beam analysis, using Rutherford backscattering spectrometry, to obtain depth profiles of the implanted ions, and diffraction techniques for the determination of the strain and stress fields. The Brazilian National Synchrotron Light Source (LNLS), located in Campinas, was used to carry out the strain measurements to determine the full stress tensor.

This thesis is divided into eight chapters, including this introduction. Chapter 2 gives the fundamental aspects of ion-solid interactions in solids. This includes a discussion of the ion stopping processes, the ion range parameters, and radiation damage. Chapter 3 deals with residual stresses in solids. In this chapter the concepts of strain and stress are discussed on the basis of elasticity theory for a better understanding of residual stresses. Defect dynamics in solids is covered in Chapter 4. Diffusion and drift processes, strain fields due to point defects, defects and ion implantation are the main foci in this chapter. Chapter 5 is dedicated to the experimental techniques used in this investigation. In this chapter the sample description and preparation is given. Furthermore, the characterization techniques are described and the experimental procedure presented. Chapter 6 is devoted to the results. Chapter 7 is a comprehensive discussion of the results, and Chapter 8 summarizes the conclusions of this work.

2 ION - SOLID INTERACTIONS

The advantage of using ion beams is due to their ability to penetrate inside a sample where the knowledge of the interactions between the accelerated ions and target material is used in many different ways in modern research and technology [2.1 - 2.3]. Ion beam modification of materials is generally a complex, non-equilibrium thermodynamic process involving both changes of the strain, microstructure and composition in the near surface region [2.4]. Depending on the ion fluence, implantation energy, implanted species, target material and temperature, material properties can be altered. Ion beams are not only used for materials modification, but also, are broadly utilized to probe the elemental composition, to determine the thickness of deposited thin films as well as the structural disorders in materials. The main techniques that are involved in ion beam analysis (IBA) are Rutherford backscattering spectrometry (RBS), elastic recoil detection analysis (ERDA), particle induced X-ray emission (PIXE), and nuclear reaction analysis (NRA).

Typically, implantation starts at energies as low as around 10 eV and may exceed MeV energies. The implanted ions have an approximately Gaussian distribution that is peaked at the mean range beneath the surface that scales with implantation energy, the exact distribution being a function of the fluence and the stopping power of the target [2.5, 2.6]. With this shallow penetration near-surface properties can be controlled independently of bulk phenomena. Practical applications of ion implantation have been used over years in the semiconductor industry [2.7], where only small implanted concentrations (10^{11}-10^{14} cm^{-2}) are needed to produce the desired changes in electronic properties. Significantly larger doses (10^{15}-10^{18} cm^{-2}) are required to alter most properties of interest in metals [2.8]. In the latter area, ion implantation is used as powerful tool for fundamental research and as a technique for changing metallic surface

properties of materials to improve corrosion resistance, wear, friction and hardness [2.9].

A proper understanding of the interactions between energetic ions and materials, especially the forces that slow down the ions is therefore important, not only in controlling the depth profile but also in determining the nature of the lattice disorder produced during ion implantation.

2.1 Ion stopping processes

Once a beam of energetic charged particles is directed onto the surface of a solid, the fast projectiles interact with the stationary near-surface atoms of the solid. In contrast to the interaction of lighter particles, *e.g.* electrons, or photons with matter, the main peculiarity of energetic ion impact is the extremely high localized density of the energy transferred to the target by the particles [2.10].

As an ion penetrates a solid, it undergoes a succession of binary collisions with target atoms and surrounding electrons, losing energy at each encounter. The energy deposition is commonly described by the stopping power, also referred to as the stopping force by some authors [2.11], gives the energy transfer per path length of a particle along its trajectory. The stopping power is the sum of two independent processes, namely nuclear collisions and electronic collisions [2.12].

This can be expressed by

$$\frac{dE}{dx} = \left(\frac{dE}{dx}\right)_{nuclear} + \left(\frac{dE}{dx}\right)_{electronic}. \qquad (2.1)$$

Fig. 2.1 illustrates the types of emission process which can result from both nuclear and electronic collisions. During nuclear collisions, either the incident ions may be elastically scattered back out of the surface or target atoms may be ejected from the surface via kinetic energy transfer to the lattice atoms. Incident

ions may also undergo nuclear reactions giving rise to the emission of reaction products [2.13]. During electronic collisions, ionisation and excitation processes can lead to the emission of radiation in the form of characteristic X-rays [2.14], optical photons [2.15, 2.16], and Auger or secondary electrons [2.17].

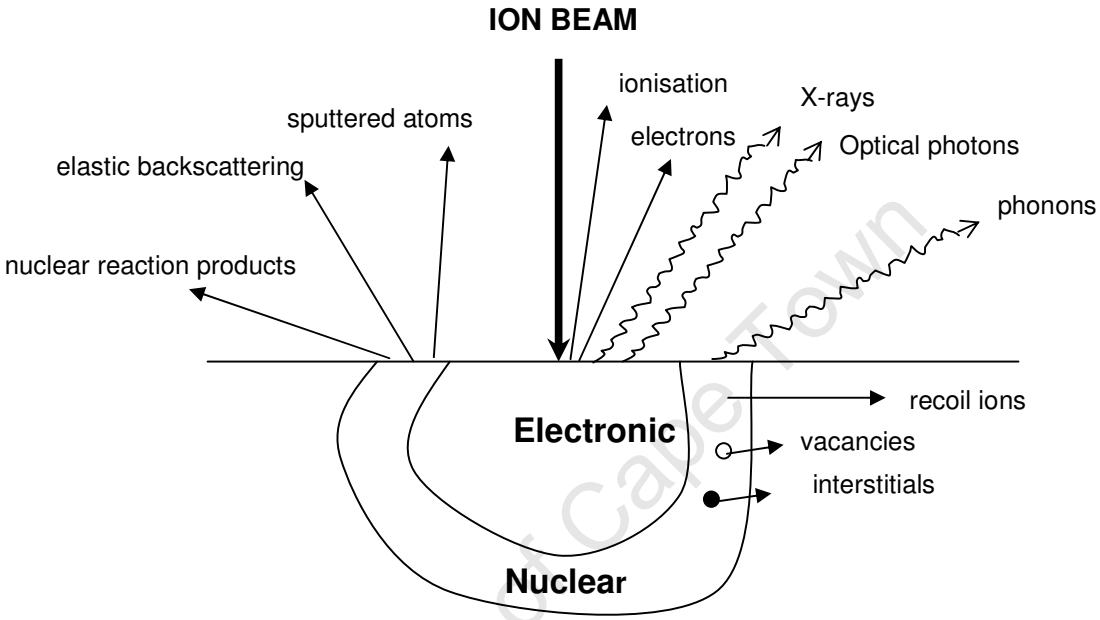

Figure 2.1: Schematic representation of ion–solid interactions.

2.1.1 Nuclear stopping

Nuclear stopping is due to collisions between the incident ion and lattice atoms, where conservation of energy and momentum apply, unless nuclear reactions or nuclear resonances occur as a result of the encounter [2.12]. The nuclear interactions lead to transfer of kinetic energy to the knock-on target atoms which might be displaced from their original positions (if the transferred energy exceeds the displacement energy), and thus might initiate the formation of structural defects, *e.g.* vacancies and interstitials, in crystalline materials. The probability of an incident ion with energy E undergoing a scattering event or a collision with a target nucleus, while traversing a thickness dx, is defined as

$$P(E) = N\sigma(E)dx\,. \qquad (2.2)$$

This probability represents the total fraction of the target surface area which acts as an effective scattering center to the incident energetic particles. N is the number of target atoms per unit volume. The differential energy-transfer cross-section $d\sigma(E)/dT$ is obtained by differentiating Eq. (2.2),

$$P(E,T)dT = \frac{dP(E)}{dT}dT = N\frac{d\sigma(E)}{dT}dTdx = \frac{1}{\sigma(E)}\frac{d\sigma(E)}{dT}dT\,, \qquad (2.3)$$

where $P(E,T)$ is the probability that an ion with energy E will have, during a collision, producing an energy transfer in the range T and dT while traversing a distance dx. In other words, it is simply the ratio of the differential cross-section to the total energy cross-section.

The average energy loss on the ion moving at a distance dx is obtained by multiplying Eq. (2.3) by the transfer energy T and integrating by over all possible values of T:

$$\langle dE\rangle = \int T\frac{dP(E)}{dT}dT = N\int_{T_{\min}}^{T_M} T\frac{d\sigma(E)}{dT}dTdx\,. \qquad (2.4)$$

For an infinitesimal distance dx and omitting the averaging symbol on dE, we obtain

$$\left.\frac{dE}{dx}\right|_n = N\int_{T_{\min}}^{T_M} T\frac{d\sigma(E)}{dT}dT\,, \qquad (2.5)$$

where $\left.\frac{dE}{dx}\right|_n$ is the nuclear stopping power. The lower limit in the integration $T_{\min}$ is the minimum energy transfer required to displace an atom from its lattice site, which is approximately 20-30 eV. The upper limit, T_M, is the maximum transfer

energy given by $T_M = 4M_1M_2/(M_1+M_2)^2$, where M_1 and M_2 are the masses of the incident ion and the target atom, respectively.

2.1.2 Electronic stopping

The energy transferred by the ion to the crystal electrons is called electronic stopping or inelastic loss. The large density of electrons and the high frequency of the collisions will contribute to a continuous energy loss during the slowing down of the incident ion. At ion velocities v significantly lower than the Bohr velocity v_0 ($v_0 = \hbar / m_e a_0$) of the atomic electrons, the ion carries its electrons and tends to be neutralized by electron capture. At these velocities, nuclear stopping is dominant [2.8]. As the ion velocity is increased, the nuclear energy loss diminishes as $1/E_0$, where E_0 is the incident energy of the ion. At higher velocities, the charge state of the ion increases and the maximum stopping power is achieved at around $v > v_0 Z_1^{2/3}$, but the ions are not yet fully stripped. According to Bohr criterion the ions are to more than 50 % fully stripped when $v > v_0 Z_1$. At this point, the ion can be viewed as a positive point charge Z_1, moving with a velocity greater than the mean orbital velocity of the electrons in the shells or subshells of the target atom.

As for the nuclear stopping power, the electronic stopping, has the form

$$-\left.\frac{dE}{dx}\right|_e = n_e \int_{T_{\min}}^{T_M} T \frac{d\sigma(E)}{dT} dT \,, \qquad (2.6)$$

where n_e is the number of electrons per unit volume.

2.1.3 Ion range parameters

One of the most important considerations in any study of ion – solid interactions is the depth (range) distribution of the implanted ions. As mentioned above, the

rate at which the projectile loses energy with penetration depth x is due to both nuclear and electronic energy-loss terms, as shown in Eq. (2.1).

The total length R of the penetration of a projectile into a solid can be found by integrating Eq. (2.1) to give

$$R = \int_0^{E_0} \frac{dE}{(dE/dx)_n + (dE/dx)_e}, \tag{2.7}$$

where E_0 is the incident energy. It is common to express the energy-loss components as stopping cross section $\varepsilon(E)$, where $\varepsilon(E) = \frac{1}{N}\frac{dE}{dx}$, N being the number of target atoms per unit volume. The dimensions of $\varepsilon(E)$ are therefore energy times area, and the conversion to a rate of energy with depth must take into account the target density. As for the total stopping power, $\varepsilon(E)$ is the sum of the nuclear and electronic components.

In Fig. 2.2, a more general three-dimensional presentation of the penetration of a projectile into a solid is shown. An energetic ion impinges on the sample surface at the point (0,0,0), at an angle α to the surface normal that points in the x-direction. The ions come to rest at a position described by the coordinates (x_s, y_s, z_s). R is called the range, and is the actual integrated distance traveled by the ion. The ion's net penetration into the material, measured along the vector of its incident trajectory, is called the projected range R_p. At high fluence, the sputtering phenomenon should be taken into account when determining the projected range. The main consequence of the sputtering is to decrease the calculated projected range with respect to the measured R_p. As indicated in Fig. 2.2, the ion may not be incident normal to the surface. Therefore the depth of penetration x_s, which is defined as the perpendicular distance below the surface that the projectile comes to rest, is not equal to the projected range. The two quantities are equal only if α is zero. The

radial range R_r is the distance from the surface to the point where the projectile comes to rest. It is given by

$$R_r = (x_s^2 + y_s^2 + z_s^2)^{1/2}. \tag{2.8}$$

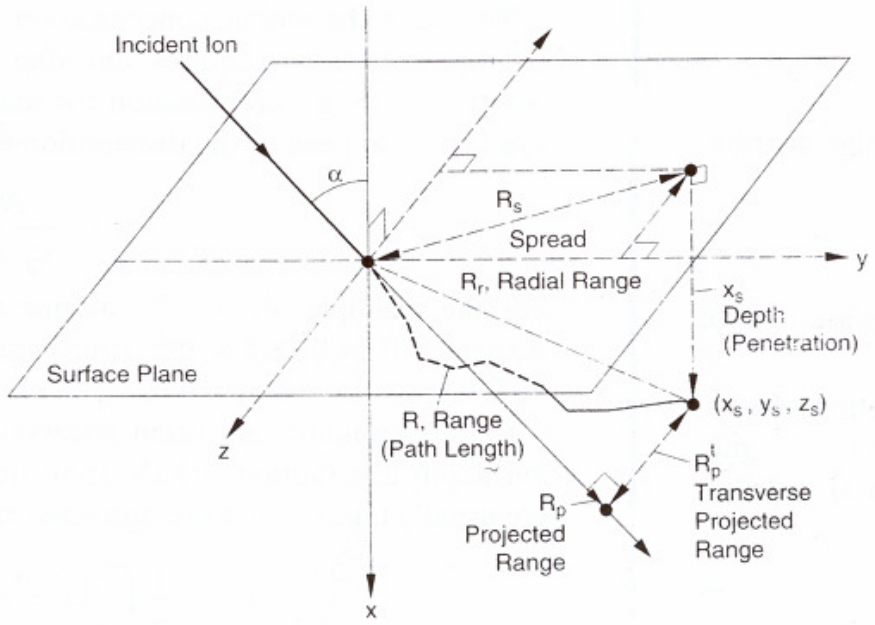

Figure 2.2: Schematic representation for the definition of depth, spread, radial range, longitudinal projected range, transverse projected range, and path length of the ions [2.18].

The spreading range R_s is the distance between the point where the projectile enters the surface and the projection of the projectile's final resting place onto the surface normal. It is given as

$$R_s = (y_s^2 + z_s^2). \tag{2.9}$$

The transverse projected range R_p^t is the vector connecting the radial range and the projected range. It is defined by

$$R_p^t = [(x_s \sin\alpha - y_s \cos\alpha)^2 + z_s^2]^{1/2}. \quad (2.10)$$

In case of normally incident projectiles, the spreading range is equal to the transverse projected range.

Finally, the longitudinal projected range (or projected range) R_p is given by

$$R_p = [(R_r)^2 - (R_p^t)^2]^{1/2}. \quad (2.11)$$

Since the energy of the projectile is lost to the target atoms and electrons in a series of discrete collisions, the energy loss per collision, and hence the total path length will have a statistical spread of their values. This leads to a near Gaussian distribution of stopping distances, which can be comprehensibly evaluated using a model which is based on the Thomas Fermi statistical model, developed by Lindhard *et al* [2.19], known as LSS theory.

Stopping of an ion is a stochastic process, and distributions of arbitrary parameters can be characterized by their moments. The first moment gives the mean μ of a distribution, and for a continuous distribution is defined as

$$\mu = \int_{-\infty}^{\infty} xf(x)dx\,, \quad (2.12)$$

where $f(x)$ is the probability function for the random variable of interest.
The second moment is the variance of the distribution, and is defined as

$$\sigma^2 = \int_{-\infty}^{\infty} (x-\mu)^2 f(x)dx\,. \quad (2.13)$$

The probability function for a Gaussian distribution, is given by

$$f(x) = \frac{1}{\sigma(2\pi)^{1/2}} \exp\left[-\frac{1}{2}\left(\frac{x-\mu}{\sigma}\right)^2\right]. \quad (2.14)$$

The depth distribution $n(x)$ of implanted ions, normalized for an ion implantation dose, or fluence ϕ, is given by comparison with Eq. (2.14) as

$$n(x) = \frac{\phi}{\Delta R_p (2\pi)^{1/2}} \exp\left[-\frac{1}{2}\left(\frac{x-R_p}{\Delta R_p}\right)^2\right], \quad (2.15)$$

where R_p and ΔR_p are the projected range, and straggling respectively, as defined in Fig. 2.3.

The dose or fluence is related to the ion depth distribution by

$$\phi = \int_{-\infty}^{\infty} n(x)dx. \quad (2.16)$$

By setting $x = R_p$ in Eq. (2.15), the expression for the peak atomic density n_p is obtained as

$$n_p = \frac{\phi}{\Delta R_p (2\pi)^{1/2}} \approx \frac{0.4\phi}{\Delta R_p}. \quad (2.17)$$

At low doses implantation profiles can be described by a Gaussian distribution with characteristic parameters R_p and ΔR_p. Higher moments are often necessary to describe the non-Gaussian depth distributions, which occur at higher doses. These moments are usually taken about the projected range and have the general expression [2.8]

$$m_i = \frac{1}{\phi}\int_{-\infty}^{\infty}(x - R_p)^i\, n(x)dx\,, \tag{2.18}$$

where i represents the order of the moment. Higher moments have also specific meanings in defining the ion distribution. The second moment is related to the range straggling

$$\Delta R_p = \left(\frac{m_2}{\phi}\right)^{1/2}, \tag{2.19}$$

whereas the third moment is related to the skewness γ_p, expressed as

$$\gamma_p = \frac{m_3}{(\Delta R_p)^3}. \tag{2.20}$$

The skewness of the projected range distribution gives a measure of the asymmetry of the distribution, where a positive value locates the peak closer to the surface than R_p. In a normal distribution, the skewness is zero.

The fourth moment is related to the kurtosis β_p by the expression

$$\beta_p = \frac{m_4}{(\Delta R_p)^4}. \tag{2.21}$$

The kurtosis provides a measure of flatness of the distribution. For example, for a Gaussian distribution the value of the kurtosis β_p = 3. In higher dose regimes, many processes, such as sputtering, radiation enhanced diffusion, compound formation have effects on the final concentration profile [2.20].

2.1.4 Simulation of ion profiles.

Simulation of ion profiles is performed using the SRIM Monte-Carlo program [2.21], which stands for the stopping and range of ions in matter. This program calculates the stopping and range of ions in matter using a quantum mechanical treatment of individual ion-atom collisions, assuming the projectile to be an ion, and all target species to atoms. During the collisions, the ion and atom have a screened Coulomb collision, including exchange and correlation interactions between the overlapping electron shells. The charge state of the ion within the target is described using the concept of effective charge, which includes a velocity dependent charge state and long range screening due to the collective electron sea of the target. Most aspects of the energy loss of ions in matter are calculated in SRIM. Range and straggling distributions for any of ion over a very broad range of energies in any elemental target can be calculated by following the individual trajectories for a set of ions with the same initial conditions. Figure 2.3 shows the variation of range, neglecting sputtering, with the implantation energy, in the case of Kr implantation in titanium.

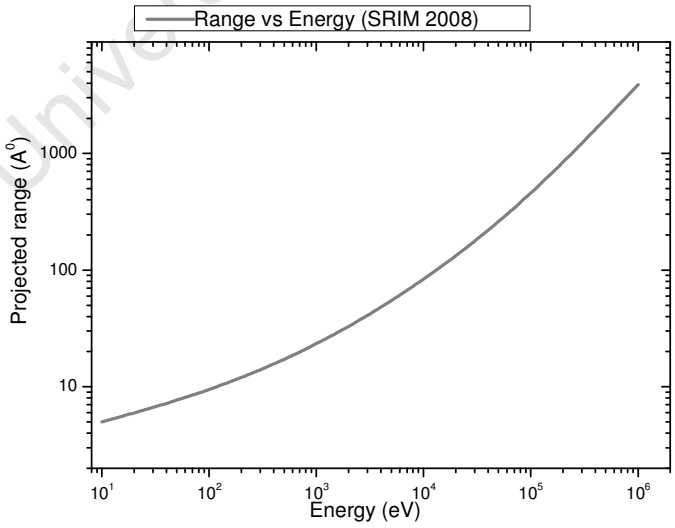

Figure 2.2: Range-energy plot for Kr implantation in titanium.

2.2 Radiation damage

The ion implantation process is generally accompanied by radiation damage, that is disorder in the lattice, consecutive to the introduction of energetic ions, ranging from keV to MeV, in the near surface region. In this process, sufficient energy may be transferred from the ion to displace an atom from its equilibrium position. As a result, the recoiling lattice atom can itself displace many other lattice atoms giving rise to a so-called displacement cascade, originating from a single primary collision between the implanted projectile and target atom. This process leads to a distribution of vacancies, interstitial atoms, and other types of lattice disorder in the region around the ion track [2.22 - 2.24]. The total amount of damage and its distribution in depth, depend on ion species, ion fluence, ion flux, temperature, energy, and channelling effects.

The thickness of the damaged region is expected to be comparable to the projected ion range according to simple theoretical considerations. While this relationship holds for implantation in semiconductors and insulators, in most metals the observed damage region of the crystal lattice extends significantly deeper into the bulk [2.25, 2.26].

Exceptionally large damage depths were reported in copper [2.27, 2.28] and platinum [2.29]. It was proposed that these deviations are the result of migration of interstitial atoms, which are, even at low temperatures, highly mobile and could therefore substantially modify the original primary defect profile. The damage can be observed by techniques sensitive to lattice structures. For example, X-ray diffraction [2.30] and electron microscopy [2.31] can be used to probe local strain fields, whereas positron annihilation [2.32] and RBS [2.33] are sensitive to point defects.

2.2.1 Collision induced defects

A minimum amount of energy, typically 25 eV [2.18], is needed to displace an atom from its lattice position. This energy represents the displacement threshold and is called the displacement energy, E_d. If in the collision process the energy transfer T is less than E_d, the struck atom undergoes vibrations with large amplitudes without leaving its lattice site. If, however, $T > E_d$ the struck atom is able to overcome the potential well that represents its stable position. In the simplest situation, the displaced atom leaves a vacancy and occupies an interstitial site in the lattice. This vacancy-interstitial defect is referred to as a Frenkel-defect [2.34].

The displacement barrier for a lattice atom is not uniform in all directions [2.18]. Depending on the crystallographic structure, the displacement can be higher or lower than the average. For instance, if the struck atom recoils in a direction where it transfers its kinetic energy to its nearest neighbours, then the displacement barrier will be high, and consequently, the displacement energy to form a Frenkel-defect will be also high. Conversely, in relatively open directions, such as <111> directions, or the <110> directions of a crystal with a fcc lattice, the displacement barrier will be low.

2.2.2 Thermally induced defects

As mentioned above, during the slowing down process of energetic ions in a solid, the kinetic energy of a moving ion is partially transferred to host atoms by elastic collisions. The recoiling atoms, in turn, transfer part of their energy to other atoms. All the atomic collisions initiated by a single ion are called a collision cascade. A collision cascade can be divided into three phases [2.35, 2.36]. The initial stage, during which atoms collide strongly, is called the collisional phase, and typically lasts about 0.1–1 ps. As a result of the collisions, a highly disrupted,

very hot (typically 1500 K) region inside the solid is created. The resulting high temperature will spread and be reduced in the solid by heat conduction. This phase is called the thermal spike, and lasts roughly 1 ns. When the heat in the thermal spike has dissipated, there will usually be left a large quantity of defects in the solid material. The defects can be of different forms, ranging from point defects to complex interstitial-dislocation loops and volume defects [2.37,2.38]. Very low dose implantation results in a number of isolated defects, whose concentration can be estimated from the Kinchin-Pease equation [2.39],

$$N_v = \frac{F_{Dn}}{E_d}, \tag{2.22}$$

where F_{Dn} is the energy deposited into the sample by atomic collisions, and E_d is the displacement threshold energy. If the local equilibrium lattice temperature during implantation is high enough, many of these defects will relax by thermally activated migration [2.40]. This phase is referred to as relaxation phase of the collision cascade.

3 STRAIN – STRESS AND RESIDUAL STRESS

This chapter gives a short survey on the theory of elasticity, which is indispensable for a proper understanding of the concepts of strain and stress. These two concepts form the basis of all types of stress analysis, and will be utilized, not only in this chapter, but also in subsequent chapters to relate deformations and residual stresses that occur in solid materials.

3.1 Theory of Strain and Stress

In the following, the fundamental concepts of strain and stress are discussed. It should be recalled that the formalistic description of stress and strain is based on the theory of elasticity, by nature a continuum theory, comprising geometric analysis of deformation or strain and the mathematical analysis of stress in solids. A comprehensive review can be found in the textbooks of Nye [3.1], Noyan and Cohen [3.2], and Landau and Lifschitz [3.3].

3.1.1 Deformation and Strain

An elastic body under an applied load deforms. Deformation leading to shape change is termed distortion, whereas dimensional change without a change in shape is termed dilatation [3.1]. The theory of linear elasticity provides a mathematical description for the displacement which a body undergoes when it is squeezed, stretched, or sheared. To understand this concept, consider the one-dimensional example of an extensible thin rubber band as shown in Fig. 3.1. Two arbitrary points P and Q are marked with the origin O. Let $OP = x$ and $PQ = \Delta x$. After stretching, P moves to P' and Q to Q'. Let $OP' = x + u$ and $P'Q' = \Delta x + \Delta u$. The strain of the section PQ is defined as

$$\frac{\textit{increase in length}}{\textit{original length}} = \frac{P'Q' - PQ}{PQ} = \frac{\Delta u}{\Delta x}. \qquad (3.1)$$

The strain at the point P is the displacement gradient, which in one dimension is defined as

$$\varepsilon = \lim_{\Delta x \to 0} \frac{\Delta u}{\Delta x} = \frac{du}{dx}. \tag{3.2}$$

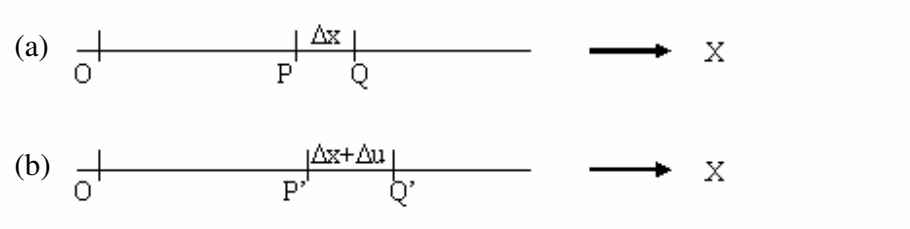

Figure 3.1: An extensible thin rubber band before (a) and after (b) deformation.

For a two-dimensional strain analysis, consider the rectangular element ABCD in Fig. 3.2 with $AB = \Delta x_1, BC = \Delta x_2$ undergoing translation, distortion and dilatation. After deformation, the point B for instance, moves to B' in both direction X_1 and X_2. By defining a local coordinate system X_1', X_2', one can eliminate the translational displacement and obtain,

$$\Delta u_1 = \frac{\partial u_1}{\partial x_1}\Delta x_1 + \frac{\partial u_1}{\partial x_2}\Delta x_2, \tag{3.3}$$

and

$$\Delta u_2 = \frac{\partial u_2}{\partial x_1}\Delta x_1 + \frac{\partial u_2}{\partial x_2}\Delta x_2 . \tag{3.4}$$

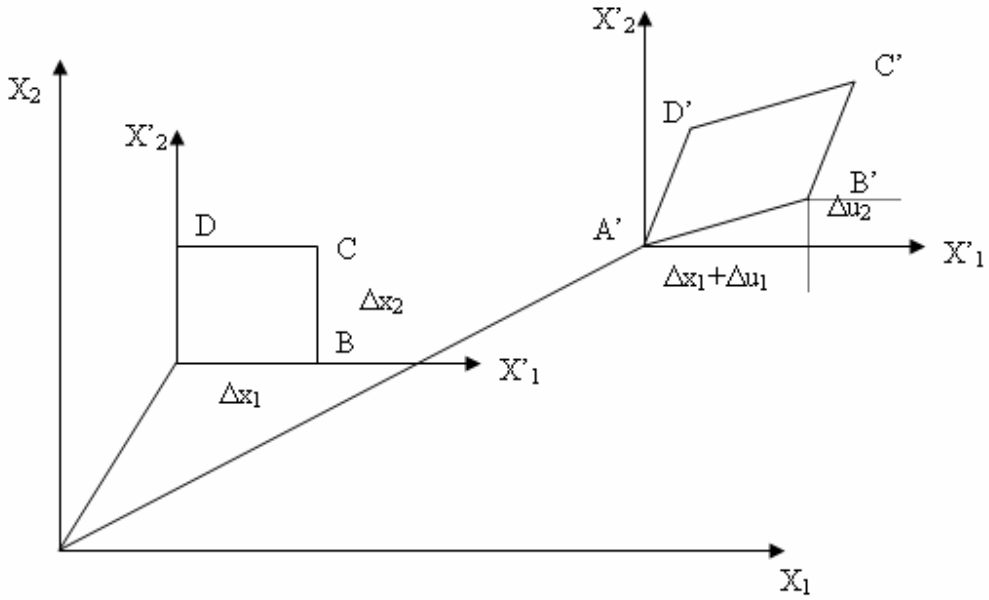

Figure 3.2: Displacement and deformation of a solid body in two dimensions.

The derivatives in Eq. (3.1) and (3.2) describe the variations of the displacement along the axes X_1', X_2'. In matrix notation, the following expression is obtained

$$\begin{pmatrix}\Delta u_1\\ \Delta u_2\end{pmatrix}=\begin{pmatrix}\dfrac{\partial u_1}{\partial x_1} & \dfrac{\partial u_1}{\partial x_2}\\ \dfrac{\partial u_2}{\partial x_1} & \dfrac{\partial u_2}{\partial x_2}\end{pmatrix}\begin{pmatrix}\Delta x_1\\ \Delta x_2\end{pmatrix}. \tag{3.5}$$

It can be seen that the derivatives form a 2-dimensional second rank tensor. Defining the quantities $e_{ij}=\dfrac{\partial u_i}{\partial x_j}$, Eq. (3.3) becomes

$$\begin{pmatrix}\Delta u_1\\ \Delta u_2\end{pmatrix}=\begin{pmatrix}e_{11} & e_{12}\\ e_{21} & e_{22}\end{pmatrix}\begin{pmatrix}\Delta x_1\\ \Delta x_2\end{pmatrix}. \tag{3.6}$$

As the translational and the rotational parts of the displacement are of no interest with regard to material behaviour, we only consider the strain that alters the distances and the relative positions between the points within the body.

Therefore, the strain tensor ε_{ij} is defined as the symmetric part of the tensor e_{ij} [3.2], *i.e.*,

$$\varepsilon_{ij} = \frac{1}{2}\left(e_{ij} + e_{ji}\right) = \frac{1}{2}\left(\frac{\partial u_i}{\partial x_j} + \frac{\partial u_j}{\partial x_i}\right). \tag{3.7}$$

In matrix notation,

$$\varepsilon_{ij} = \begin{pmatrix} \varepsilon_{11} & \varepsilon_{12} \\ \varepsilon_{21} & \varepsilon_{22} \end{pmatrix} = \begin{pmatrix} e_{11} & \frac{1}{2}(e_{12} + e_{21}) \\ \frac{1}{2}(e_{12} + e_{21}) & e_{22} \end{pmatrix}. \tag{3.8}$$

The strain in three dimensions is obtained by a similar procedure and yields a similar second rank tensor:

$$\begin{pmatrix} \varepsilon_{11} & \varepsilon_{12} & \varepsilon_{13} \\ \varepsilon_{21} & \varepsilon_{22} & \varepsilon_{23} \\ \varepsilon_{31} & \varepsilon_{32} & \varepsilon_{33} \end{pmatrix} = \begin{pmatrix} e_{11} & \frac{1}{2}(e_{12} + e_{21}) & \frac{1}{2}(e_{13} + e_{31}) \\ \frac{1}{2}(e_{12} + e_{21}) & e_{22} & \frac{1}{2}(e_{23} + e_{32}) \\ \frac{1}{2}(e_{13} + e_{31}) & \frac{1}{2}(e_{23} + e_{32}) & e_{33} \end{pmatrix}. \tag{3.9}$$

The diagonal elements ε_{ii} of the strain tensor represent the dilatation/contraction, *i.e.* change of length per unit length, and the cross terms, or the off-diagonal, are related to the shear strains. Shear strains represent the change of angle between the perpendicular directions.

3.1.2 Forces and Stresses

Strain is the result of the application of force to a solid material. This force is expressed as stress, *i.e.* as force per area. The surface force at a point is described by a stress tensor [3.4]. To illustrate and define the stress

components, a small cube with face area *A*, within a homogeneously stressed body, is considered, as shown in Fig. 3.3. There are six independent stress components. The normal stresses, σ_{ii} act normal to the cube faces, and the shear stresses, σ_{ij} for $i \neq j$, act parallel to the cube faces. The indices i and j vary from 1 to 3, and equilibrium requires $\sigma_{ij} = \sigma_{ji}$, for $i \neq j$. Otherwise, there would be a net rotational moment on the volume element.

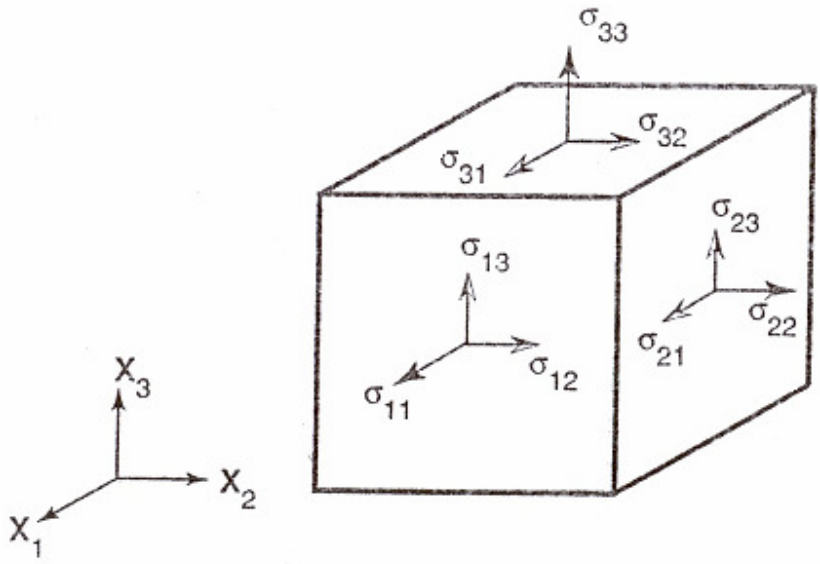

Figure 3.3: The unit cube with the nine components of stress. Due to the symmetry, i.e. $\sigma_{ij} = \sigma_{ji}$, *for* $i \neq j$, *only three of the shear components are independent. All components are shown in their positive directions. Note that* σ_{ij} *means that the stress is acting on the face perpendicular to* x_i, *and in the* x_j *direction [3.5].*

Like strain, stress is also a second rank tensor with nine components in three dimensions. In matrix notation, it is written as

$$\sigma_{ij} = \begin{pmatrix} \sigma_{11} & \sigma_{12} & \sigma_{13} \\ \sigma_{21} & \sigma_{22} & \sigma_{23} \\ \sigma_{31} & \sigma_{32} & \sigma_{33} \end{pmatrix}, \qquad (3.10)$$

where $\sigma_{11}, \sigma_{22}, \sigma_{33}$ are known as normal stresses, and σ_{12}, σ_{13}, and σ_{23} as shear stresses. If the sum of diagonal elements of the stress tensor is zero, then the stress state is termed pure shear.

Because of the symmetry, i.e., $\sigma_{ij} = \sigma_{ji}$, only 6 of the 9 components are independent and are sufficient to describe the stress and the strain at any point in the material. A tensile stress σ_{11} will cause a tensile strain ε_{11} along the X_1 axis and compressive strains $\varepsilon_{22}, \varepsilon_{33}$ along the transverse directions X_2, X_3. When seen microscopically, the transverse strains occur in part because of the cross-bonds between atoms, as shown in Fig. 3.4 [3.2].

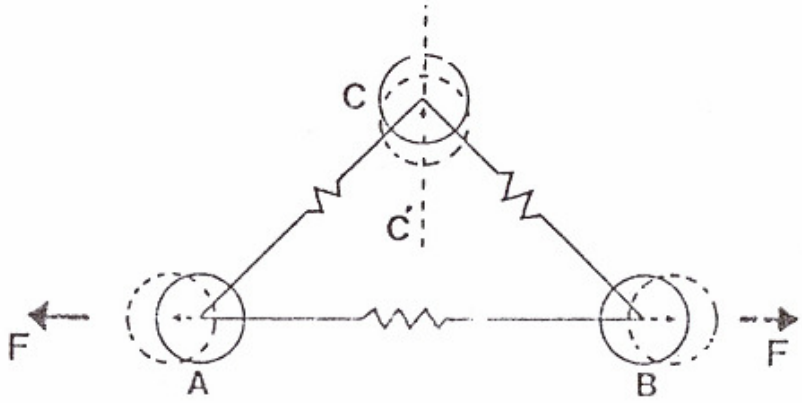

Figure 3.4: Schematic depiction of transverse contraction in a solid loaded in uniaxial tension. Assuming that the atomic bonds can be represented by coil springs, AB elongates if the stress σ_{11} is applied along AB. However, the bonds AC, BC pull on atom C, resulting in a net contraction, and thus a compressive strain along the direction CC' [3.2].

3.1.3 Hooke's law and elastic constants

Under the assumption of small deformations, or the so called elasticity domain, the strain tensor components of a deformed body, depend linearly on the

component of the stress tensor, as expressed by the generalized form of Hooke's law [3.2]

$$\varepsilon_{ij} = \sum_{k,l=1} S_{ijkl}\sigma_{kl} . \tag{3.11}$$

The proportionality constants S_{ijkl} are known as compliances, and are represented in a 4th rank tensor. The inverse of the compliance tensor, the tensor of the elasticity constants or stiffness constants, C_{ijkl} which is also a 4th rank tensor, represents the stress as a function of strain

$$\sigma_{ij} = \sum_{k,l=1} C_{ijkl}\varepsilon_{kl} . \tag{3.12}$$

It should be mentioned here, that the Hooke's law not only shows the relationship between stress and strain, but also introduces specific properties into the framework of the theory of elasticity. The concept of stress, as well as the concept of strain is purely theoretical. For their explanation no information of the real material is used. In contrast, both elastic constants and compliances describe the mechanical properties of the material. Because the strain and the stress tensors are symmetric, the maximum number of independent elastic constants is reduced from 81 to 36. However, due to elastic energy considerations the number of these independent constants is further reduced to 21 [3.4]. This is true for a material crystallising in the triclinic crystal structure, but because of the increasing symmetry of the crystal systems, the number of independent components reduces. Table 3.1 gives an overview of the number of independent elastic constants for different Bravais lattices.

Bravais lattice	Number of independent elastic constants
triclinic	21
monoclinic	13
orthorhombic	9
tetragonal	6 or 7
trigonal	6 or 7
hexagonal	5
cubic	3

Table 3.1: Independent elastic constants for different Bravais lattices [3.1]

For materials with a hexagonal structure, such as titanium, only five independent elastic constants are sufficient to describe the elastic properties. For a cubic structure with the highest symmetry, only three independent elastic constants are sufficient to describe the elastic properties. For an elastically isotropic body, *e.g.* in the form of a polycrystalline solid without texture, the material can be described by only two mechanical quantities, usually given as Young's modulus E, and Poisson's ratio ν. In an elastically isotropic body, Hooke's law relates the strain to the stress by

$$\begin{aligned} \varepsilon_{ii} &= \frac{1}{E}\sigma_{ii}, \\ \varepsilon_{jj} &= -\frac{\nu}{E}\sigma_{ii}, i \neq j. \end{aligned} \tag{3.13}$$

For a unit cube subjected to three normal stresses, the strain along any direction X_i is the sum of the strain caused by the stress in that direction and the strains caused by the stresses acting in the transverse directions, *i.e.*,

$$\begin{aligned}\varepsilon_{11} &= \frac{1}{E}\sigma_{11} - \frac{\nu}{E}(\sigma_{22} + \sigma_{33}),\\ \varepsilon_{22} &= \frac{1}{E}\sigma_{22} - \frac{\nu}{E}(\sigma_{11} + \sigma_{33}),\\ \varepsilon_{33} &= \frac{1}{E}\sigma_{33} - \frac{\nu}{E}(\sigma_{11} + \sigma_{22}).\end{aligned} \tag{3.14}$$

Compactly, Eq. (3.14) can be expressed as

$$\varepsilon_{ij} = \frac{1+\nu}{E}\sigma_{ij} - \delta_{ij}\frac{\nu}{E}\sigma_{kk}, \tag{3.15}$$

where δ_{ij} is the Kronecker delta defined as

$$\delta_{ij} = \begin{cases} 1, i = j \\ 0, i \neq j \end{cases}. \tag{3.16}$$

3.2 Residual Stress

Residual, or internal, stresses play an important role in material and component failure. Of particular significance are stresses in the near surface region which influence mainly the mechanical properties of a particular component. Therefore residual stresses are of special interest in view of the improvement of material properties and of the increase of the lifetime of components. In the following, residual stress is discussed and the different categories of residual stresses are described.

3.2.1 What is Residual Stress?

Residual stresses (RS) are the self-equilibrating internal stresses existing in a free body that has no external forces or constraints acting on its boundary [3.6, 3.7]. Although such stresses tend to exist unnoticed, they are as real as any

stress arising from applied loads or service conditions. The effect of these internal stresses is only observed after acting on the body of the material. For instance, if an internally stressed wire or an aluminium foil is cut, the separated ends will bend. In the same manner, a plate in which a hole is drilled may deform due to internal stresses present before the drilling. A way of interpreting this behaviour is to consider an arbitrary small volume element of the material. Such an element is bounded by its neighbours, and is not necessarily free to assume its unstressed size, shape or orientation. If this element is removed from the material, or at least the material is cut so that it is at the free surface, some or all of the constraints on the element are removed and it will be able to relax through deformation. However, because it will never be possible for all elements to relax, internal stresses will result. Therefore residual stresses are always present in materials independently of external applied forces, and they are in equilibrium.

3.2.2 Classification of Residual Stress

The physical conditions responsible for nearly all residual stresses arise from the interaction between the thermal, chemical and mechanical properties of the material in a specific state [3.8]. Hence, each manufacturing process (*e.g.* rolling or drawing), treatment (*e.g.* annealing or shot-peening), or radiation damage may modify the distribution and the magnitude of the residual stress state in the material, and the final behaviour of the component depends strongly on its history. A summary of the origins of residual stresses is given in Fig. 3.5. As an example, consider a sample which has undergone a heat treatment and afterwards is rapidly quenched. As a result, the surface and the interior will cool at different rates because of the presence of a temperature gradient. The subsequent thermal stresses may easily exceed the plastic limit and plastic flow will result. As the surface contracts more quickly than the volume of the material, on equalisation of the temperatures, a compressive residual stress will be present in the surface region, becoming tensile deeper in the sample. After

cooling, on equalisation of the temperatures, the bulk of the sample therefore ends in net compression with a tensile residual stress at the surface [3.2]. If the same sample is subjected to a forming operation, such as rolling to relieve residual stresses, here again a stress gradient through the sample consisting of elastic and plastic stresses will result. During this manufacturing process, the surface can be extended more than the interior due to friction at the rollers, resulting in compression on the surface. In this operation, the magnitude of the stress is a function of the thickness of the sample, the roller diameter and the degree of reduction [3.2]. The final stress state of the sample depends on all the stages involved in the processing from the production to the finishing.

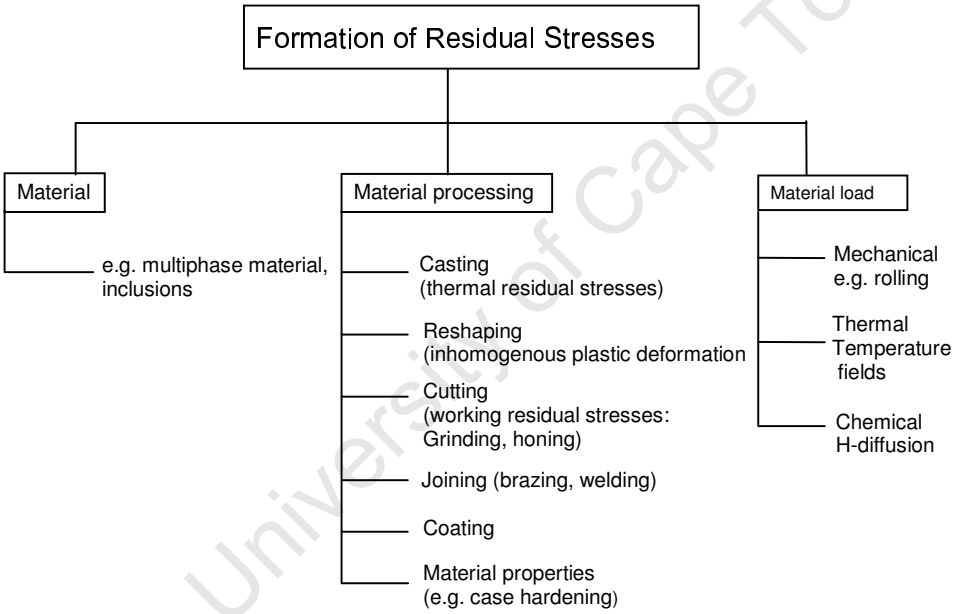

Figure 3.5: Origin of residual-stress formation, after [3.4].

Residual stresses affect the properties of materials and can have a marked influence on the behaviour of components in service. For instance the stress-corrosion sensitivity [3.9 - 3.11], fatigue [3.12], crack growth [3.13], fracture toughness [3.14], creep [3.15], and diffusion [3.16 - 3.18] properties can all be influenced by the magnitude and direction of the residual stress. Therefore residual stress can have both detrimental and favourable consequences for the

behaviour of materials, components and structures in service under certain conditions. Under load, the residual stress will superimpose onto the applied stress, and hence can either act to reduce or increase its effect.

Depending on the scale at which a material is analysed, residual stress can be classified into two categories: macrostresses, and microstresses. The scale of these stresses are illustrated in Fig. 3.6 [3.19].

Macrostresses also known as type 1 (σ^{I}) residual stresses are stresses which vary within a body of a component over a range much larger than the grain size. They represent an average value of the local stresses in a volume that comprises many grains but are still small compared to the overall dimensions of the body. The typical sources of residual macrostresses are heat treatment, welding, and surface processing such as grinding, shot-peening, coating deposition, and ion implantation.

Microstresses are stresses which occur within a body over distances comparable to the grain size. They are classified into 2 categories: Intergranular, and intragranular stresses. Intergranular stresses or type II stresses (σ^{II}) vary on the scale of an individual grain. Intergranular stresses may be expected to exist in single-phase materials because of anisotropy in the behaviour of each grain. They may also develop in multi-phase and composite materials that have differential elastic, plastic, and/or thermal properties. Intragranular stresses or type III residual stresses (σ^{III}) exist within a grain at the atomic level. Intragranular stresses develop around lattice defects such as point defects and dislocations due to strain fields [3.20].

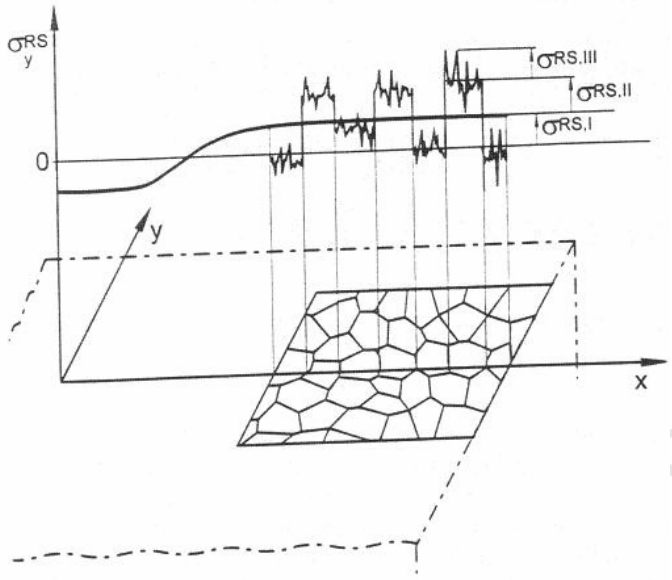

Figure 3.6: Types of residual stresses. $\sigma^{RS,I}$ varies over a range much larger than the grain size. $\sigma^{RS,II}$ Is comparable to grain dimensions while $\sigma^{RS,III}$ is less than the grain diameter [3.19].

4 DEFECT DYNAMICS UNDER INFLUENCE OF STRESS

The presence of defects profoundly influences many physical solid properties such as optical absorption, electrical conductivity, and mechanical strength. The phenomenon of diffusion, which depends on the presence and dynamics of defects, plays a great role in solid state reactions. In this chapter, the diffusion mechanisms of point defects under strain fields will be discussed. Of interest is the interaction of point defect strain fields in a metal with defect strain fields generated by ion implantation.

4.1 Point defects in a crystal structure

It is well known that crystal lattice imperfections have a large effect on most of the physical properties of a solid material. These properties depend crucially on the type and concentration of defects that perturb the original structure [4.1]. Of these, the simplest are point defects, *i.e.* interstitials and vacancies. A vacancy is a lattice position that is vacant because an atom is missing and an interstitial is an atom that occupies a place outside the normal lattice position. It may be a self-interstitial or an impurity atom. Point defects in solid materials inevitably distort the surrounding lattice as illustrated in Fig. 4.1 to accommodate the mechanical misfit or an introduced charge distribution. These two types of misfit are interdependent and can be related to microscopic electric and strain fields [4.2].

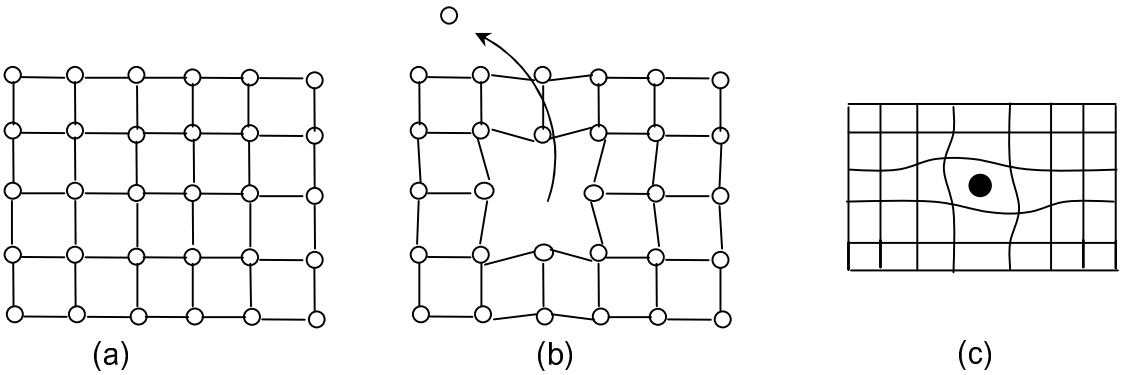

Figure 4.1: Two dimensional representation of (a) a perfect crystal structure (b) a distorted crystal structure caused by a vacancy created by atom removal from its lattice site. (c) distortion of a crystal structure by an interstitial.

Since the formation energies of point defects are of the order of electron volts, which is high compared to thermal energies, their equilibrium concentrations tend to be low. However, in a radiation environment, they form in abundance because of the multitude of the irradiating species, such as electrons, heavy ions or neutrons, interacting with the atoms of the host material [4.3]. The ensuing evolution of the point defect distributions due to diffusion leads to significant changes in microstructure and causes a number of radiation-induced property changes.

4.2 Diffusion and drift processes

Defect dynamics in solids can be described by two superimposing mechanisms: drift and diffusion. Diffusion in solids is the random motion of matter, similar to Brownian motion caused by molecular collisions in a gas. Atomic diffusion proceeds via lattice defects, in particular point defects. A number of possible diffusion mechanisms, such as exchange, ring, interstitial, interstitialcy, crowdion, vacancy, divacancy, relaxion, dislocation pipe diffusion, grain boundary diffusion, and surface diffusion mechanisms are described in [4.4].

In polycrystalline materials the mechanism of diffusion is very complex, since the transport of material is not only limited to the migration of point defects, but also takes place along grain boundaries, internal surfaces, and dislocations, *etc* [4.5]. In the presence of a concentration gradient the random motion of the individual particles results in a net flux away from the region of high concentration. This is simply because there are more particles moving away from the region of high concentration than there are particles moving away from region of low concentration.

Drift occurs when a driving force causes atoms or vacancies to move in a direction determined by the direction of the force. This process is similar to charge transport due to an electric field [4.6]. The driving force of the drift results from the interaction of the defect's own strain fields with a surrounding stress field. The external stress field can be due to the local strain field of other defects in the material, or strain fields due to an applied load acting on the whole material, or more generally, strain caused by any structural and inhomogeneous thermal change of the solid. The forced diffusion of point defects under the influence of a stress can find applications in ion beam modification irradiation, in semiconductor technology [4.7], and is discussed for other systems in many areas of classical physics, plasma physics, and charge transport in semiconductors [4.3]. Much attention is given to study the defect dynamics and stress evolution during semiconductor processing because defect and stress engineering can significantly improve the device performance [4.8 - 4.10]. The focus in semiconductor technology is mainly directed to the study of the stress assisted diffusion of impurity atoms and point defects [4.11, 4.12] including the influence of strain fields on the drift of point defects near the surface or at the interfaces [4.13], and near inhomogeneities of semiconductor materials [4.14].

In metals, stress induced diffusion or macroscopic deformations of diffusion couples during interdiffusion have been studied empirically. The transport of

interstitial hydrogen in metals, also known as the Gorsky effect [4.15], is a classic example of diffusion. The deformation field due to an applied field causes interstitial hydrogen to move towards expanded areas, setting up a concentration gradient that causes an additional time-dependent strain. The transport process depends on the applied field, the mobility, and on the chemical potential of the hydrogen. In precipitation coarsening [4.16] and radiation damage induced defect clustering [4.17], diffusion is usually treated thermodynamically through a minimization of energy. There are two main reasons for studying diffusion in metals [4.18]. The first reason is to understand the changes that occur in solids at high temperatures for diffusion processes such as precipitation, oxidation, radiation damage, creep, and annealing, *etc*. The second reason for studying diffusion is to learn about point defects and their movement under strain fields.

To fully understand the influences of pressure and stress on diffusion processes it is important to consider both the effects on the point defect concentrations [4.14, 4.19, 4.20] and on the point defect mobilities [4.14, 4.21, 4.22].

As mentioned above, for a concentration distribution of defects $c(r)$ under the influence of a driving force $F(r)$, there are two contributions to the defect (particle) dynamics. The first contribution is the defect flux due to diffusion under the thermal motion:

$$J_D = -D\nabla c\,, \tag{4.1}$$

where D is the diffusivity or diffusion coefficient. The diffusion coefficient is generally described by the empirical equation

$$D = D_0 e^{\left(-\frac{H}{kT}\right)}, \tag{4.2}$$

where D_0 is a temperature independent factor, H is the activation energy or enthalpy, k is Boltzman's constant and T is the absolute temperature.

The second contribution to the defect dynamics is caused by drift, *i.e.* a directed motion under an applied force *F:*

$$J_F = \eta c F\,, \tag{4.3}$$

where η is the mobility. The mobility is a measure of how fast a defect can be moved, on average, under the influence of an applied force. Its product with the force gives the drift velocity, which is familiar from elementary hydrodynamics [4.23], and electric conduction [4.24]. The mobility and the diffusivity are related through the Nernst-Einstein relation

$$D = \eta k T\,. \tag{4.4}$$

The rate of change of concentration at any position r in the distribution is derived from the total flux using Fick's law

$$\frac{\partial c}{\partial t} = -\nabla(J_D + J_F) + S(r,t)\,, \tag{4.5}$$

where the source term S represents the rate at which defects are created at any point.

By substituting the expressions of J_D and J_F into Eq. (4.5), the general form of the drift-diffusion equation is obtained

$$D\left[\nabla^2 c - \frac{1}{kT}(F.\nabla c + c\nabla.F)\right] + S(r,t) = \frac{\partial c}{\partial t}\,. \tag{4.6}$$

The dominant mechanism for atomic diffusion is vacancy diffusion. In all crystals there are vacancies, *i.e.* lattice sites that are unoccupied. When an atom from an adjacent site jumps into the vacant site, the atom is said to have diffused by a hopping mechanism. From the theory of specific heat, atoms in a crystal oscillate around their equilibrium positions, and occasionally these oscillations become violent enough to allow an atom to change sites. It is the jumping of atoms from one site another which gives rise to diffusion in solids. For an atom to escape its bond, and diffuse into an adjacent site, it has to acquire enough thermal energy. With an increase in temperature the natural vibrational energy of the atoms is increased so that an atom is more likely to have enough energy to jump into a vacancy, leaving of course a vacant site behind as it does so.

4.3 Force on a defect

The three main driving forces for the drift of any point like particle in condensed matter, described by Wipf [4.15] for the interstitial hydrogen atom, also hold for vacancies and substitutional defects. The causes of these three forces are thermal gradients, electric fields, and elastic strains. Electromigration of vacancies, for instance, requires force terms resulting from both the lattice strain and the electric field acting on the effective charge, Z^* of the defects [4.25].

$$F = Z^* eE \,. \tag{4.7}$$

Similarly, a temperature gradient, will result in a force

$$F = -\frac{H_M}{kT} k \nabla T \,, \tag{4.8}$$

where H_M is the migration enthalpy of the defect.

The third force is the elastic force on a defect, which depends strongly on the symmetry of the defect itself. This arises because the force results from the interaction of the applied strain field with that produced by the defect itself. This is comparable to the magnetic force on a current element arising from the superposition of the external magnetic field onto that produced by the current.

The force on a general inhomogeneity in an elastic medium was derived by Eshelby, by treating the defect as a Somigliana dislocation [4.26]. If the applied stress is σ and the displacement field of the defect in the surrounding medium is u, the force is given by the surface integral,

$$F = \oint_{\Sigma} (u \cdot \nabla\sigma - \sigma \cdot \nabla u)\, ds\,. \tag{4.9}$$

The surface of integration Σ is any surface which encloses the surface singularity corresponding to the defect without cutting it. For a point-like defect, Σ is a closed surface, which has the symmetry of the displacement field. For a true point defect in an isotropic medium, the surface is a sphere. Both point and extended volume defects can be thought of as elastic inclusions with a different volume V, to that of the region of the surrounding matrix V_0, which they replace [4.27,4.28]. The relative difference in volume can be expressed in terms of a mismatch parameter α as

$$V = V_o(1-\alpha)\,. \tag{4.10}$$

In this situation, an interstitial atom will generally constitute a centre of dilatation, with a positive α, and a vacancy a centre of contraction, with a negative α. The force of such inclusion is given by Eshelby as

$$F = \alpha \frac{4}{3} \pi r_0^3 \nabla Tr(\sigma)\,, \tag{4.11}$$

where r_0 is the radius of the defect core and the trace of the stress tensor $Tr(\sigma) = \sigma_{11} + \sigma_{22} + \sigma_{33}$ is the normal stress.

4.4 Strain field due to point defects

To investigate the influence of defects on each other it is necessary to consider the strain field which is intrinsic to the individual defects. The displacement around a point defect can be expressed as the derivative of the Lamé strain potential [4.29],

$$u(r) = -\nabla u(r), \tag{4.12}$$

where $u(r) = \frac{A}{r} = A(r_1^2 + r_2^2 + r_3^2)^{-\frac{1}{2}}$ with r being the displacement, and A is an arbitrary constant.

Differentiating the components of the displacement leads to

$$u_i(r) = \frac{1}{2} A\left(r_1^2 + r_2^2 + r_3^2\right)^{-\frac{3}{2}} 2r_i = \frac{A}{r^3} r_i . \tag{4.13}$$

The strain is given by the derivative of the displacement:

$$\varepsilon_{ii} = \frac{\partial u_i}{\partial r_i} = A\frac{\partial}{\partial r_i}\left[r_i\left(r_1^2 + r_2^2 + r_3^2\right)^{-\frac{3}{2}}\right] = \frac{A}{r^3}(1 - 3\frac{r_i^2}{r^2}), \tag{4.14}$$

and

$$\varepsilon_{ij} = \frac{1}{2}\left(\frac{\partial u_i}{\partial r_j} + \frac{\partial u_j}{\partial r_i}\right) = -\frac{A}{2}\left(\frac{3}{2}\frac{r_i r_j}{r^5} + \frac{3}{2}\frac{r_j r_i}{r^5}\right) = -\frac{3}{2}\frac{A}{r^3}\frac{r_i r_j}{r^2} . \tag{4.15}$$

If the medium is isotropic the normal stress is directly proportional to the normal strain, which is given by its trace. Summing the three components in Eq. (4.14), leads to

$$Tr\varepsilon = \frac{A}{r^3}\left[(1-3\frac{r_1^2}{r^2})+(1-3\frac{r_2^2}{r^2})+(1-3\frac{r_3^2}{r^2})\right] = \frac{A}{r^3}\left(3-3\frac{r_1^2+r_2^2+r_3^2}{r^2}\right) = 0 \quad (4.16)$$

From Eq. (4.14) and Eq. (4.15), the radial and tangential strains [4.30] can be obtained if one of the coordinate axes parallel to the position vector is for example set to $r = (r_1, 0, 0)$,

$$\varepsilon_{rr} = -\frac{2A}{r^3}, \varepsilon_{\theta\theta} = \varepsilon_{\phi\phi} = \frac{A}{r^3}. \quad (4.17)$$

Eq. (4.16) and Eq.(4.17) show that the strain field due to a spherically symmetric defect in an infinite isotropic medium is a pure shear, which causes no dilatation of the surrounding medium. It can be concluded that spherically symmetric point-like defects cannot influence the dynamics of other point defects. This might not be the case for a real anisotropic material. Therefore experimental studies are needed to enlighten this theoretical observation.

4.5 Defects and ion implantation

Due to the fact that energetic ions can deposit energy at high densities over very short times, ion implantation can be used to create highly non-equilibrium alloyed surface layers. The introduction of defects and their subsequent migration during ion bombardment leads to changes in both microstructure and the distribution of defects in the near surface region [4.31]. Despite the shallow (about 10 μm or less) surface layers that are produced, long-lasting improvements may occur when ion species, ion energy, and ion doses are carefully selected [4.32, 4.33]. At low dose implantation, the majority of defects introduced are point defects. At

higher doses it can be assumed that extended defects produced in the ion cascade [4.17] act as sources of internal stress, which may drive the drift of point defects. The mathematical description is simplified to a one dimensional problem, because all distributions are averaged laterally.

The forced diffusion equation in one dimension is

$$D\left[\frac{d^2c}{dz^2}-\frac{1}{kT}\left(F_3\frac{dc}{dz}+c\left(\frac{\partial F_1}{\partial z}+\frac{\partial F_2}{\partial z}+\frac{\partial F_3}{\partial z}\right)\right)\right]+S(z)=\frac{dc}{dt}. \qquad (4.18)$$

where F_1, F_2, F_3 are the components of the force exerted by a point defect.

Substituting the components of the force from Eq. (4.11), Eq. (4.18) becomes

$$\begin{aligned} & D\left[\frac{d^2c}{dz^2}-\frac{4\pi\alpha r_0^3}{3kT}\sum_{i=1}^{n}\left(\frac{dc}{dz}\frac{\partial\sigma_{ii}}{\partial z}+c\frac{\partial^2\sigma_{ii}}{\partial z^2}\right)\right]+S(z) \\ &= D\left[\frac{d^2c}{dz^2}-\frac{\alpha}{kT}\frac{4\pi r_0^3}{3}\frac{d}{dz}\left(c\sum_{i=1}^{n}\frac{\partial\sigma_{ii}}{\partial z}\right)\right]+S(z) \quad , \qquad (4.19) \\ &= \frac{dc}{dt} \end{aligned}$$

where r_0 is the radius of the defect core.

Eq.(4.19) expresses the total stress from all sources including applied stress and all types of defects, either initially present or introduced during implantation. The distribution $c(z)$ corresponds to the actual depth distribution of vacancies or implanted ions, in the absence of clustering. The source term $S(z)$ corresponds to the rate of implantation or vacancy production due to implantation damage.

5 EXPERIMENTAL

This chapter focuses on the description of the samples and their preparation as well as on the characterization techniques used to evaluate the influence of stress fields on the ion implanted species and the influence of ion implantation on the pre-existing stress. Special emphasis is put on the description of the Rutherford Backscattering experiment to determine the ion profile, and on the synchrotron experiments for stress determination. In addition optical microscopy is used for preliminary studies of the sample condition.

5.1 Sample preparation and characterization

The material used in this study is commercially pure α-titanium. Titanium discs, of 25 mm diameter and 0.33 mm thickness, cut from rolled sheet in half-hard condition were obtained from Goodfellow Ltd. As specified by the supplier, the impurities consist of 1200 ppm oxygen, 700 ppm iron, 130 ppm carbon, 50 ppm nitrogen, and 19 ppm hydrogen. The yield strength, the tensile strength, and the elongation of titanium samples, as measured by the manufacturer, are 406 MPa, 498 MPa, and 4 % respectively.

One set of samples was polished in order to prepare samples with smooth surfaces, free of damage introduced during the processing, as well as to obtain samples with a different stress distribution in the near surface region. The samples were mounted on a specially manufactured sample holder consisting of a mild steel cylinder (outer part), and an adjustable brass cylinder (inner part), with an accurately machined indentation of 25 mm (inner radius), and 45 mm (outer radius), as shown in Fig. 5.1. The polishing procedure consisted of several steps. In the first step a surface layer was removed by 600, 800, 1000, and 1200 grit silicon carbide papers. The samples were then roughly polished using Struers paste containing diamond particles of 6 μm diameter. Further polishing steps were performed using pastes containing $3\mu m$, and $1\mu m$ diameter

diamond particles for approximately 15 min for each polishing step. Finally an alumina suspension, containing alumina particles of approximately 0.04 μm, was employed for approximately 10 min. Rough, intermediate and final polishing were performed on a Struers DP 9 universal polisher wheel, with a speed of 250 rpm. At every stage the surface condition was checked using a Reichert Me3A optical microscope at 100X magnification.

Figure 5.1: Photograph showing the top view of the sample holder

As can be seen in Fig. 5.2, the as-received sample is characterised by asperities and the surface becomes smoother with polishing. Metallographic studies on previous samples from the same supplier with the same specifications show the microstructure to consist of equiaxed α-grains with slip bands resulting from the rolling process [5.1].

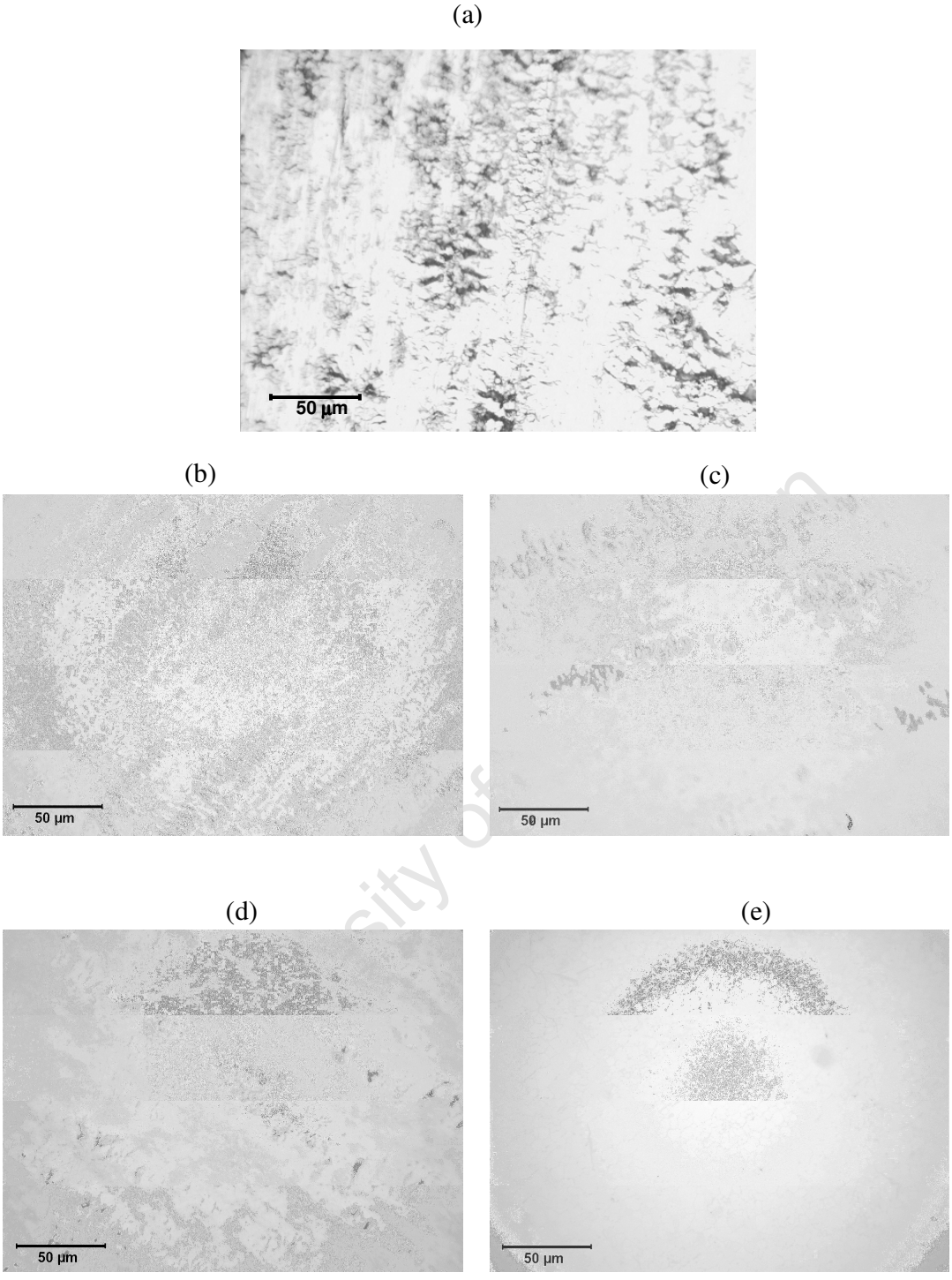

Figure 5.2: Polishing stages. (a) unpolished sample (b) Rough polishing (6 μm diamond paste). (c) and (d) Intermediate polishing (3 μm and 1 μm diamond paste). (e) Final polishing, 0.04 μm alumina (Al_2O_3).

Implantation was performed using the EATON™ NV 3206 implanter [5.2] by Marc Marteau at the Laboratoire de Physique des Materiaux UMR6630-CNRS. The ion energy can be varied between 20 and 400 keV, with a typical current less than 650 μm, a dose uniformity of 0.75 %, and a reproducibility of ± 1%. The vacuum system is maintained by a diffusion pump at the ion source. The pressure in the beamline and at the end station attains $3x10^{-7}$ Torr. The sample temperature is maintained by a water cooling system. Before the implantation process, the samples were divided into two batches. The first batch consisted of five samples in their as-received condition, whereas the second batch consisted of five polished samples. Pairs of samples, one from each batch, were implanted at the same fluence with 180 keV Kr, and a beam current of 11 μA was used. The fluences were regulated by implantation at different times. Table 1 provides the sample names adopted throughout this work, their status with respect to surface and implantation states.

As-received samples	Polished samples	Fluence (Kr^+/cm^2)	Implantation time (s)
N5	P5	-	-
N1	P1	$1x10^{14}$	10
N2	P2	$5x10^{14}$	50
N3	P3	$1x10^{15}$	100
N4	P4	$5x10^{15}$	500

Table 5.1: Sample names and implantation fluence

5.2 Rutherford Backscattering Spectrometry

5.2.1 Principles of Rutherford Backscattering Spectrometry

Rutherford Backscattering Spectrometry (RBS) is an important technique commonly applied in the analysis of materials [5.3]. It is used to determine the

elements present in a given sample, their stoichiometry, and their depth distribution. RBS in simple terms is based on the measurement of the recoil energy of ions backscattered from atoms in a target material. This method is based on four fundamental physical concepts that contribute to qualitative and quantitative analysis of projectile-target atom interactions. The energy transfer from the projectile to a target nucleus in an elastic two-body collision leads to the concept of the kinematic factor and to the capability of mass determination. The atomic composition is analysed by taking advantage of the concept of Rutherford scattering cross section for an energetic ion beam, interacting with atoms in a solid, under pure electrical repulsion between the ion and atomic nuclei [5.3]. As a projectile pushes its way through the target, it slows down and its kinetic energy decreases. This process leads to the concept of stopping cross section and to the capability of depth profiling. The last concept is related to the energy straggling associated with the spread of the beam energy due to statistical fluctuations of the energy transfer while the beam is penetrating the target material. All these processes occur in backscattering experiments and determine the resulting backscattering spectrum.

RBS finds its strength in investigating the near surface of solid materials where the elemental depth distributions can be analysed with good sensitivity for high mass elements and good mass separation for low mass elements [5.4]. The weaknesses of the technique are, of course, its low sensitivity in detecting light elements and low mass separation of heavy elements. As discussed later this can be overcome by making use of resonance scattering. In the following the four fundamental concepts, *i.e.,* kinematics, scattering cross section, energy loss, and energy loss straggling will be discussed in a more quantitative manner.

a) Kinematics

When a sample is bombarded with a beam of high energy particles, the vast majority of the particles are absorbed and a small fraction of the incident particles are backscattered and detected by a detector located at an angle θ. The interaction between the particle and the target atom can be described as an elastic collision, using classical physics, if two conditions apply: (1) the projectile energy must be larger than the binding energy of the atoms in the target; and (2) nuclear reactions and resonances must be absent. Nuclear processes depend on the specific choice of projectile and target atom, therefore the upper limit of the projectile energy varies with the atoms involved in the collision process. For instance, with a H^+ beam, nuclear effects can appear even below 1MeV, whereas they start to appear above 2 MeV with a He^+ beam [5.3]. Fig. 5.4 gives the notation and the geometry of the scattering process. Since the initial ion energy, is much higher than the lattice binding energies, the ion scattering process can be simulated on the basis of elastic collisions between pairs of nuclei while, ignoring the relatively weak lattice forces. By applying the principles of conservation of energy and conservation of momentum, parallel and perpendicular to the direction of incidence, the following equations are obtained

$$E_0 = \frac{1}{2}M_1 v_0^2 = \frac{1}{2}M_1 v_1^2 + \frac{1}{2}M_2 v_2^2 = E_1 + E_2, \tag{5.1}$$

$$M_1 v_0 = M_1 v_1 \cos\theta + M_2 v_2 \cos\phi, \tag{5.2}$$

$$0 = M_1 v_1 \sin\theta - M_2 v_2 \sin\phi, \tag{5.3}$$

where M_1, v_0, E_0 and M_2, v_1, E_1 are the masses, the velocities, and the energies of the incident particle and the target atom, respectively. The angle θ is the scattering angle of the incident particle, and the angle ϕ is the recoil angle of the target atom.

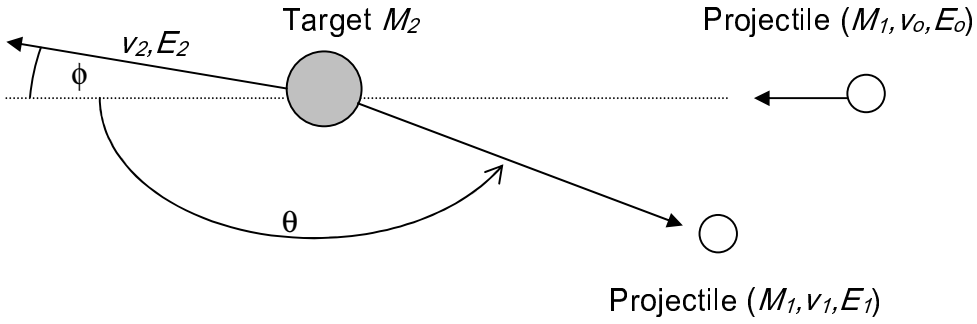

Figure 5.4: Schematic of a classic collision and backscattering process of a lighter projectile (mass M_1) with a heavier target atom (mass M_2) which was initially at rest. The process is seen in the laboratory frame of reference.

The arrangement of the above equations leads to the kinematic factor K defined as the ratio of the projectile energy after collision to the projectile energy before collision,

$$K = \frac{E_1}{E_0} = \left[\frac{\left(M_2^2 - M_1^2 \sin^2\theta\right)^{1/2} + M_1 \cos\theta}{M_1 + M_2} \right]^2 \qquad (5.4)$$

Eq. (5.4) contains the essence of how backscattering spectroscopy acquires the ability to sense the mass of a target atom. The value of M_2 can be determined by measuring E_1 after the collision if E_0, M_1, and θ are known.

b) Scattering cross section

The identity of target atoms is established by the energy of the scattered particle after an elastic collision. The number of target atoms per unit area is determined by the probability of a collision between the incident particles and target atoms. The relative number of backscattered particles from a target atom into a given

solid angle for a given number of incident particles is related to the differential scattering cross section defined as [5.3]

$$\frac{d\sigma}{d\Omega} = \frac{1}{N_s}\left[\frac{1}{d\Omega}\frac{dQ}{Q}\right], \tag{5.5}$$

where N_s is the number of target atoms per unit area, dQ is the number of particles backscattered into a differential solid angle $d\Omega$, and Q is the total number of incident particles. For a thin target of thickness t with N atoms/per unit volume, $N_s = Nt$.

To calculate the differential cross section for an elastic collision, the principles of conservation of energy and momentum are applied. The force that acts during the collision between the projectile and the target masses is assumed to be a repulsive Coulomb force. The distance of closest approach is large compared with nuclear dimensions, but small compared with the Bohr radius $a_0 = \frac{\hbar}{m_e e} = 0.53\,\text{Å}$. These assumptions being made, the differential scattering cross section is given by Rutherford formula [5.3]

$$\left(\frac{d\sigma}{d\Omega}\right)_c = \left(\frac{Z_1 Z_2 e^2}{16\pi\varepsilon_0 E_{0(c)} \sin^2(\theta_c/2)}\right)^2, \tag{5.6}$$

where the subscript c indicates that the values are given with respect to the centre of mass coordinates. Z_1 is the atomic number of the projectile with mass M_1, Z_2 is the atomic number of the target atom with mass M_2, θ is the scattering angle, e is the electronic charge, and E_0 is the energy of the projectile immediately before scattering. The Rutherford scattering cross section is expressed in barn/steradian, 1 barn being $10^{-24} cm^2$. For the general case, the transformation of Eq. (5.6) from the centre of mass to the laboratory frame of reference yields

$$\frac{d\sigma}{d\Omega} = \left(\frac{Z_1 Z_2 e^2}{8\pi\varepsilon_0 E_0 \sin^2\theta}\right)^2 \frac{\left[\left(1-\left(\frac{M_1}{M_2}\sin\theta\right)^{1/2} + \cos\theta\right)\right]^2}{\left[1-\left(\frac{M_1}{M_2}\sin\theta\right)^2\right]^{1/2}} \quad . \qquad (5.7)$$

The order of magnitude of the differential cross section is mainly dependent on the atomic numbers Z_1, and Z_2 of the incident particle and the target atom respectively, the incident particle energy E_0 and the scattering angle θ.

c) Energy loss

As described in section 2.1, the projectile ion loses energy on entering and leaving the target material. The amount of energy ΔE lost per distance x traversed depends on the identity and the velocity of the projectile, and on the density and composition of the target material. The signal detected due to an atom located at the sample surface will appear in the energy spectrum at a position $E_1 = KE_0$, where K is the kinematic factor. The signal from a collision with atoms of the same mass below the sample surface will be shifted by an amount equal to the energy lost while the projectiles pass through the sample, both before ΔE_{in} and after a collision ΔE_{out}. The sequence of energy loss, as illustrated in Fig. 5.5, goes through 3 steps:

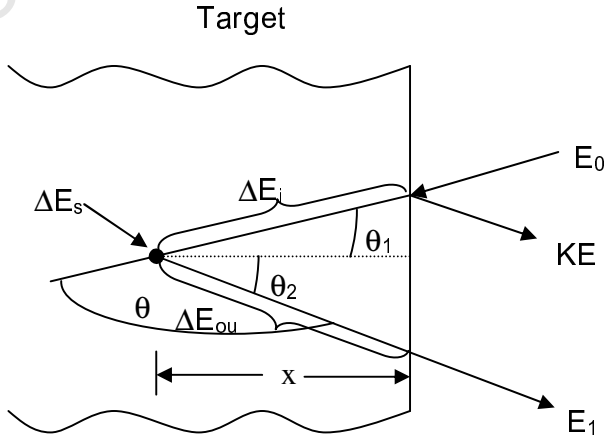

Figure 5.5: Schematic showing energy loss before and after scattering at depth x.

(1) Energy lost via electronic stopping on the inward path of the projectile, $\triangle E_{in}$

$$\triangle E_{in} = \frac{x}{\cos\theta_1}\left(\frac{dE}{dx}\right)_{in}, \tag{5.8}$$

where θ_1 is the angle between the sample normal and the direction of the incident particle.

(2) Energy lost in the scattering process,

$$\triangle E_s = (1-K)E_x, \tag{5.9}$$

where $E_x = E_0 - \frac{x}{\cos\theta_1}\left(\frac{dE}{dx}\right)_{in}$.

(3) Energy lost due to electronic stopping on the outward path of the projectile after collision,

$$\triangle E_{out} = \frac{x}{\cos\theta_2}\left(\frac{dE}{dx}\right)_{out}, \tag{5.10}$$

where θ_2 is the angle between the sample normal and the direction of the scattered particle.

The energy of the particle detected is therefore given by

$$E_1 = E_0 - \triangle E_{in} - \triangle E_s - \triangle E_{out}, \tag{5.11}$$

or

$$E_1 = KE_0 - \left[\frac{K}{\cos\theta_1}\left(\frac{dE}{dx}\right)_{in} + \frac{1}{\cos\theta_2}\left(\frac{dE}{dx}\right)_{out}\right]x. \tag{5.12}$$

The energy width of the signal from a thin layer is given by

$$\triangle E = \left[\frac{K}{\cos\theta_1}\left(\frac{dE}{dx}\right)_{in} + \frac{1}{\cos\theta_2}\left(\frac{dE}{dx}\right)_{out}\right]x = [S]x\,, \qquad (5.13)$$

where $[S]$ is referred to as the backscattering energy loss factor or S factor [5.3]. The path of the incident particle, the path of the scattered particle and the normal of the sample lay all in one plane, so that the scattering angle in the laboratory frame of reference is given by $\theta = 180° - \theta_1 - \theta_2$.

An equivalent set of equations [5.3] can be given in terms of the stopping cross sections rather than $\frac{dE}{dx}$,

$$\triangle E = [\varepsilon]Nx\,, \qquad (5.14)$$

where $[\varepsilon] = \left[\frac{K}{\cos\theta_1}\varepsilon_{in} + \frac{1}{\cos\theta_2}\varepsilon_{out}\right]$ is called the stopping cross section factor or ε factor.

For the near surface region, the thickness x is small, and the relative change in energy along the incident path also becomes small. A surface energy approximation is therefore used, and $\left(\frac{dE}{dx}\right)_{in}$, and $\left(\frac{dE}{dx}\right)_{out}$ are evaluated at E_0 and KE_0, respectively. In the same manner, the stopping cross sections $\varepsilon(E_0)$ and $\varepsilon(KE_0)$ are evaluated at E_0 and KE_0. The expressions for energy loss and stopping cross section are then written as

$$[S_0] = \left[\frac{K}{\cos\theta_1}\left(\frac{dE}{dx}\right)_{E_0} + \frac{1}{\cos\theta_2}\left(\frac{dE}{dx}\right)_{KE_0}\right], \qquad (5.15)$$

and

$$[\varepsilon_0] = \left[\frac{K}{\cos\theta_1}\varepsilon(E_0) + \frac{1}{\cos\theta_2}\varepsilon(KE_0)\right]. \qquad (5.16)$$

d) Energy loss straggling

Due to the different mechanism of energy transfer involved, and the dispersion in the number of interactions, the energy loss of charged particles penetrating a material is a statistical process which leads to energy broadening. This phenomenon is called energy straggling. Energy transfer processes leading to straggling are mainly collisions between nuclei and double and multiple scattering. At lower energies only the valence electrons of the target material participate in the energy loss and straggling, whereas at higher energy the atomic core electrons also contribute [5.5, 5.6].

5.2.2 Resonance RBS for oxygen detection

Oxygen is frequently present in processing, sometimes as an unwanted contaminant, and at other times as a necessary element to achieve desired material properties. The precise non-destructive determination of the oxygen content in materials is of great practical importance, in *e.g.* optoelectronic applications [5.7], semiconductor technology [5.8], the study of corrosion processes [5.9], and more recently in the development of high-Tc superconducting materials [5.10]. There are a number of techniques known to be useful in oxygen detection, such as secondary ion mass spectroscopy (SIMS) [5.11, 5.12], or Auger electron spectroscopy (AES) [5.12, 5.13], but most of these methods are limited when the absolute measurement of low oxygen concentration is required. Furthermore, they induce major damage to the material, and the necessity of using standards with compositions as close as possible to the material under investigation to obtain quantitative results constitutes a major disadvantage.

Rutherford Backscattering Spectrometry (RBS) provides a quantitative depth profiling of an atomic species in a host material without inducing major damage

to the material [5.3]. However, due to the low kinematic factor and the low scattering cross section of oxygen relative to other elements, RBS is not suitable for adequate oxygen analysis. The oxygen signal is often submerged in the background signal caused by the heavier elements. An alternative to RBS is the elastic nuclear resonance measurement also known as resonance elastic backscattering [5.14 - 5.15], to enhance the oxygen sensitivity. This technique is based on the concept that when the energy of the probing ^{4}He ions of the incident beam exceeds a certain threshold, the cross section of the target species increases by 1-2 orders of magnitude in comparison to the corresponding RBS cross section [5.16 - 5.18]. This leads to a relatively lower background from heavy elements, and a better counting statistics for oxygen [5.19 - 5.20].

5.2.3 Experimental details

a) The Van de Graaff Accelerator

The accelerator, as the source of the ion beam for sample characterization, is the most important part of the RBS experiment. The 6 MV Van de Graaff Accelerator used for the RBS experiments is described fully in [5.21]. The Van de Graaff facility, located at iThemba LABS, Faure, South Africa, is a high precision variable energy machine, capable of accelerating light and heavy ions to energies between 0.5 and 20 MeV with an energy spread of less than one part in 1000.

In a single ended Van de Graaf accelerator, such as iThemba LABS accelerator, an ion source (helium in our case) is positioned at the high voltage terminal, and the other end is at ground, where the ion beam emerges from the Pelletron with energy roughly equivalent to the terminal voltage. The ion accelerator is

connected to several beam lines and uses switching magnets to steer the beam from one beamline to another.

b) RBS beamline

After being deflected into the beamline by the switching magnet, the ion beam is collimated and focused by a series of electrostatic lenses, magnetic lenses and apertures. A Faraday cup is mounted in the middle of the beamline to monitor the beam quality and provide feedback for beam focusing and adjustments. At the end station, the beam is collimated through apertures which can be adjusted to 1 mm or 2 mm diameter. To achieve a base pressure of about 10^{-5} Torr in the RBS chamber, roughing and turbo pumps are used. Fig. 5.6 shows the different components of the RBS beam path from the Faraday cup to the end station.

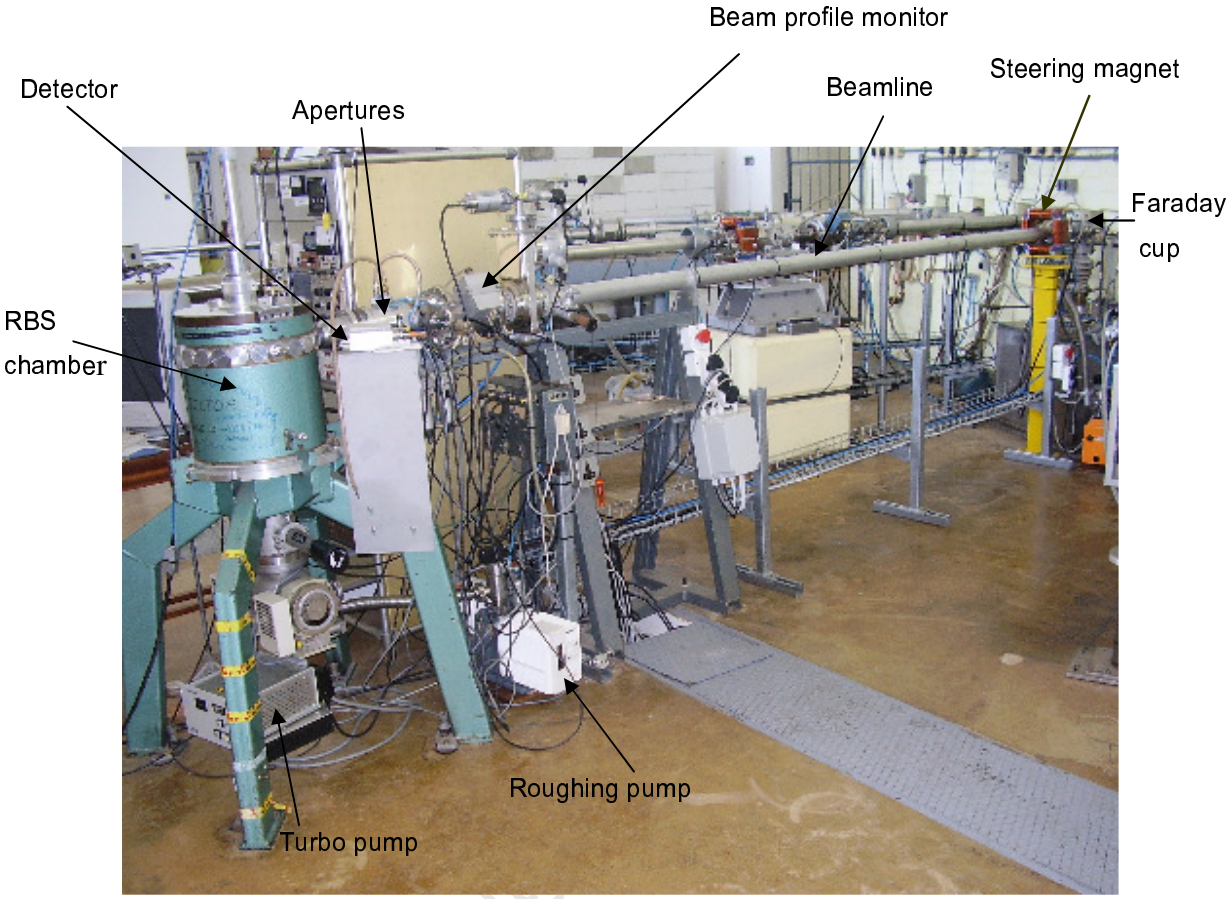

Figure 5.6: Photograph of the RBS beamline located at iThemba LABS (Cape Town).

c) The RBS chamber

The sample chamber located at the end of the beamline is an enclosure which contains a stage for holding the sample holder, the beam entrance, a detector, and the vacuum system. The sample chamber is aligned with the beam by a series of positioning screws and bolts. The alignment is done so that the beam coming in through the final aperture hits a crosshair on the beam window on the far side of the chamber. This assures that the beam is focused in the centre of the chamber where the sample is mounted. The layout of the RBS chamber, the sample, and the detector positions are shown in Fig. 5.7. The radius of the

chamber is 175 mm. The sample holder is a metal ladder which can accommodate ten samples. To avoid channeling effects when measuring the single crystal calibration standard samples, the sample holder is tilted to an angle ϕ equal to 80° with respect to the incident beam. The surface barrier detector is mounted at a fixed scattering angle θ equal to 15° with respect the incident beam direction. The sample-detector distance is equal to 145 mm.

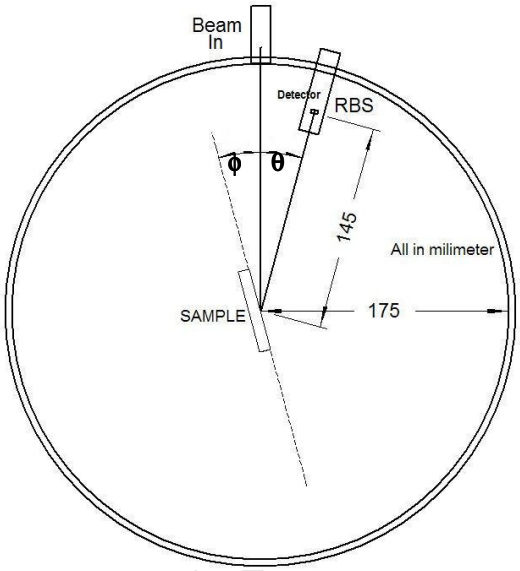

Figure 5.7: Layout of the RBS chamber indicating sample and detector position.

d) RBS experiment

Conventional backscattering measurements were performed with 2.00 MeV $^4He^+$ ions. The samples were mounted individually along the ladder and then loaded into the sample chamber. The standard samples used to calibrate the channel number in terms of backscattered ion energy were platinum (Pt), palladium (Pd), titanium (Ti), and silicon oxide (SiO_2). An average current of 78 nA and total charge of 20 μC were chosen. The vacuum base pressure was better than $1x10^{-4}$ Torr. The energy spectrum of the scattered radiation was recorded using a surface barrier detector at a constant scattering angle 15º, with respect to the

incident beam direction, as shown in Fig 5.7. The detector energy resolution was 20 keV.

The resonance scattering was performed in a standard RBS geometry. The beam energy was varied between 3.0 and 3.3 MeV, with a step of 0.02 MeV, to observe the oxygen resonance, at different depths. To analyse the oxygen profile, sequential spectra were taken as the energy was increased stepwise. For all measurements, the multichannel analyser calibration was 5.8 keV/channel as determined by the calibration standards.

By means of RUMP software [5.22], conventional RBS as well resonance scattering data were analysed. Inputs to the RUMP program include beam energy, ion species, integrated incident charge, detector solid angle, energy-channel conversion factor, energy resolution, angle between the sample normal and the incoming beam, and the angle between the beam direction and the detector.

For a spectrum synthesis the sample is considered to consist of a stack of sublayers, each with uniform composition and therefore a fixed energy loss. Each simulated spectrum is made up of the superimposed contributions from each element of each sublayer in the sample. Any such contribution is referred to as brick. To determine the location in energy of a brick, the energy loss is computed along the inward and outward path of the beam through all overlying sublayers. In case of impurity or implanted ion analysis within a given layer, the SPECIES command in conjunction with the EQUATION command is used to define the distribution. The EQUATION command defines a Gaussian profile with range and straggling as parameters. The refinement procedure consists in first varying the projected range value while the straggling value is fixed and vice versa until the agreement is found. Analysis details are shown in Appendix C. To analyse the oxygen profile, sequential spectra were taken stepwise, as shown in Appendix D,

and E. The scattering cross section data for He on oxygen, of Gurbich [5.23], calculated for a scattering angle of 165°, were used. With the RUMP program, the calculated spectrum is compared with the experimental spectrum and various features are matched to obtain the scaling and normalisation parameters.

5.3 Stress Determination using Synchrotron Diffraction

Among a number of methods available for stress analysis, the diffraction technique, employing either conventional X-ray or synchrotron radiation, is very suitable for the non-destructive residual stress analysis of the near surface region of polycrystalline materials, or even thin films [5.24, 5.25]. X-ray stress analysis is based on the experimental determination of elastic strains, which are converted to stresses by means of the theory of elasticity [5.26]. In the following the concept of diffraction stress analysis and the experimental procedures to determine stress in the ion implanted samples will be discussed.

5.3.1 Concept of diffraction stress analysis

Residual stresses can be classified as macrostresses, and microstresses depending on the scale at which a material is analysed, as discussed in section 3.2. In a crystal structure, residual stresses can be characterised in terms of their effect on the X-ray diffraction pattern. The basic feature of diffraction stress determination is the use of interplanar spacings as atomic level strain gauges. Bragg's law

$$\lambda = 2d^{hkl} \sin\theta^{hkl}, \qquad (5.17)$$

determines the peak position by relating the lattice spacing d^{hkl} of a family of planes, identified by the Miller indices (hkl), to the diffraction angle θ^{hkl} to a

given wavelength λ. Concentrating firstly on the determination of macroresidual stresses in a polycrystalline material, it is important to underline here that the lattice spacings are measured in the direction of the scattering vector. Therefore, the direction-dependent measurement of lattice strains associated with the macroresidual stresses is possible. The interplanar spacings of a specific set of planes (*hkl*) are obtained from diffraction of differently orientated grains. This is achieved by measuring the same diffraction peak under different tilts and rotations of the sample with respect to the incident beam. Due to the presence of stress, there will be a shift in the measured peak position corresponding to the change in average lattice spacing in the direction measured, as illustrated in Fig. 5.8.

Usually the diffraction angle θ^{hkl}, and hence d^{hkl} is obtained from the position of the maximum or centroid of the (*hkl*) peak. It is then possible to calculate the elastic strain ε^{hkl} from

$$\varepsilon^{hkl} = \frac{\left(d^{hkl} - d_o^{hkl}\right)}{d_o^{hkl}}, \qquad (5.18)$$

where d_0^{hkl} is the strain-free lattice spacing of the (*hkl*) lattice planes.

In the case of microstresses, the strain may vary considerably over short distances, but with no net effect over the illuminated volume. In this situation, the effect of microstresses leads to an angular broadening of the diffraction peak, but without any change in its position [5.27].

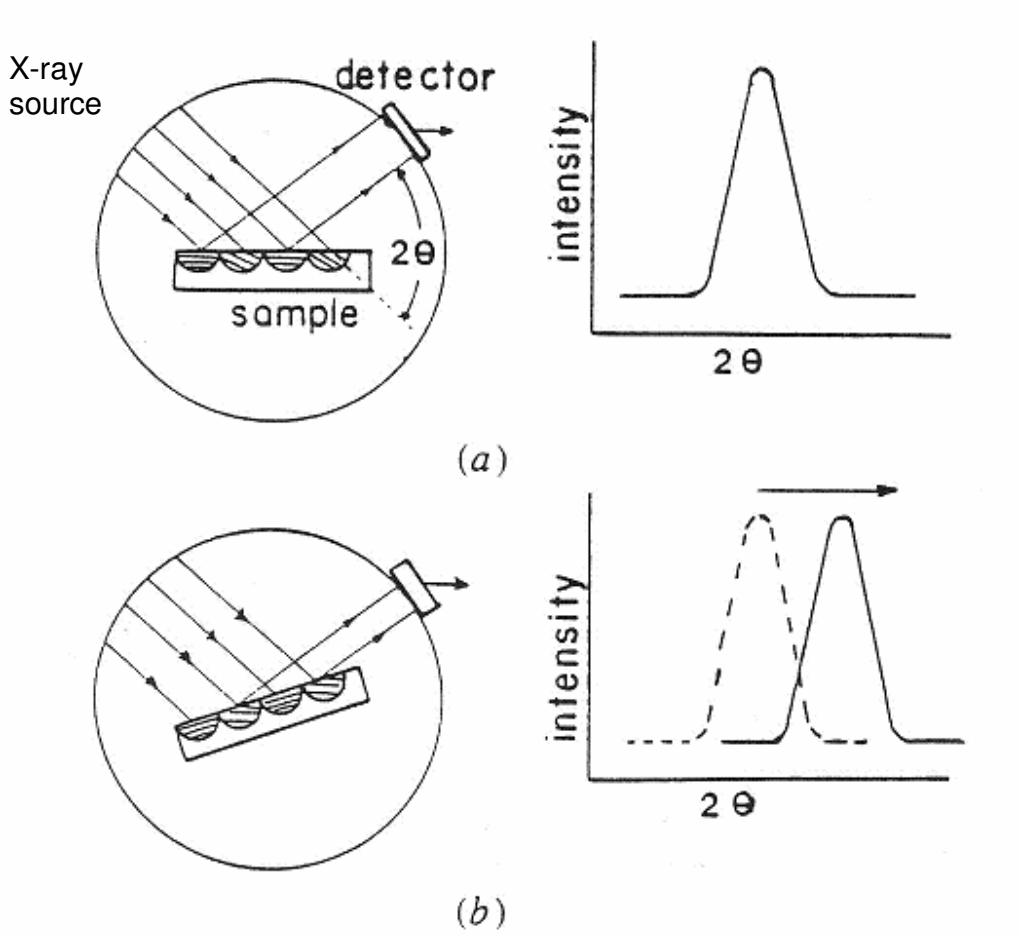

Figure 5.8: Schematic of diffraction stress determination:
(a) certain atomic planes satisfy Bragg's law and diffract X-rays at a 2θ value which depends on the spacing of the (hkl) planes. (b) After the sample is tilted, diffraction occurs from other grains, but from the same set of planes. Since in a stressed sample the interplanar spacing is different, there will be a change in diffraction angle as indicated by the peak shift [5.27].

a) Diffraction geometry and strain measurement procedure

The direction of the strain measurement, is usually denoted by the angles ψ and ϕ, where ψ is the angle of inclination of the sample surface normal to the

diffraction vector, and ϕ denotes the rotation of the sample around the sample surface normal.

A typical diffraction geometry, as well as the definition of the sample reference system S_i and the laboratory reference system L_i, is shown in Fig. 5.9. In the sample coordinate system S_i, S_1 and S_2 are in the surface of the sample, whereas S_3 is orientated along the surface normal to the sample. In the laboratory reference system L_i, L_3 points in the direction of the normal of the family of planes (*hkl*) whose lattice spacings are being measured. If the sample is tilted, both axes S_3 and L_3 are separated by ψ. L_2 is in the sample surface plane making an angle of ϕ with the S_2 axis. In this setup, the tilt angle ψ and azimuth angle ϕ, are used to determine the sample orientation in every step of the measurement. At a fixed Bragg angle θ^{hkl}, different measurement directions bring different grains into diffraction condition. The linear lattice strain measured for a particular (ψ, ϕ) direction is the normal component of the tensor strain along the diffracting plane at the measurement point.

Full determination of the strain tensor, and hence the determination of stress, at a point requires at least six independent measurements. Theoretically, in the absence of statistical and experimental uncertainty this can be achieved by measuring the six strain components in different (ψ, ϕ) directions at the same point.

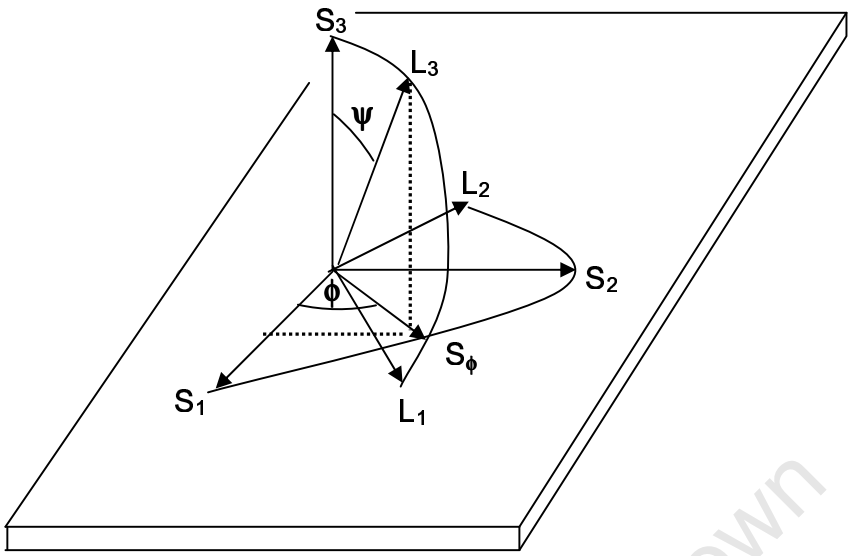

Figure 5.9: Definition of the angles ψ and ϕ with respect to both, the laboratory coordinate system L_i and the coordinate system S_i.

b) Fundamental equation of X-ray stress determination

Using Eq. (5.18), strain measured in the above defined coordinate systems along L_3 is given by

$$\varepsilon_{\phi\psi} = \frac{\left(d_{\phi\psi} - d_0\right)}{d_0}, \tag{5.19}$$

where $d_{\phi\psi}$ is the lattice spacing from grains oriented so that the chosen Bragg reflection leads to diffraction. The strain measured in the laboratory reference system can be expressed by the lattice strains ε_{ij} in the sample coordinate system by tensor transformation, as described in [5.28]

$$\varepsilon_{\phi\psi} = a_{3k} a_{3l} \varepsilon_{kl}, \tag{5.20}$$

where a_{3k} and a_{3l} are the direction cosines between L_3 and S_k, and S_l respectively. The indices k and l can take the values 1, 2, and 3.

For this operation the sample coordinate is rotated around the S_3 axis by the azimuthal angle ϕ and tilted around S_2 by the inclination angle ψ. The transformation matrix a_{ik} is given by

$$a_{ik} = \begin{pmatrix} \cos\phi\cos\psi & \sin\phi\cos\psi & -\sin\psi \\ -\sin\phi & \cos\phi & 0 \\ \cos\phi\sin\psi & \sin\phi\sin\psi & \cos\psi \end{pmatrix}. \tag{5.21}$$

Substitution of a_{3k} and a_{3l} in Eq. (5.20) yields

$$\begin{aligned} \varepsilon_{\phi\psi} = {} & \varepsilon_{11}\cos^2\phi\sin^2\psi + \varepsilon_{12}\sin 2\phi\sin^2\psi + \varepsilon_{22}\sin^2\phi\sin^2\psi + \varepsilon_{33}\cos^2\psi \\ & + \varepsilon_{13}\cos\phi\sin 2\psi + \varepsilon_{23}\sin\phi\sin 2\psi. \end{aligned} \tag{5.22}$$

Equation (5.22) is the fundamental equation of X-ray strain measurement [5.24,5.29,5.30]. It can be also be written in the form

$$\begin{aligned} \varepsilon_{\phi\psi} = {} & (\varepsilon_{11}\cos^2\phi + \varepsilon_{12}\sin 2\phi + \varepsilon_{22}\sin^2\phi - \varepsilon_{33})\sin^2\psi \\ & + (\varepsilon_{13}\cos\phi + \varepsilon_{23}\sin\phi)\sin 2\psi + \varepsilon_{33}. \end{aligned} \tag{5.23}$$

Eq. (5.23) connects the measured strains with the components of the strain tensor in the reference system of the sample. Finally Hooke's law links the measured strain tensor ε_{ij} to the stress tensor σ_{ij}:

$$\varepsilon_{ij} = s_{ijkl}\sigma_{kl}, \tag{5.24}$$

where i and j can take values 1,2 and 3, and S_{ijkl} is the tensor of the elastic compliances. Eq. (5.24) cannot directly be substituted in Eq. (5.20), because the elastic compliances are usually given in the reference system of the crystal's unit cell rather, than the sample reference system. Therefore, it is necessary to

perform a fourth rank tensor transformation, for which the ε_{11} component is shown as an example:

$$\varepsilon_{11} = b_{1m} b_{1n} b_{ko} b_{lp} S_{mnop} \sigma_{kl}. \tag{5.25}$$

The tensor of the elastic constants S_{mnop} is given in the coordinate system of the unit cell of the crystal, and the b_{ij} are the direction cosines between the basis vectors of the unit cell and the sample reference system. Substituting Eq. (5.25) into Eq. (5.24) makes this equation unwieldy, but, if the material under consideration is isotropic, then Hooke's law becomes much simpler:

$$\varepsilon_{ij} = \frac{1}{2} s_2(hkl)\sigma_{ij} + \delta_{ij} s_1(hkl)\sigma_{kk}. \tag{5.26}$$

The subscript k is a dummy index, and implies summation over all k, and δ_{ij} is Kronecker delta.

The quantities $s_1(hkl)$ and $\frac{1}{2}s_2(hkl)$ are the X-ray elastic constants. These are averaged single crystal elastic constants, which take into account the elastic response of the grains which contribute to the actual diffraction [5.28]. For an elastically isotropic material, these are directionally independent and related to the macroscopic elastic constants by

$$\begin{aligned} s_1^{hkl} &= -\frac{\nu}{E} \\ \frac{1}{2} s_2^{hkl} &= \frac{1+\nu}{E}, \end{aligned} \tag{5.27}$$

where υ and E are Poisson's ratio and Young's modulus, respectively.

Substitution of Eq. (5.26) into Eq. (5.23), and taking into account Eq. (5.27), yields

$$\varepsilon_{\phi\psi} = \frac{1+\nu}{E}(\sigma_{11}\cos^2\phi + \sigma_{12}\sin 2\phi + \sigma_{22}\sin^2\phi - \sigma_{33})\sin^2\psi + \frac{1+\nu}{E}(\sigma_{13}\cos\phi + \sigma_{23}\sin\phi)\sin 2\psi + \frac{1+\nu}{E}\sigma_{33} - \frac{\nu}{E}(\sigma_{11}+\sigma_{22}+\sigma_{33}), \quad (5.28)$$

or, in terms of the X-ray elastic constants as

$$\varepsilon_{\phi\psi} = \frac{1}{2}s_2^{hkl}(\sigma_{11}\cos^2\phi + \sigma_{12}\sin 2\phi + \sigma_{22}\sin^2\phi - \sigma_{33})\sin^2\psi + \frac{1}{2}s_2^{hkl}(\sigma_{13}\cos\phi + \sigma_{23}\sin\phi)\sin 2\psi + \frac{1}{2}s_2^{hkl}\sigma_{33} + s_1^{hkl}(\sigma_{11}+\sigma_{22}+\sigma_{33}). \quad (5.29)$$

Eq. (5.29) expresses the measured strain in terms of the stress tensor components in the sample frame of reference.

c) The $\sin^2\psi$ method

In a diffraction experiment as described above, only the near surface region of a sample can be probed, leading to the assumption that the stress in this region is biaxial, *i.e.* all components σ_{i3} of the stress tensor are zero [5.31]. Thus Eq. (5.29) reduces to

$$\varepsilon_{\phi\psi} = \frac{1}{2}s_2^{hkl}\sigma_\phi \sin^2\psi + s_1^{hkl}(\sigma_{11}+\sigma_{22}), \quad (5.30)$$

where

$$\sigma_\phi = \sigma_{11}\cos^2\phi + \sigma_{12}\sin 2\phi + \sigma_{22}\sin^2\phi. \quad (5.31)$$

Measuring the strain $\varepsilon_{\phi\psi}$ at a chosen angle ϕ and at different tilt angles ψ, and plotting the strain against $\sin^2\psi$, leads to a straight line with the slope $\frac{1}{2}s_2^{(hkl)}\sigma_\phi$, and intercept $s_1^{hkl}(\sigma_{11}+\sigma_{22})$, provided that $\frac{1}{2}s_2^{hkl}$ and σ_ϕ are constant. It should be mentioned that the stress σ_ϕ obtained in this approach, known as the $\sin^2\psi$-

method, and introduced by Macherauch and Müller in 1961, is a scalar quantity [5.32]. If several stress values σ_ϕ are acquired from the slopes of $\sin^2\psi$ plots measured in different azimuthal directions ϕ, say σ_ϕ, $\sigma_{\phi+45^\circ}$, $\sigma_{\phi+90^\circ}$, the stress components σ_{11}, σ_{12}, and σ_{22} can be calculated from Eq. (5.31).

It is important to note that in certain cases, the application of this method does not lead necessarily to the expected linear behaviour [5.33,5.34]. In textured materials for example, where the grains are preferentially oriented, the X-ray elastic constants can vary with ψ and ϕ. As a result the $\sin^2\psi$ plot shows an oscillatory behaviour (Fig. 5.10a). Another situation is where the shear stresses are non-zero. This case introduces a ψ-splitting in the plot of the lattice spacing (or strain) versus $\sin^2\psi$ (Fig. 5.10b).

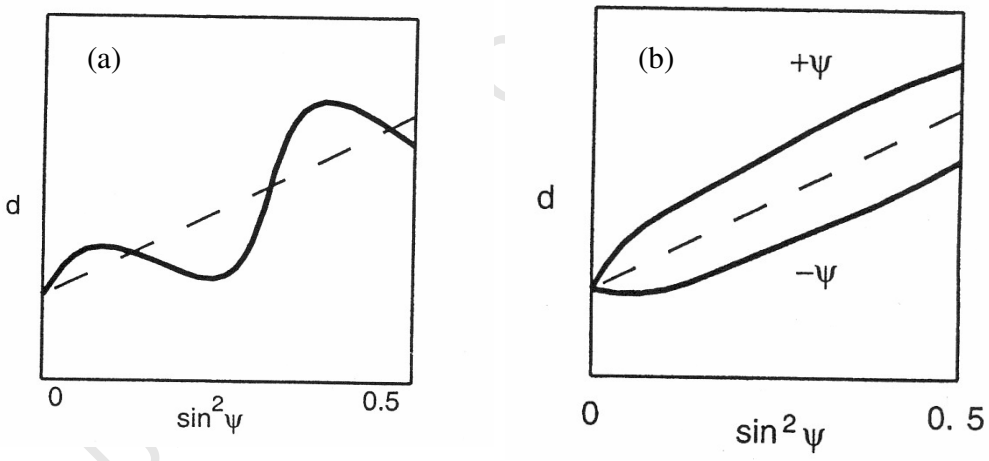

Figure 5.10: $\sin^2\psi$ *responses for (a) materials exhibiting texture, (b) a triaxial stress state [5.30].*

Non-linearity of a $\sin^2\psi$ plot is also observed in the case of steep stress gradients. Since a fair amount of the radiation is not scattered at the surface of the sample, but in the region below, the diffracted X-rays always carry some information from a region where the stress is not necessarily biaxial. Therefore

due to different strains in the surface and in the bulk, a change in slope should be expected. One approach which takes the stress gradients into account is to describe the stress components as averages over the depth z probed:

$$\sigma_{ij}^{'} = \frac{\int \sigma_{ij}(z)\exp(-z/\tau)dz}{\int \exp(-z/\tau)dz}, \qquad (5.32)$$

where τ is the penetration depth, given by

$$\tau = \frac{\sin\theta\cos\psi}{2\mu}, \qquad (5.33)$$

where μ is the linear absorption coefficient. The change of notation of depth from $\times$ to z is motivated for compatibility with normal usage in the field of stress analysis. The penetration depth τ given by Eq. (5.33) is for measurements made in the side-inclination geometry [5.23], as discussed later. The penetration depth τ is defined by the condition that the intensity I of the X-rays passing through a material of this thickness is $1/e$ of the primary intensity I_0. The penetration of the X-ray beam depends, due to the linear coefficient μ, on the material under investigation, the Bragg angle θ, and the tilt angle ψ. The observed stress value is therefore the weighted sum of all the underlying stresses in the depth penetrated by the X-ray, as expressed in Eq. (5.32).

d) Determination of the stress depth profile

As mentioned above, residual strain and stress profiles determined by X-ray diffraction in the near surface region of polycrystalline materials are always averaged quantities. A convenient measure of the irradiated depth is the $1/e$ penetration depth τ in the Eq. (5.31). Thus, all measured quantities are in fact functions of τ, rather than a function of the depth z beneath the surface. The τ-

profile of strain and stress can be determined by varying the incident beam angle [5.35 - 5.37], or by varying the wavelength and reflection used [5.31, 5.38, 5.39].

For a quantity q determined by a diffraction experiment, *e.g.* a stress or strain component, the relation between the average quantity $\langle q(\tau)\rangle$ measured as a function of τ, and z-profiles of that quantity is

$$\langle q(\tau)\rangle = \frac{\int_0^D q(z)dP'}{\int_0^D dP'}, \tag{5.34}$$

where

$$dP' = c\, e^{\frac{-z}{\tau}} dz\,, \tag{5.35}$$

where c is a constant, D is the sample thickness in the z direction, and $dP'/\int_0^D dP'$ is a weighting factor expressing the normalized diffracting power from the element dV at depth z.

Eq. (5.34) can be written as

$$\langle q(\tau)\rangle = \frac{\int_0^D q(z)e^{-\frac{z}{\tau}}dz}{\int_0^D e^{-\frac{z}{\tau}}dz}. \tag{5.36}$$

By integrating the denominator in Eq. (5.36), the following expression is obtained

$$\int_0^D e^{-\frac{z}{\tau}}dz = \tau\left(1-e^{-\frac{D}{\tau}}\right). \tag{5.37}$$

If D is much larger than τ value, then Eq. (5.37) is approximately equal to τ. D can also be assumed to be infinity without significantly affecting the value of the integral in the numerator. With these assumptions, Eq. (5.36) becomes

$$\tau\langle q(\tau)\rangle = \int_0^\infty q(z)e^{-\frac{z}{\tau}}dz = L[q(z)]. \tag{5.38}$$

The right hand side of Eq. (5.38) is the Laplace transform of *q(z).* Therefore the *z*-profile is the inverse Laplace transform of the left hand side of Equation (5.38), *i.e.*

$$q(z) = L^{-1}[\tau\langle q(\tau)\rangle]. \tag{5.39}$$

To obtain the z-profile, the normal procedure is to assume a function for the z-profile, calculate the τ-profile from Equation (5.36), compare it with the measured τ-profile data and repeat the process until a satisfactory fit is obtained to the τ data. A number of model functions, *e.g.* exponential functions [5.40], Jacobi polynomials [5.41], trigonometric functions [5.42], and Taylor polynomials [5.43] have been used, with least squares minimization to obtain the depth-resolved residual stresses.

Using the power series, the depth resolved stress can be modelled as

$$\sigma_{ij}(z) = \sigma_{ij}^0 + \sum_n a_{ij}^n z^n , \tag{5.40}$$

where σ_{ij}^0 are the stress tensor components on the surface, the a_{ij} constants are the power series coefficients and n are the exponents of the series terms. Since we are dealing with the averaged stresses, one can write

$$\langle\sigma_{ij}(z)\rangle = \sigma_{ij}^0 + K_{ij}\tau_{\psi,\theta}^{n_{ij}}, \tag{5.41}$$

where σ_{ij}^{0} and K_{ij} are constants, and $\tau_{\psi\theta}$ is the measurement dependent penetration depth.

The functional dependence determined in [5.31] for near surface stress states, is adopted in this work. According this model, the depth dependence of the stress tensor components is given by

$$\sigma_{ij}(z) = \sigma_{ij,0} + a_{ij}z + b_{ij}z^2 + u_{ij}z^3, \tag{5.42}$$

and the corresponding averaged stress tensor components integrated over the depth, using

$$\int_0^\infty z^n e^{-\frac{z}{\tau}} dz = n!\tau^n, \tag{5.43}$$

are

$$\langle \sigma_{ij} \rangle = \sigma_{ij,0} + a_{ij}\tau_{(\psi,\theta)} + 2b_{ij}\tau_{(\psi,\theta)}^2 + 6u_{ij}\tau_{(\psi,\theta)}^3. \tag{5.44}$$

To obtain the average stress dependence with depth, a fitting of the integrated stress components to the different diffraction peaks is done. The strain $\varepsilon_{\phi\psi}$ obtained from each diffraction peak is considered as a data point, which is used to parametrize a tri-axial model stress function expressed in Eq. (5.29). The outcome of the parametrization is a set of six scalar functions, each one corresponding to one stress tensor component, as given in Eq. (5.44). To reduce the number of unknown coefficients in Eq. (5.44), the surface boundary conditions and the equations of equilibrium of the linear elasticity theory are used, *i.e.*,

$$\nabla \sigma_{ij} = 0, \; i,j = 1,2,3, \tag{5.45}$$

and

$$\sigma_{ij=0,z=0} = 0. \tag{5.46}$$

Eq. (5.45) imposes certain restrictions on the stress distribution possible within the material, so that all forces in the body must be in equilibrium. Eq. (5.46) reflects that, directly on the surface, all the components of the stress tensor perpendicular to the surface marked with the index 3 must vanish.

Taking the above considerations into account, the number of unknown coefficients in Eq. (5.44) is reduced to 20:

$$\begin{aligned}
\langle\sigma_{11}\rangle &= \sigma_{11,0} + a_{11}\tau_{(\psi,\theta)} + 2b_{11}\tau^2_{(\psi,\theta)} + 6u_{11}\tau^3_{(\psi,\theta)} \\
\langle\sigma_{22}\rangle &= \sigma_{22,0} + a_{22}\tau_{(\psi,\theta)} + 2b_{22}\tau^2_{(\psi,\theta)} + 6u_{22}\tau^3_{(\psi,\theta)} \\
\langle\sigma_{33}\rangle &= 2b_{33}\tau^2_{(\psi,\theta)} + 6u_{33}\tau^3_{(\psi,\theta)} \\
\langle\sigma_{12}\rangle &= \sigma_{12,0} + a_{12}\tau_{(\psi,\theta)} + 2b_{12}\tau^2_{(\psi,\theta)} + 6u_{12}\tau^3_{(\psi,\theta)} \\
\langle\sigma_{13}\rangle &= a_{13}\tau_{(\psi,\theta)} + 2b_{13}\tau^2_{(\psi,\theta)} + 6u_{13}\tau^3_{(\psi,\theta)} \\
\langle\sigma_{23}\rangle &= a_{23}\tau_{(\psi,\theta)} + 2b_{23}\tau^2_{(\psi,\theta)} + 6u_{23}\tau^3_{(\psi,\theta)}
\end{aligned} \quad . \qquad (5.47)$$

The unknown coefficients are obtained through a non linear fit procedure using Mathematica™ software [5.44]. This program fits the parameters of the mathematical model to the measured strain values with a weighted non-linear Levenberg-Marquardt fit procedure [5.45]. Details of the nonlinear fit procedure are found in Appendix A.

The elastic constants used in this stress determination process take the X-ray elastic constants, *i.e.* s_1^{hkl}, and $\frac{1}{2}s_2^{hkl}$ into account. The reason for this approach is that the material under investigation, polycrystalline titanium, has a hexagonal close packed structure, and therefore, as other hcp materials, it presents anisotropic elastic and plastic properties. The X-ray elastic constants based on the Kröner model [5.46, 5.47] were used in this investigation.

5.3.2 Experimental details

5.3.2.1 Radiation source and beamline

a) Synchrotron radiation source

The principle of every synchrotron radiation source is that, for a bunch of electrons accelerated in a ring to speeds close to the speed of light, the centripetal acceleration due to the curvature of the path causes the electrons to emit electromagnetic radiation [5.48]. Using the example of the Brazilian synchrotron source, Laboratório Nacional de Luz Sincrotron (LNLS), Campinas, used in this study, the main components of a synchrotron radiation facility are shown in Fig. 5.11. A linear accelerator (LINAC), not shown in Fig. 5.11, accelerates electrons to 120 MeV before feeding them into a booster synchrotron. The booster raises the beam energy to a starting energy of 500 MeV. The accelerated electron beam is then injected into the storage ring, where it is accelerated to, and maintained at the operating energy of 1.37 GeV. The photons produced at the bending magnets are available for users through the individual beamlines.

(a)

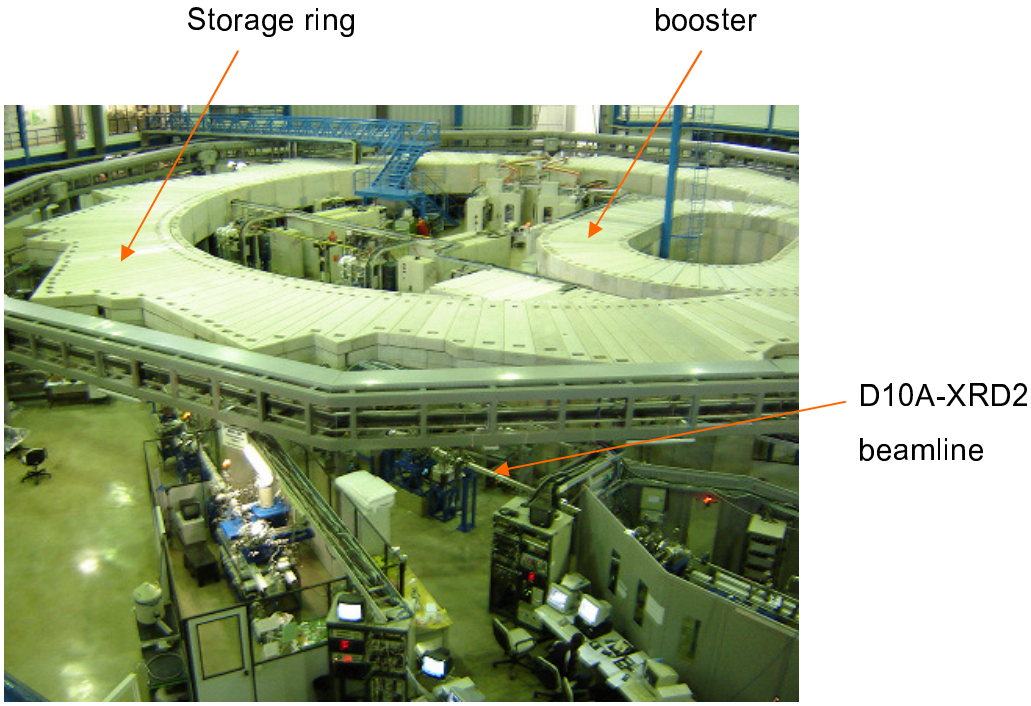

(b)

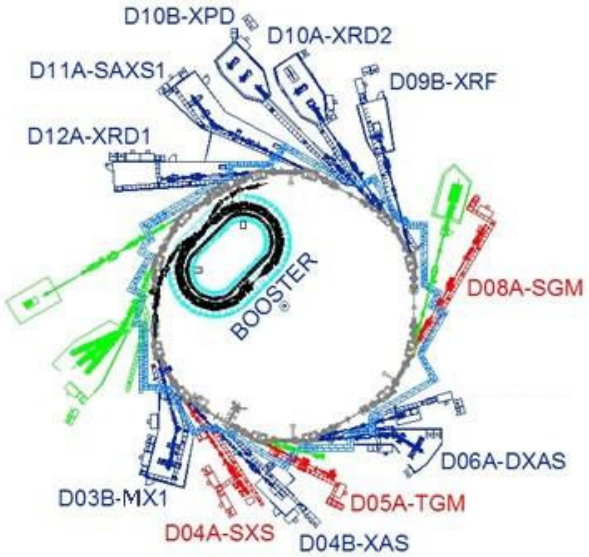

Figure 5.11: Synchrotron radiation source at Laboratório Nacional de Luz Sincrotron (LNLS) Campinas, Brazil. (a) Photograph showing the booster, the storage ring, and the beamline used. (b) Schematic representation of the facility indicating beamlines using VUV and soft X-rays (red) and beamlines using hard X-rays (blue). beamlines indicated in green are under construction, D10A-XRD2 is beamline used for the experiment described in this work [5.49].

According to general principles of classical electrodynamics, accelerated charged particles always radiate electromagnetic waves. The power radiated by non-relativistic electrons is given by

$$S = \frac{e^2}{6\pi\varepsilon_0 m_0^2 c^3}\left(\frac{dp}{dt}\right)^2, \tag{5.48}$$

where e is the charge and m_0 the mass of an electron, c is the velocity of light, ε_0 is the dielectric constant of the vacuum, and $p = m_0 v$ is the particle momentum. In case of relativistic particles, a Lorentz invariant form of Eq. (5.48) is applied, where the time transforms according to

$$dt \to d\tau = \frac{1}{\gamma}dt, \quad \gamma = \frac{E}{m_0 c^2} = \frac{1}{\sqrt{1-\beta^2}}, \quad \beta = \frac{v}{c}. \tag{5.49}$$

With these transformations, the radiation power of a charged relativistic particle becomes

$$S = \frac{e^2 c}{6\pi\varepsilon_0 \left(m_0 c^2\right)^2}\left[\left(\frac{dp}{d\tau}\right)^2 - \frac{1}{c^2}\left(\frac{dE}{d\tau}\right)^2\right]. \tag{5.50}$$

The radiation depends strongly on the angle between the direction of particle velocity and the direction of acceleration. From the two extreme cases, linear acceleration, where $(dv/d\tau) \| v$, and circular acceleration where $(dv/d\tau) \perp v$, the latter provides the basic concept for quantifying the synchrotron radiation output. If the accelerating force F acts on a charged particle perpendicular to the direction of motion, the emitted radiation power is significantly higher than in the case of linear acceleration. Since electrons in a synchrotron are moving through a magnetic field B, the accelerating force F is given by

$$F = ev \times B, \quad F \perp v. \tag{5.51}$$

Because of the direction of the accelerating force the resulting trajectory is a circle. Therefore, the energy of the particle is not changed. The term $dE/d\tau$ in Eq. (5.50) vanishes and the radiation power can be written as

$$S = \frac{e^2 c}{6\pi\varepsilon_0 \left(m_0 c^2\right)^2}\left(\frac{dp}{d\tau}\right)^2 = \frac{e^2 c\gamma^2}{6\pi\varepsilon_0 \left(m_0 c^2\right)^2}\left(\frac{dp}{dt}\right)^2. \qquad (5.52)$$

The trajectory being a circle, the derivative of the momentum with respect to the time becomes

$$\frac{dp}{dt} = p\omega = p\frac{v}{R}, \qquad (5.53)$$

where R *is* the bending radius of the trajectory. For ultra-relativistic particles with $\gamma \gg 1$, i.e. $\gamma > 1000$, the energy is $E = pc$. Therefore Eq. (5.57) can be written as

$$S = \frac{e^2 c}{6\pi\varepsilon_0 \left(m_0 c^2\right)^4}\frac{E^4}{R^2}. \qquad (5.54)$$

Eq. (5.54) shows the strong energy dependence of the radiation emitted by charged particles traveling along a circular trajectory. It also shows a strong dependence of the radiation on the particle mass m_0. This explains the choice of electrons to generate such radiation, instead of using protons.

Eq. (5.54) gives the total power of radiation emitted for all photon energies or wavelengths. For practical purposes three properties, the brilliance, the brightness, and the flux, characterize a synchrotron light source [5.50]. The brilliance is defined as the number of photons per unit time area, solid and bandwidth $(\Delta E/E)$. The normal units applied for solid angle and area are mrad^2 and mm^2, and a bandwidth of 1% is used. Integrating over the area yields the brightness, which is the number of photons per unit time, solid angle, and

bandwidth. Further integrating over the vertical divergence over the beam gives the quantity normally quoted for any experiment, the flux which is the number of photons per unit time, bandwidth and angle in the horizontal plane. When normalized to the energy of the beam current the brilliance has a universal form [5.50] as seen in Fig.5.12.

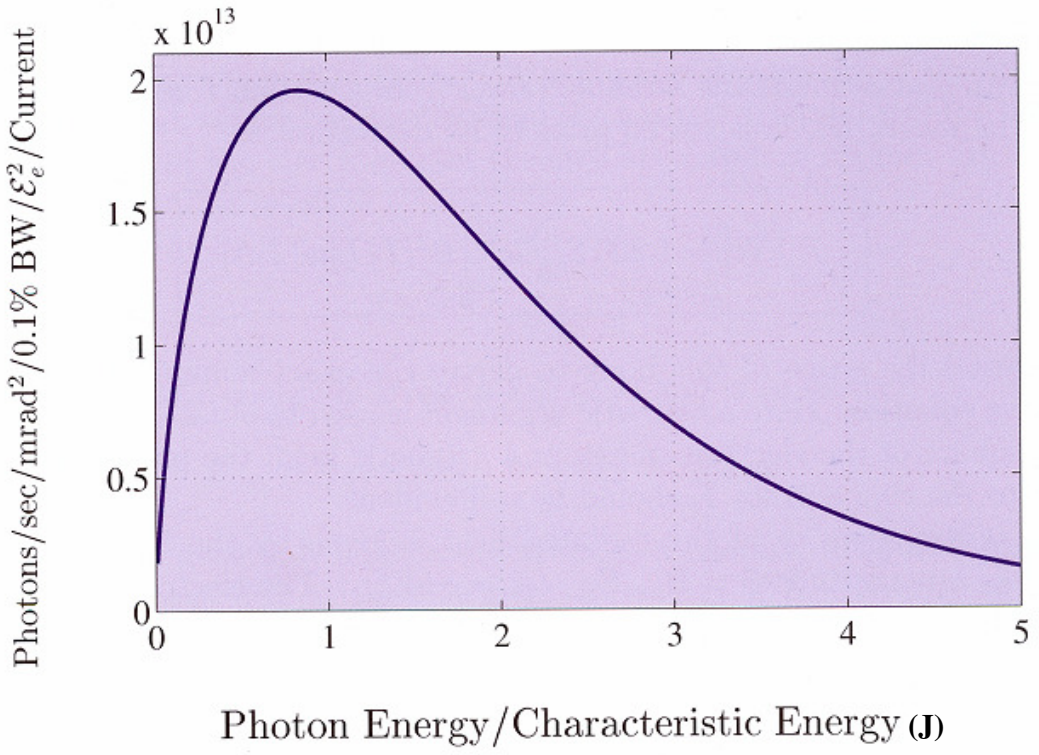

Figure 5.12: The brilliance spectrum from a bending magnet , normalized by the square of the electron energy and the beam current as a function of the ratio of the photon energy to the electron beam energy [5.51].

b) D10A-XRD2 beamline

As seen in Fig. 5.11b all the beamlines are located at the 12 dipole bending magnets. The photon flux for any of the dipole magnets is shown in Fig 5.13. The selection of the spectral region used in an experiment depends on the characteristics of the particular beamline. The D10A-XRD2 beamline used in this

work covers the spectral range of X-rays,with a flux ranging from $5x10^7$ to10^{12} photons/mrad/sec/0.1%bw, as seen in Fig. 5.13. The main application areas for this equipment are high-resolution X-ray diffraction, resonant X-ray magnetic diffraction and grazing incidence diffraction but it is also adapted for measurements of diffraction-enhanced tomography and phase-contrast radiography [5.52].

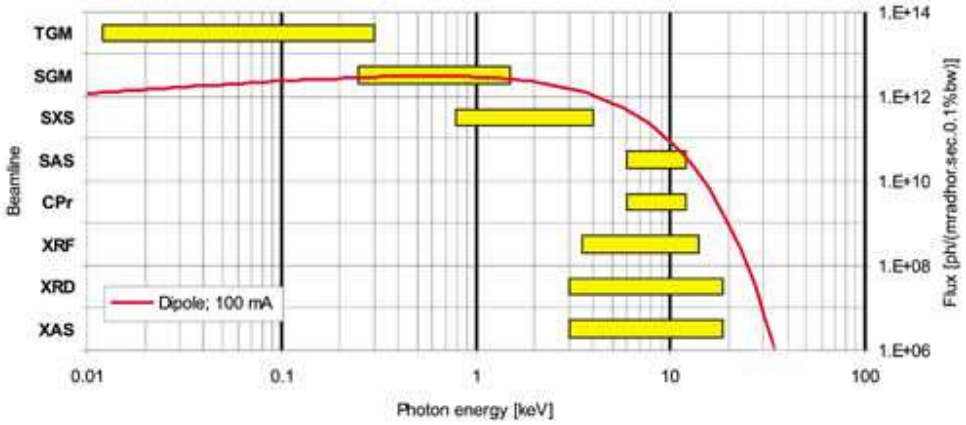

Figure 5.13: Spectral flux of the bending magnets at the LNLS, indicating regions used by the individual beamlines [5.49].

In the framework of this study, preliminary work [5.53] showed that CuKα radiation produced by a conventional X-ray tube, allows, in principle, probing of the change in stress due to implantation. However, the unacceptably long measuring time using conventional X-rays suggested employing synchrotron radiation, and the combination of the available photon energy, and the flexibility of the goniometer, as described below, made it possible to use this particular beamline.

c) Synchrotron beamline optics

There are two main optical elements in the D10A-XRD2 beamline. The first is a vertically focusing, cylindrically bent Rh-coated ultra-low-expansion X-ray mirror shown, as part (ii) in Fig. 5.14. The role of the mirror is to reflect all energies below 15 keV, through the beamline.

The second element, indicated as (iii) in overall layout of the beamline in Fig. 5.14, is the double-bounce monochromator consisting of a flat water-cooled first crystal and a dynamically bent sagittal crystal. The monochromator is located in a one-to–one configuration regarding the source-to-monochromator and monochromator-to-sample distances, allowing an optimized configuration of the beam size at the sample and the horizontal angular acceptance. Other beamline elements, such as motorized slits, X-ray beam position monitors, adjustable filters, vacuum flight paths, a detector to monitor the intensity of the primary beam, primary beam counter are connected in the end station (iv). The energy range covered by the beamline optics is between 3 keV and 15 keV. The lower limit is imposed by the absorption losses in the Be windows, and the upper limit is fixed by the source and cut-off energy of the X-ray mirror. The highly parallel beam has, at the sample position at the centre of the six-circle goniometer, segment (v) a size of the order of 0.5×1 mm^2.

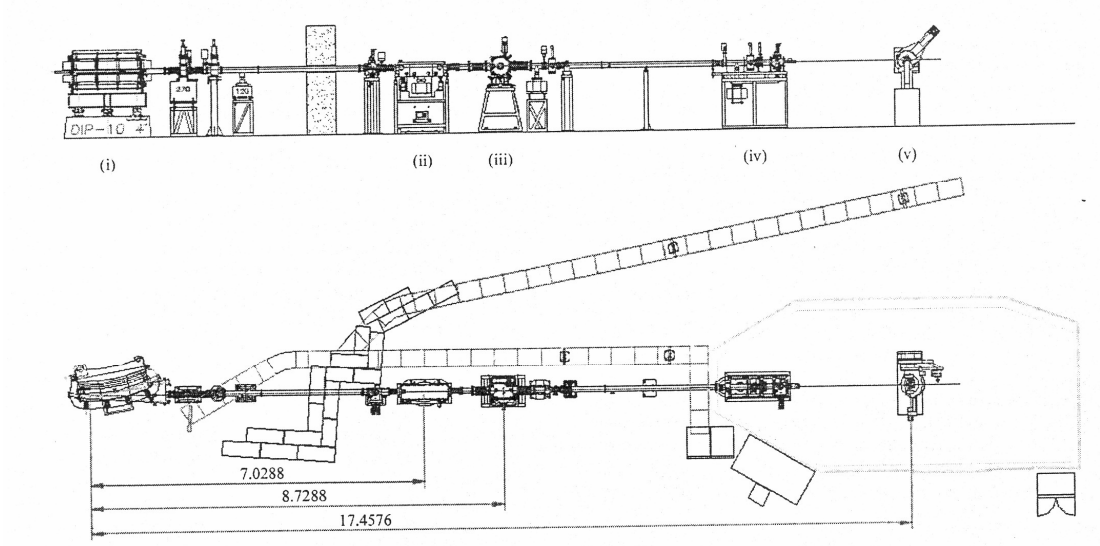

Figure 5.14: (a) Side and top views of the main components of the XRD2 beamline at LNLS: (i) bending-magnet source, (ii) X-ray mirror, (iii) double-crystal monochromator, (iv) end-station, (v) six-circle diffractometer [5.52]

From a user point of view the primary component of the beamline is the Huber six-circle diffractometer, in vertical scattering geometry, on which the sample to be investigated is mounted. The second part of the diffractometer is the scintillation counter which records the diffracted radiation from the material under investigation. Fig. 5.15 shows a photograph of the diffractometer used to carry out our experiment, as well as schematic representation of the goniometer indicating the degrees of freedom for moving sample and detector during the experiment. The axes in the figure are labeled according to the generic names used for all goniometers. In the side inclination geometry used here, the ψ-tilt corresponds to the movement of the chi goniometer.

The goniometer is operated using SPEC software [5.54] in a PC-based Linux environment using separate computers for control and data storage. For alignment of the goniometer axis in the beam, an additional detector is positioned in the beam axis behind the diffractometer.

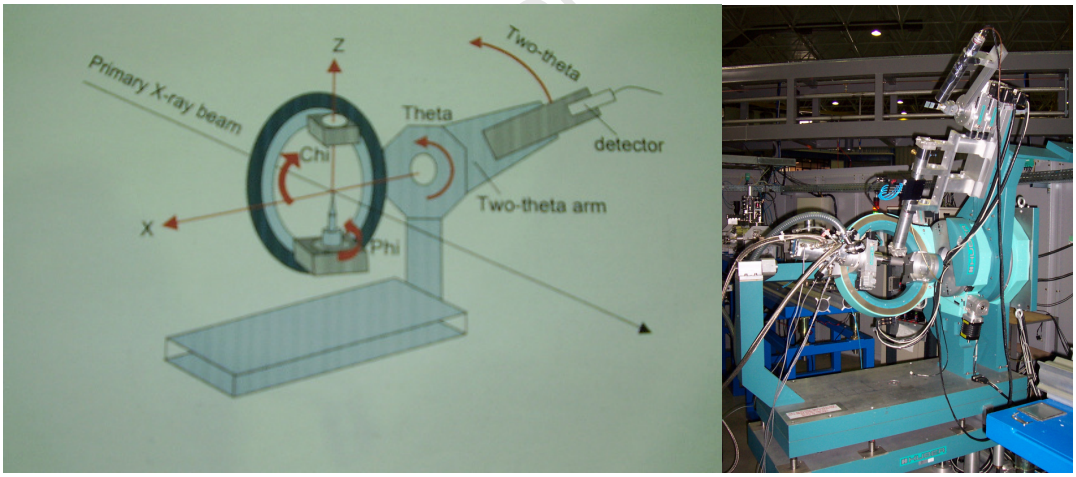

Figure 5.15: (a) Schematic of the goniometer showing the four degrees of freedom of movement used in the experiment: theta, chi, phi, and two-theta. (b) Photograph of the diffractometer at LNLS.

5.3.2.2 Sample alignment

It is important to underline here that, not only at the start of the experiment, but whenever the beam has been off, an alignment of the beam must done. This is achieved by monitoring the direct beam with a CCD camera and adjusting until it has a defined profile and position on a TV monitor. The sample surface must then be accurately positioned in the centre of the goniometer axis, and simultaneously in the centre of the beam. This is achieved by ensuring that the sample surface is parallel to the beam and bisects it at theta equal to zero. Before mounting any sample, the following alignment to make sure that the goniometer axis is in the beam is required:

1. Mount a pin in the position of the sample on the goniometer head.
2. Observe visually that the point does not move on rotation using a telescope. If so, then the pin point is on the goniometer axis.
3. Use the x and z movements of the goniometer table to bring the pin into the beam so that it cuts half of the beam.

Once alignment of the goniometer axis and beam is achieved, the pin is removed and the sample mounted. For each new sample mounted, the important steps for the alignment are as follows:

1. Line up the z movement on the goniometer so that the sample cuts half of the beam.
2. Line up the theta circle to bring the sample surface parallel to the beam.
3. Move chi to 180° and repeat the line up theta procedure.
4. Repeat steps (1) to (3) until the sample surface is parallel to the beam.
5. Turn to the phi circle to 90° and repeat steps (1) to (4).
6. Repeat steps (1) to (5) until the alignment is achieved.
7. Define the zero position of the 2θ circle.

To realign during a measurement, after the beam has been switched off, the above steps are repeated using the sample, except that the z-motion of the goniometer table is used instead of the sample.

5.3.2.3 Measurement procedure and data collection

The diffraction experiment was carried out on the unimplanted and implanted polycrystalline titanium samples, described in section 5.1 of this work. The beam energy used during the measurements was 11 keV, which corresponds to a wavelength of 1.125 Å. From a $\theta - 2\theta$ scan between 2θ angles of 24.8° and 81°, four reflection peaks were chosen for stress determination. Three low index peaks: (100) at θ=12.78°, (002) at θ=13.98°, and (101) at θ=14.60° were chosen for low penetration depth. These three peaks were measured within a θ range of 12.0° - 15.5° in sted sizes of 0.01°. The fourth peak (105) at θ=39.80° was chosen for high penetration depth and was measured, with the same step size as the previous peaks, in a range between 39.4° and 40.25°. The 16 ψ-tilts were provided by tilting the sample in side inclination mode, perpendicular to the scattering plane, at 10° intervals from 0° to 70°, and then 75°, 78°,80°, 82°, 84°, 86°, 88°, and 89°. The samples were measured at ϕ angles of 0°, 45°, 90°, 135°, 180°, 225°, 270°, and 315°.

The measurement for one sample took approximately 7 hours. The actual data recording time was relatively short in comparison to the time the goniometer requires to read the settings. To optimize the measuring time a new strategy for the goniometer movement was introduced to the operation of the diffractometer. In a normal approach, after measuring the diffraction pattern at the different ψ tilts the orientation of the sample was set back to its initial position, defined as the $\psi = 0$ setting, and the phi circle of the goniometer was moved to a new angle and the measurement continued by measuring the diffraction peaks at different ψ angles starting from 0 to the highest. For the improved approach a macro

script was written to control the different stepping motors to control the goniometer in a way that after the sequence of the ψ dependent measurements, a new ϕ angle was set and ψ measurements were performed in reverse order. This led to a significant reduction in the measurement time for each sample. The measurements were stored on the data computer as ascii file, which can imported to any other program, such as Origin.

5.3.2.3 Quality check of the stress determination

To confirm the adjustment of the diffractometer, a stress free tungsten powder sample was measured under the same conditions. The peak positions for the $\sin^2\psi$ curve, shown in Fig. 5.16, were determined by fitting a gaussian to the diffraction pattern. The curve shows no stress dependence, even for high ψ tilting, indicating the high quality of the alignment and the high quality of the measurement in general.

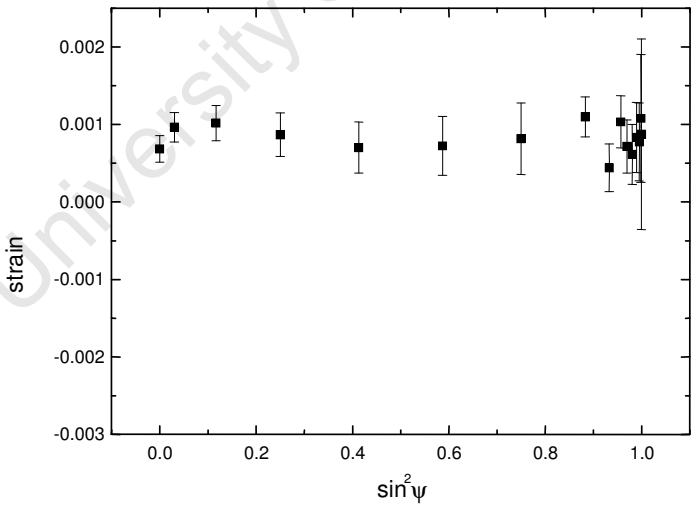

Figure 5.16: strain versus $\sin^2\psi$ curve of a stress free tungsten powder sample for the (100) reflection peak (2θ=29°). This reflection is very close to the (101) reflection chosen for the measurement (28.9°).

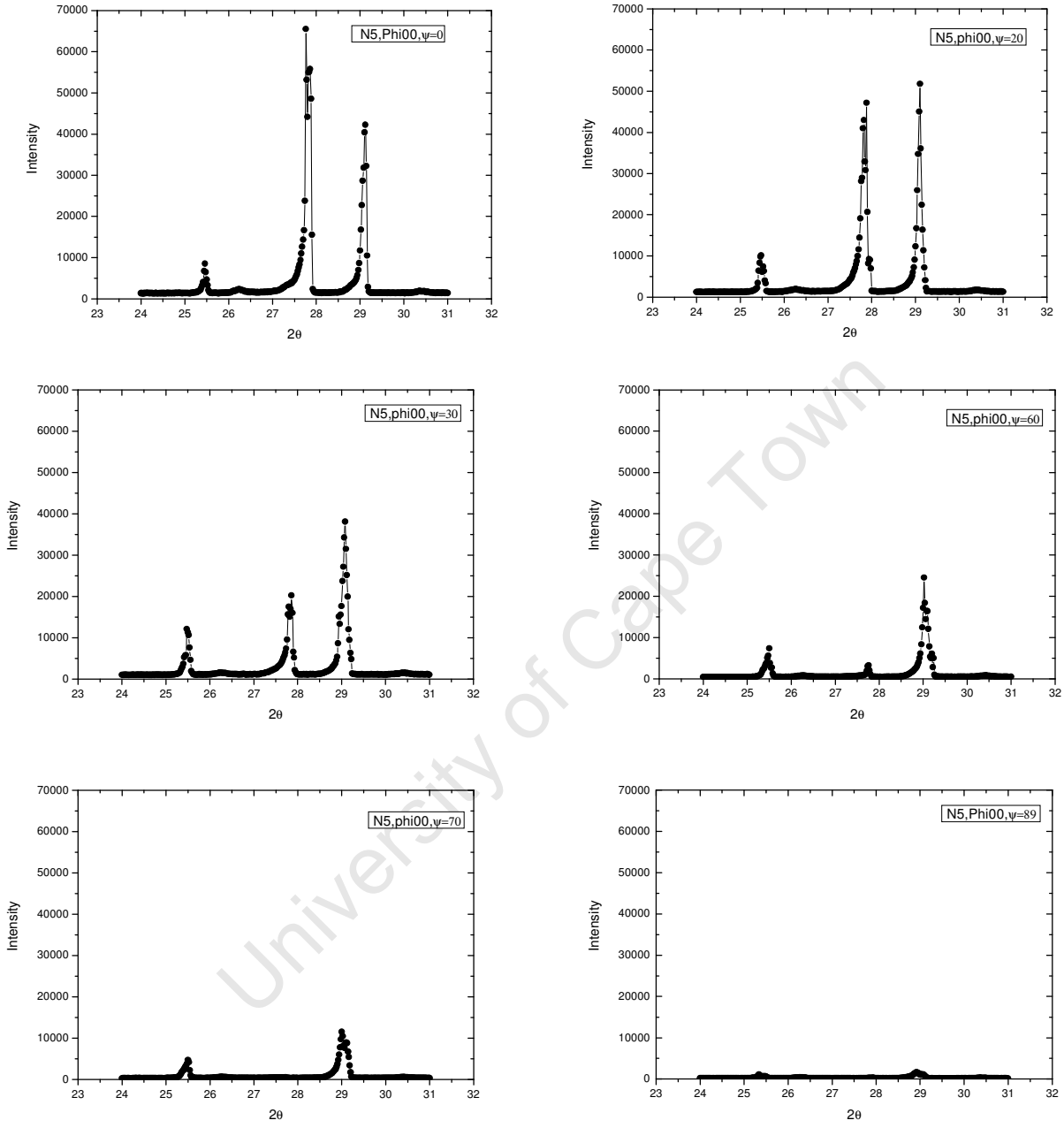

Figure 5.17: Raw diffraction peaks for (101) reflection for unpolished sample for ϕ = 0°, and corresponding ψ = 0°, 20°, 30°, 60°, 70°, 89°.

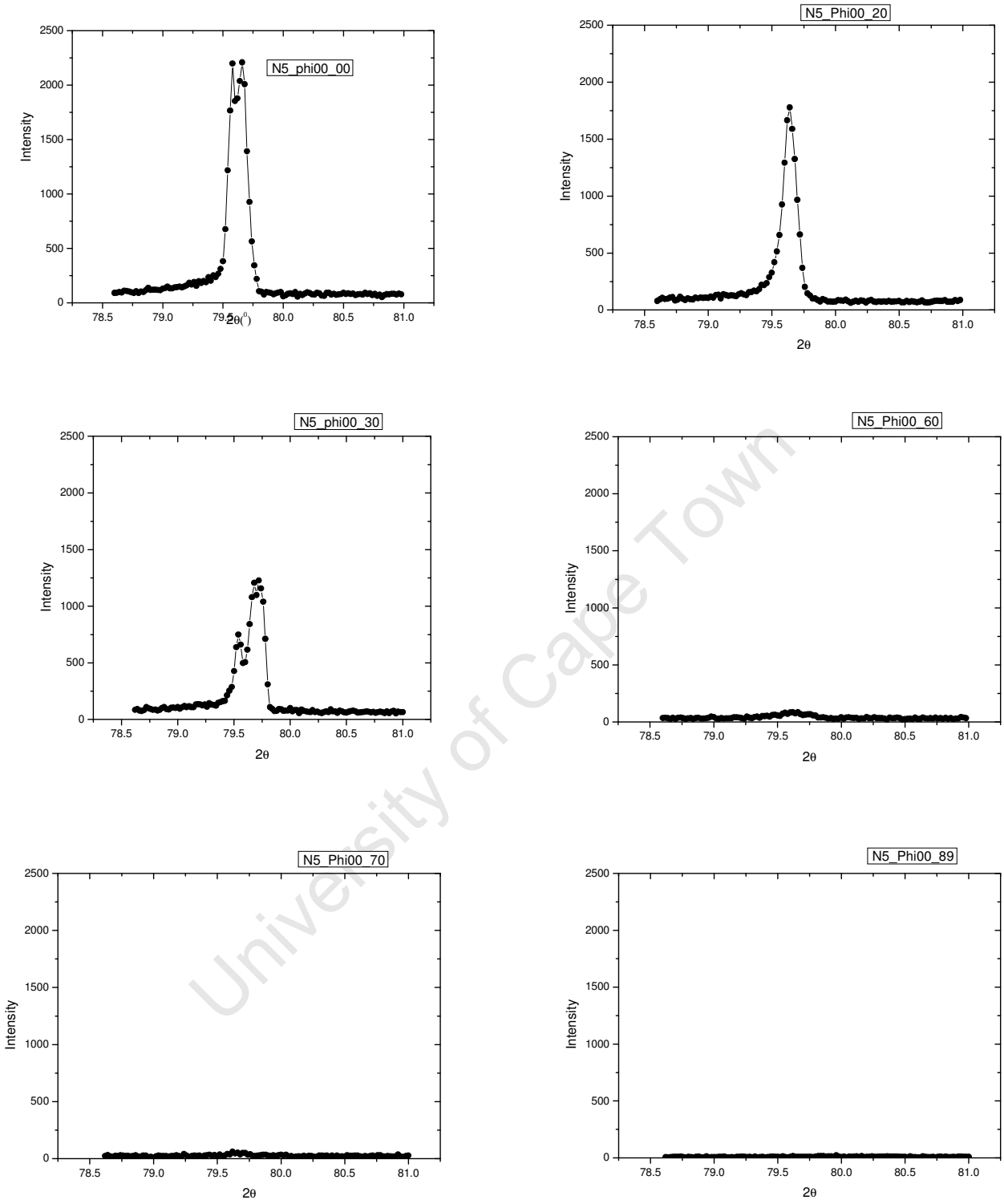

Figure 5.18: Raw diffraction peaks for (105) reflection for unpolished sample for ϕ = 0°, and corresponding ψ = 0°, 20°, 30°, 60°, 70°, 89°.

5.3.3 Peak position determination

The accuracy of stress determination using the X-ray diffraction method relies on both, the accuracy of the determination of the peak position and the goodness-of-fit of the assumed linear model that relates the peak shift to the sample orientation [5.55]. In the absence of systematic errors, it is the uncertainty in peak location due to random counting statistics that provides the major source of errors. The most frequently used methods for the determination of the angular position of X-ray diffraction intensity profiles are: the parabola method [5.56], least square fitting of a mathematical function [5.56, 5.57] the cross correlation method [5.56, 5.58], and the centroid (or the centre of gravity) method [5.59 - 5.61]. In the fitting process, common functions that are used include Gaussian, Lorentzian or pseudo-Voigt functions [5.62].

In this work, however, the centroid method was chosen to determine the peak position of the diffraction peaks. The use of cross-correlation or centroid has the advantage of being independent of the shape of the diffraction peak, but requires integration of the diffracted intensity over the entire peak profile [5.63]. This choice was informed by two observations. Firstly, the background is very low in the synchrotron diffraction patterns, leading to fewer inaccuracies in performing the integration. Fig. 5.17 and Fig. 5.18 show raw diffraction peaks (101) recorded for low Bragg and high Bragg angles (105), respectively (both for θ = 0°, and ψ = 0°, 20°, 30°, 60°, 70°, 89°). More importantly, however, was the fact that most of the peaks recorded present complex shapes. As seen from Fig. 5.19 most of the diffraction patterns show besides an asymmetry in the tails, multiple peaks which change with the measurement direction. This peak shape complexity in polycrystalline titanium was also reported in [5.64]. The difficulties with the peak shape make titanium a much more challenging material than other metals to perform residual stress determination.

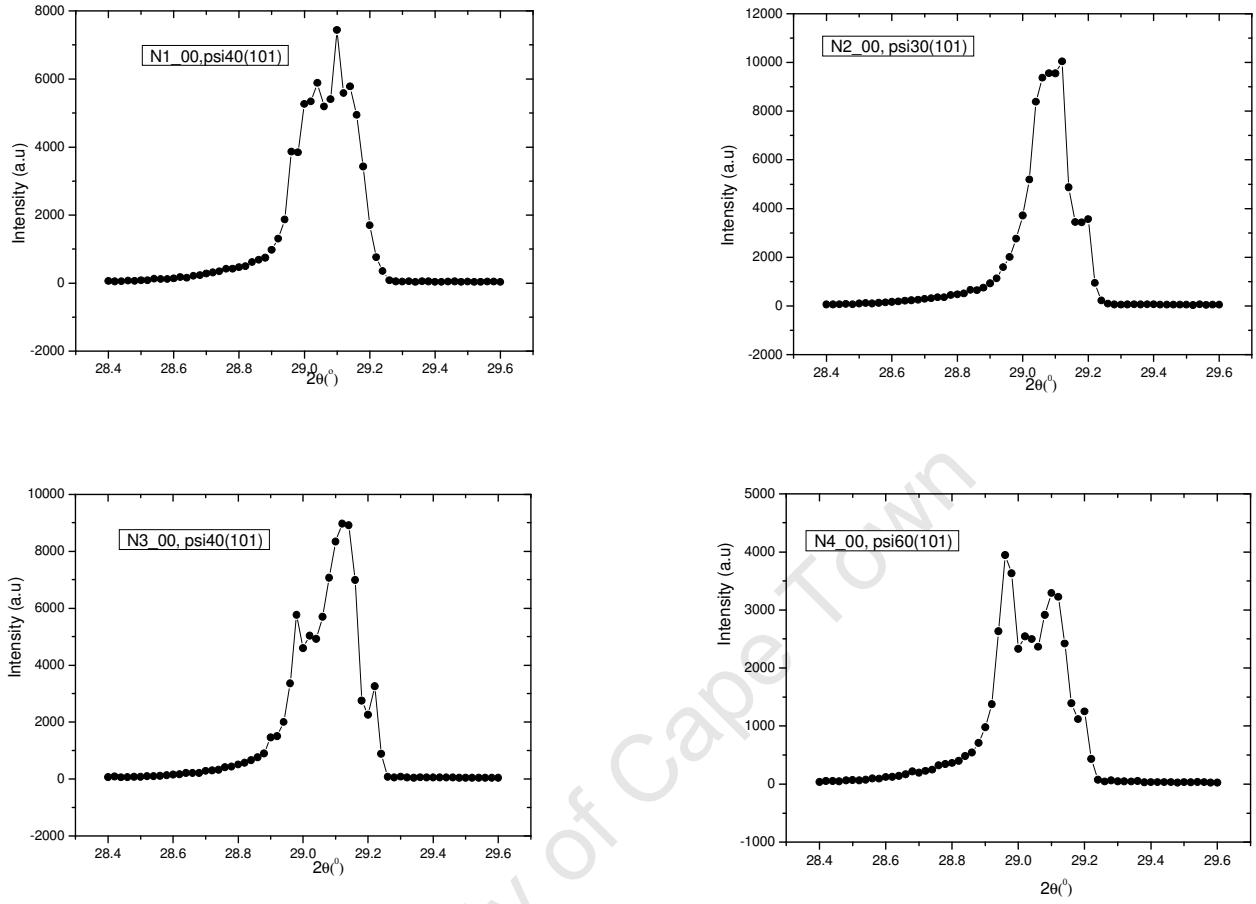

Figure 5.18: Complexity of the peak shapes. Asymmetry and multi-peaks in the peaks recorded are shown.

The centroid is defined [5.65] by

$$\langle 2\theta \rangle = \frac{\int 2\theta I(2\theta) d(2\theta)}{\int I(2\theta) d(2\theta)}, \qquad (5.61)$$

where $I(2\theta)$ is the intensity corresponding to the peak location at 2θ.

A special difficulty encountered in the experimental determination of the centroids of peak profiles comes from the slow asymptotic approach of the tails of the

profiles to the underlying background. Without incurring significant error, it has been found practicable to solve this problem by truncation of the profile at some arbitrary level above the background [5.65-5.68].

The variance, or squared standard deviation is directly associated with the centroid $\langle 2\theta \rangle$ as a measure of peak location, and is defined by

$$\sigma^2 = \langle (2\theta - \langle 2\theta \rangle)^2 \rangle = \frac{\int (2\theta - \langle 2\theta \rangle)^2 I(2\theta) d(2\theta)}{\int I(2\theta) d(2\theta)}. \qquad (5.62)$$

The accuracy of the centroid method is dependent upon the precision with which the intensity in the tails of the diffraction peak can be determined and upon the range of integration. Therefore it is very important to measure the diffracted intensity at small angular increments to provide a precise definition of the entire diffraction peak profile.

6 RESULTS

6.1 Krypton profile

Fig. 6.1 shows on a linear scale the experimental and simulated RBS spectra used to determine the krypton profile, in both unpolished (Fig. 6.1(a)-(e)) and polished (Fig. 6.1(f)-(i)) titanium samples. The same spectra are shown in Fig. 6.2 on a logarithmic scale. RUMP software [6.1] has been used for the simulations. The refinement procedure followed is based on modelling a multilayer structure with a Gaussian implantation profile, through a series of adjustments of layer thicknesses, compositions, projected range and full width at half maximum (FWHM), until the best agreement is found between the simulated spectrum and the experimental data. Details of the analysis method are given in Appendix C. For ease of comparison, the spectra for unpolished and polished samples, with the same fluence, are shown side by side in the figure.

The basic form of all spectra is, as expected for a bulk sample, a step function centered at energy of around 1.5 MeV corresponding to back-scattering from titanium. In the spectra, there are three particular features of interest. The first is the krypton signal, which is observable as a peak to the right of the titanium edge, at around 1.6 MeV, which increases with the fluence. The second is a shoulder, between channel 350 and 380, which can only be observed in all unpolished samples. This shoulder is associated with the presence of iron impurities in the titanium samples, as specified by the producer. The polishing process removes the iron impurities, as can be seen in the spectra of all the polished samples. The third feature, which is associated with the presence of oxygen in the samples, is a small step arising from the superposition of titanium signal and oxygen, observable at around channel 320 for the unpolished samples. This step is hardly visible in polished samples. Another indication of oxygen in the RBS spectrum is the sloping background, which suggests a gradient in the titanium concentration, or the presence of a light element which is

not titanium. The Kr peak is shown on an expanded scale in Fig. 6.3 (linear scale) and in Fig. 6.4 (semi-logarithmic scale). To investigate this further it was necessary to make use of resonant scattering from oxygen, at 3.045 MeV, as discussed in section 6.2 below.

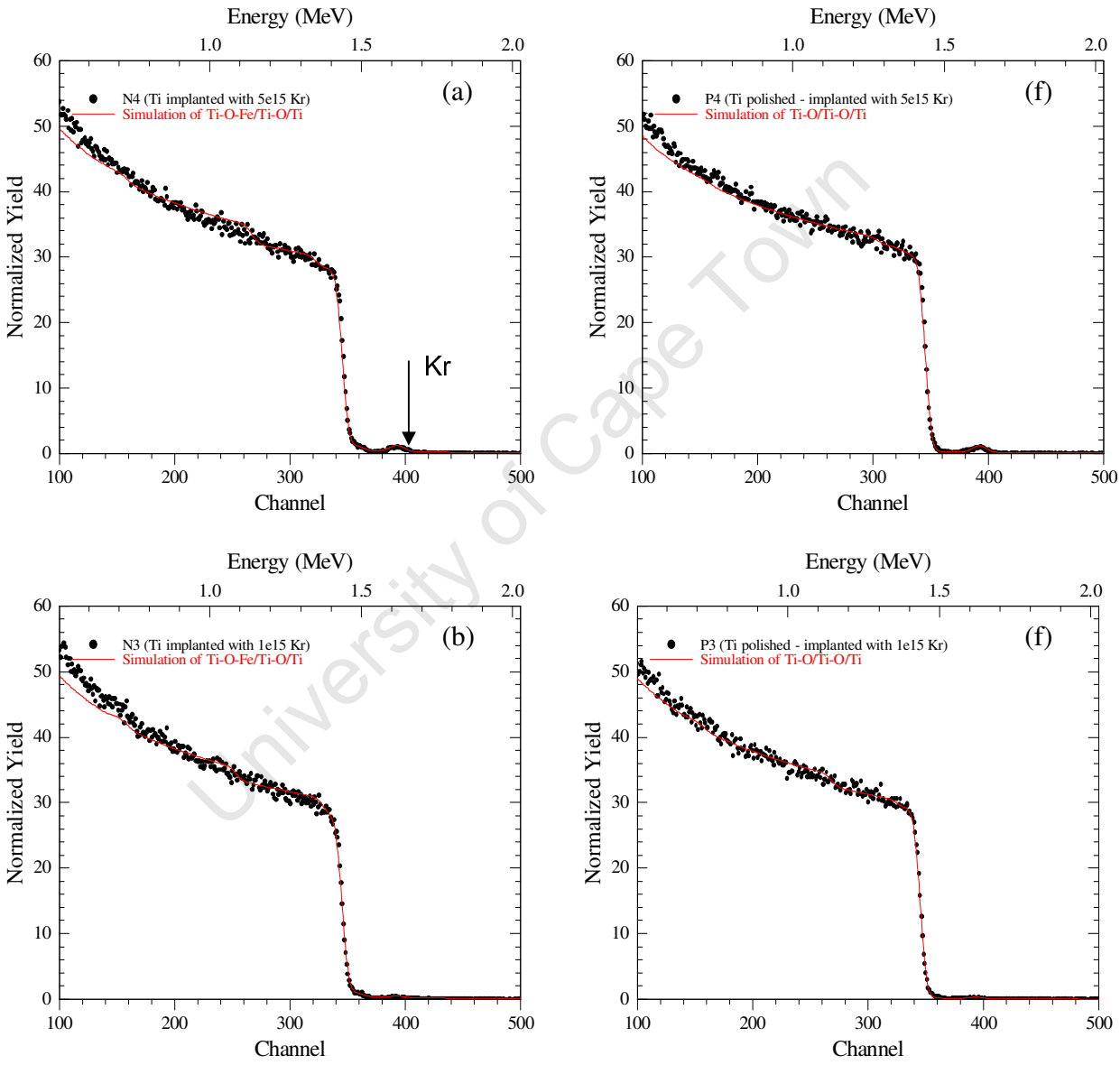

Figure 6.1: (a) to (e) Experimental and simulated spectra for unpolished samples. (f) to (i) Experimental and simulated spectra for polished samples (continued overleaf).

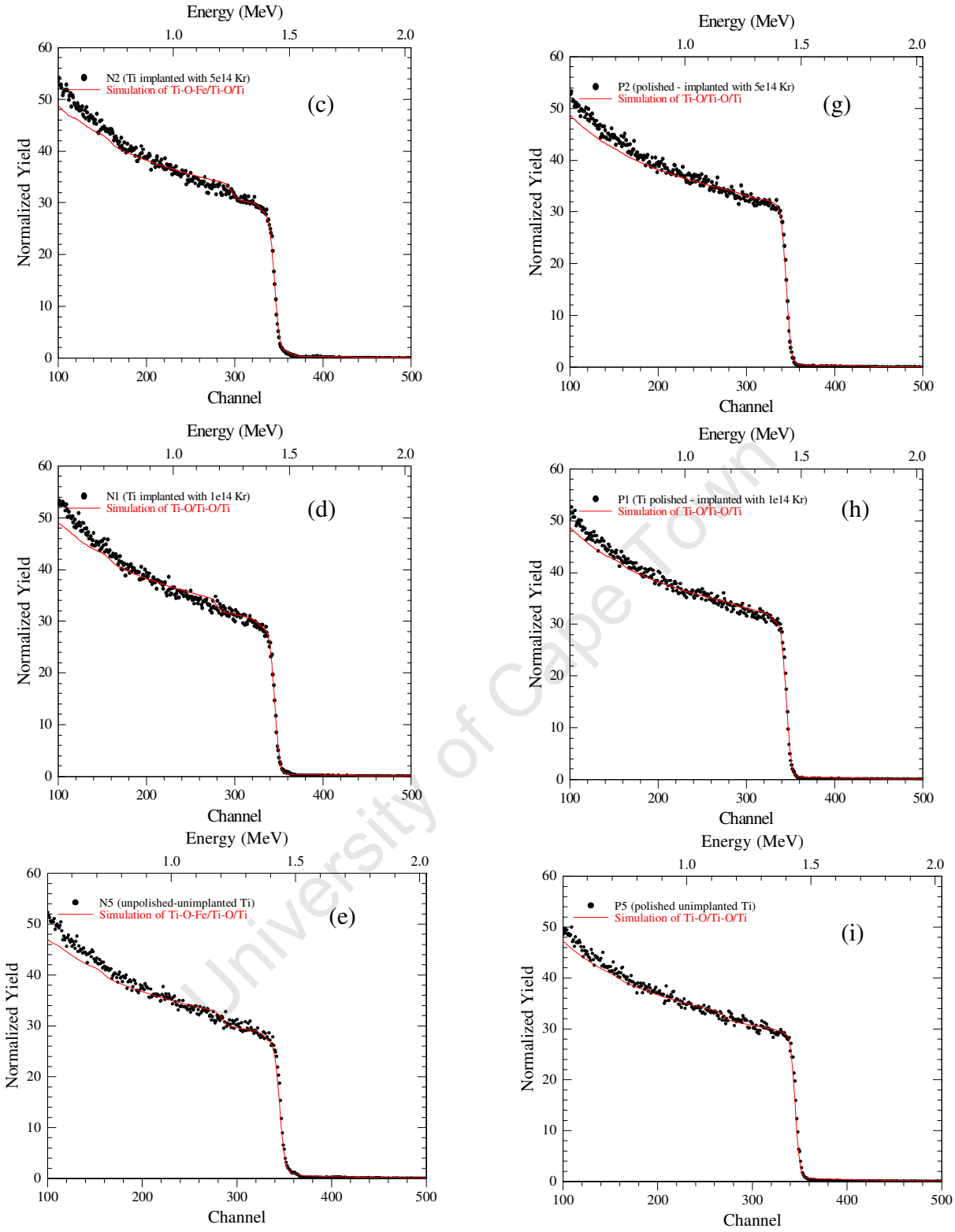

Figure 6.1: (a) to (e) Experimental and simulated spectra for unpolished samples. (f) to (i) Experimental and simulated spectra for polished samples (continued from previous page).

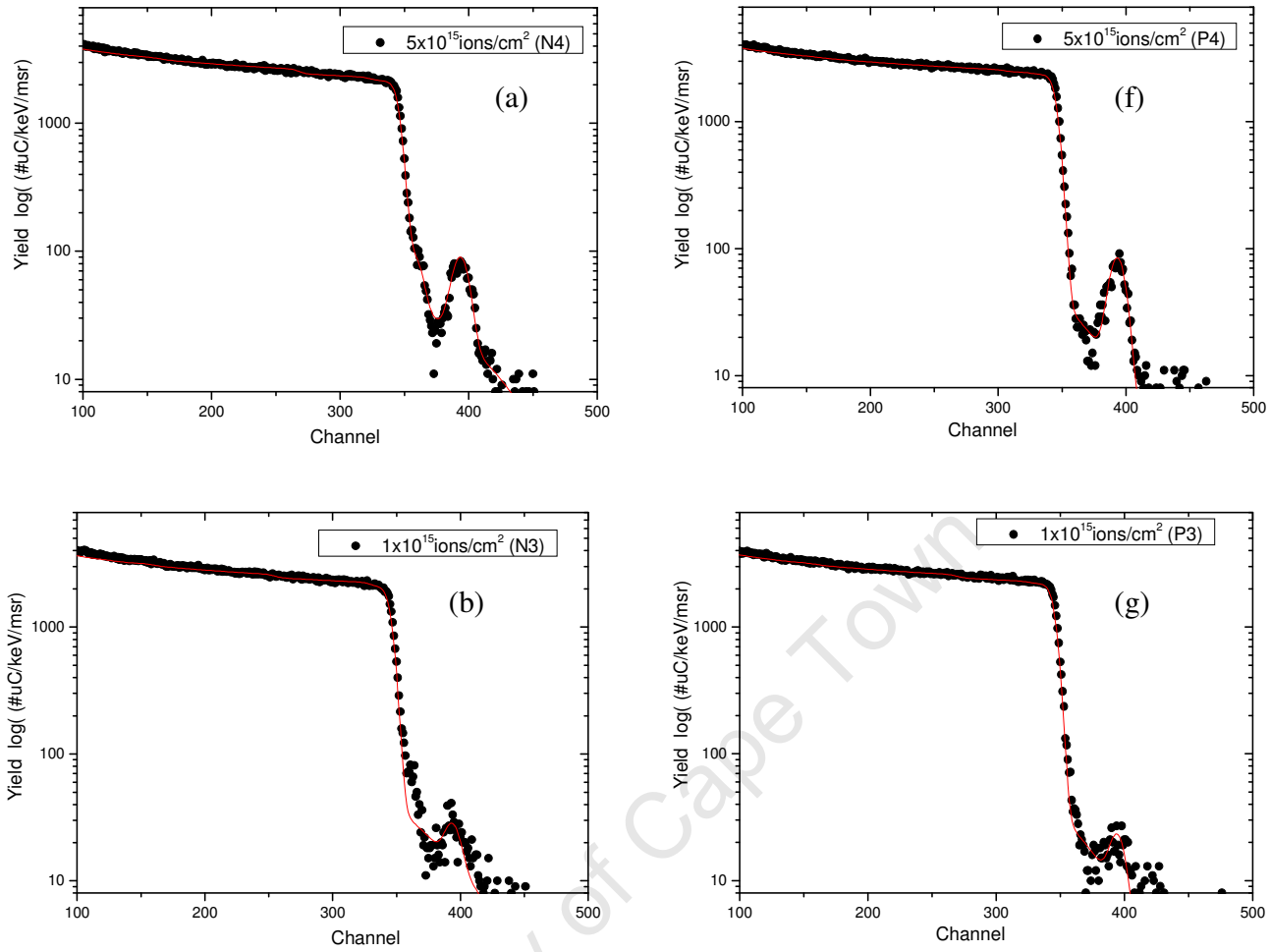

Figure 6.2: (a) to (e) Experimental and simulated spectra for unpolished samples. (f) to (i) Experimental and simulated spectra for polished samples (continued overleaf).

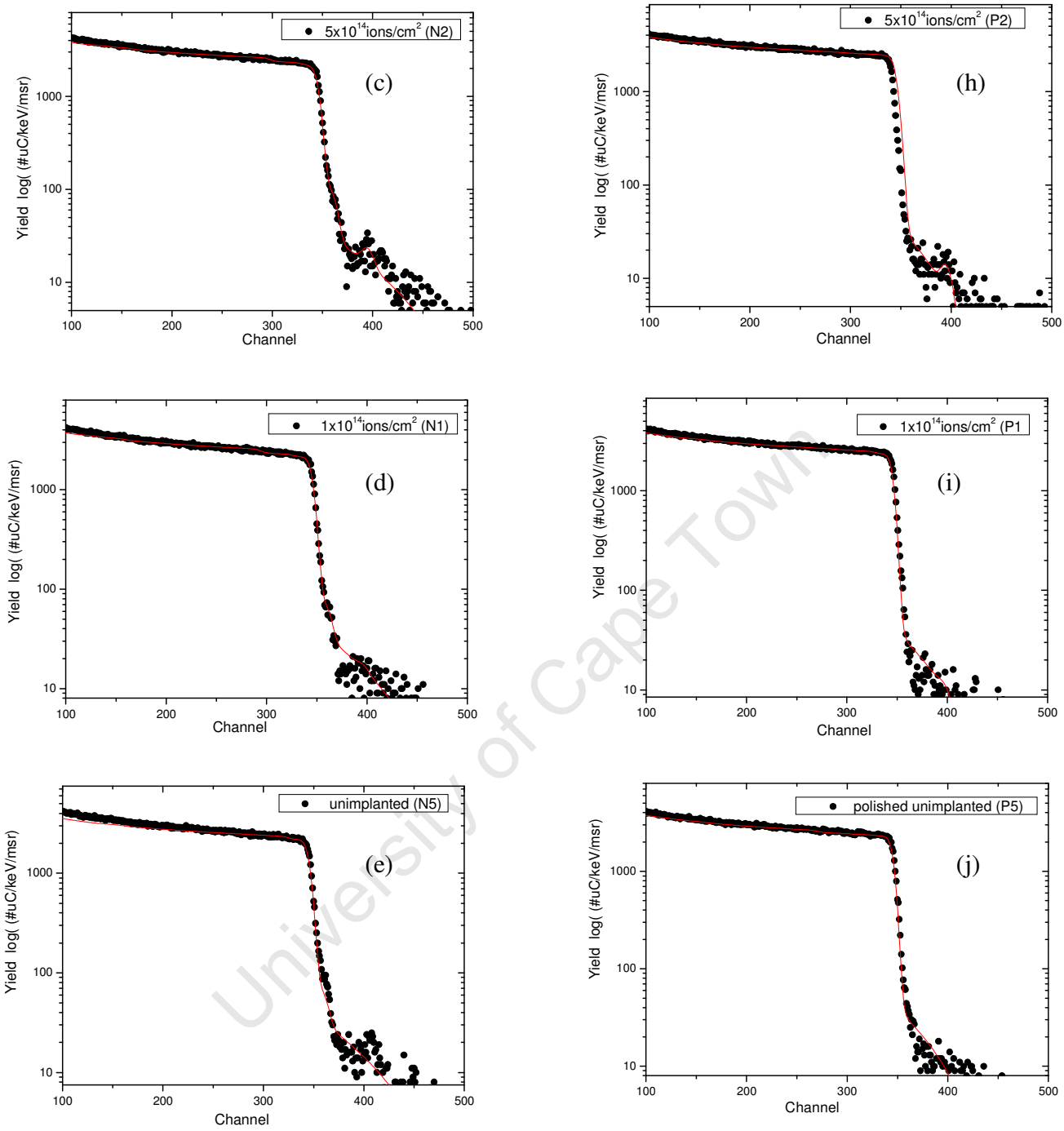

Figure 6.2: (a) to (e) Experimental and simulated spectra for unpolished samples. (f) to (i) Experimental and simulated spectra for polished samples (continued from previous page).

Modelling an isolated krypton peak on a small scale, using the RUMP package as described previously, allowed the determination of the krypton ion projected range, and the associated range straggling, for both the unpolished and polished samples. The procedure consists in first varying the projected range value in the simulation around the peak position while the straggling value is fixed, and then vice versa. This was repeated until the agreement was found. The results are shown in Fig. 6.3, for both unpolished (Fig. 6.3(a)-(d)) and polished (Fig. 6.3(e)-(h)) side by side with their corresponding residuals showing the accuracy and agreement of the model with the experimental data. The values for the estimated projected range and straggling, with associated errors, are summarized in Table 6.1. For convenience, and comparison with other techniques, all depths have been scaled to the mass density of elemental titanium. Although titanium is well-known to getter oxygen and other atmospheric gases, these are incorporated into the structure with the change in density being compensated by lattice expansion. It is obvious from these results that, as expected, as the fluence decreases the krypton concentration also decrease, leading to the increase in error of the projected range and the straggling. It can be observed, on the other hand, that for the same fluence the projected range is deeper, and the straggling higher in the unpolished samples than in polished samples.

For comparison, the SRIM Monte-Carlo code [6.2], version 2008 was used to calculate the projected range and straggling of krypton ions in titanium. From the calculations, a projected range of 698 Å and a straggling of 271 Å were obtained. The calculated projected range is about 18% higher than the value of the unpolished sample implanted the highest dose but the straggling value correlates with the measured value. At this dose, the difference between the calculated and measured projected range is reduced to about 15% corresponding to a value of about 673 Å if the sputtering process is taken into account, as seen in Table 6.1.

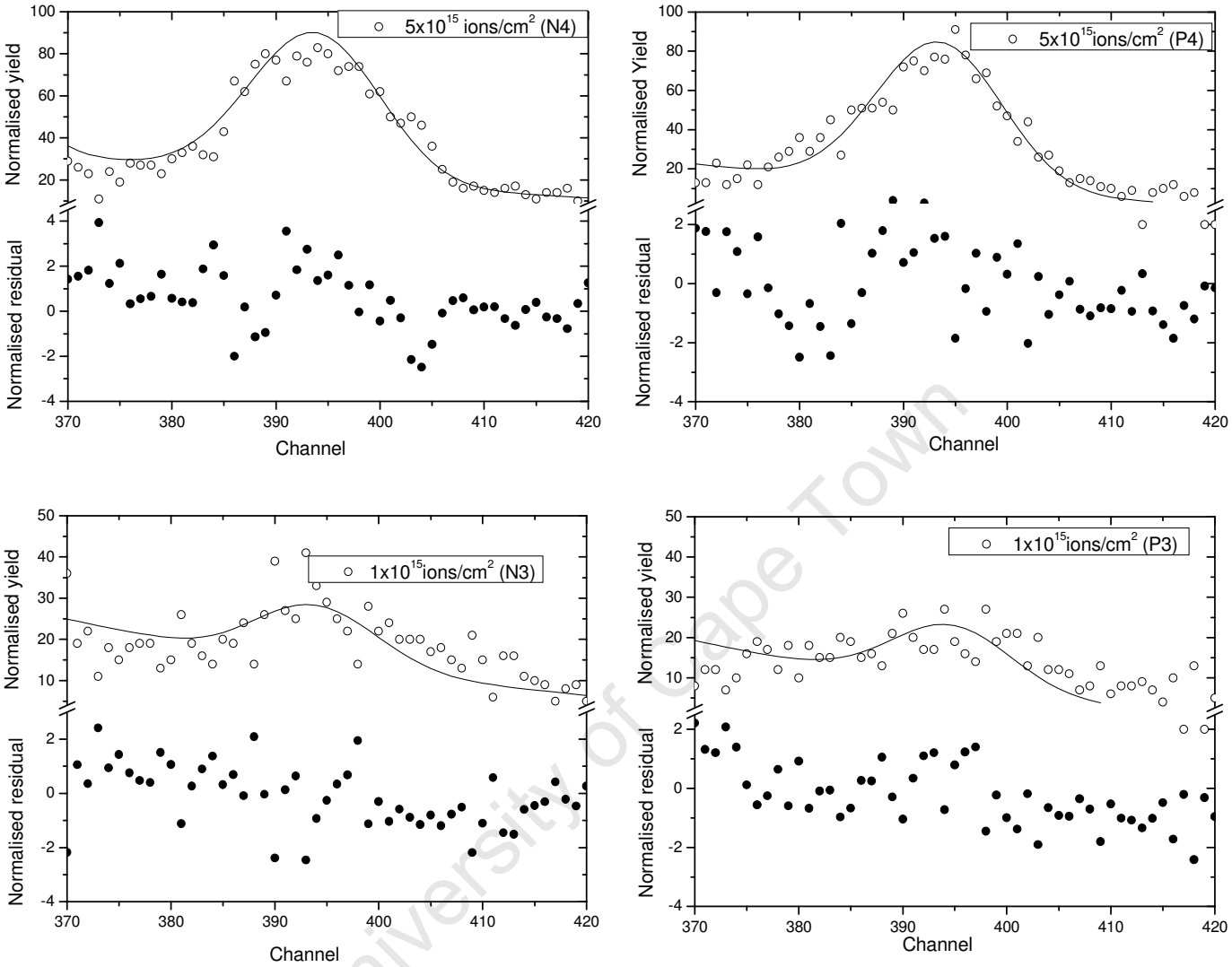

Figure 6.3: (a)-(d) Krypton peak on an expanded scale for unpolished samples. (e)-(h) Krypton peak on expanded scale for unpolished samples. The residuals for both samples are also shown on each graph at the bottom (continued overleaf).

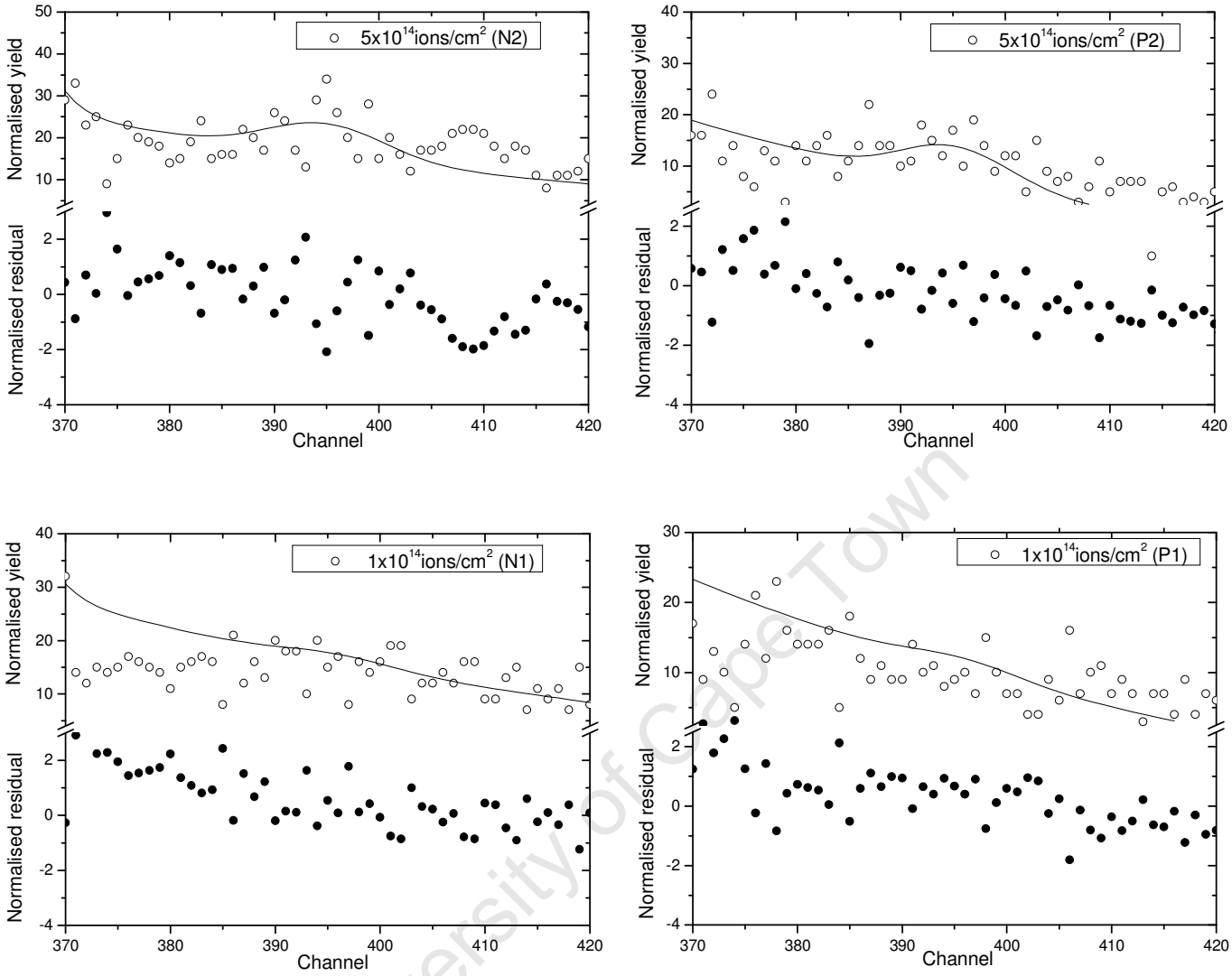

Figure 6.3: (a)-(d) Krypton peak on an expanded scale for unpolished samples. (e)-(h) Krypton peak on an expanded scale for unpolished samples. The residuals for both samples are also shown on each graph at the bottom (continued from previous page).

Samples	Fluence ions/cm^2	Calculated range (Å)	Krypton range (Å)	Krypton straggling (Å)
Unpolished				
N4	5x10^{15}	673	570 ± 10	274 ± 6
N3	1x10^{15}	693	580 ± 20	262 ± 15
N2	5x10^{14}	695	510 ± 30	234 ± 21
N1	1x10^{14}	698	450 ± 50	213 ± 34
polished				
P4	5x10^{15}	673	540 ± 10	234 ± 4
P3	1x10^{15}	693	505 ± 15	226 ± 9
P2	5x10^{14}	695	475 ± 25	221 ± 13
P1	1x10^{14}	698	410 ± 40	212 ± 26

Table 6.1: Krypton projected range and associated straggling for unpolished and polished samples. The calculated range includes correction for sputtering of the surface.

6.2 Oxygen profiling

The results presented in Fig. 6.4 illustrate the backscattering spectra using elastic resonance for oxygen detection. The spectra for both unpolished (Fig. 6.4(a)-(e)) and polished (Fig. 6.4(f)-(j)) samples have been simulated using Gaussian and multilayer modelling at the oxygen resonance energy of 3.045 MeV. The analysis method used is shown in Appendix D(a) for unpolished and Appendix D(b) for polished samples with higher dose implantation. The scattering cross section data for He on oxygen, are those calculated by Gurbich [6.3] with a scattering angle of 165°, corresponding to the setup for the detector. The most noticeable feature in these results is the oxygen resonance peak arising from scattering off near surface oxygen.

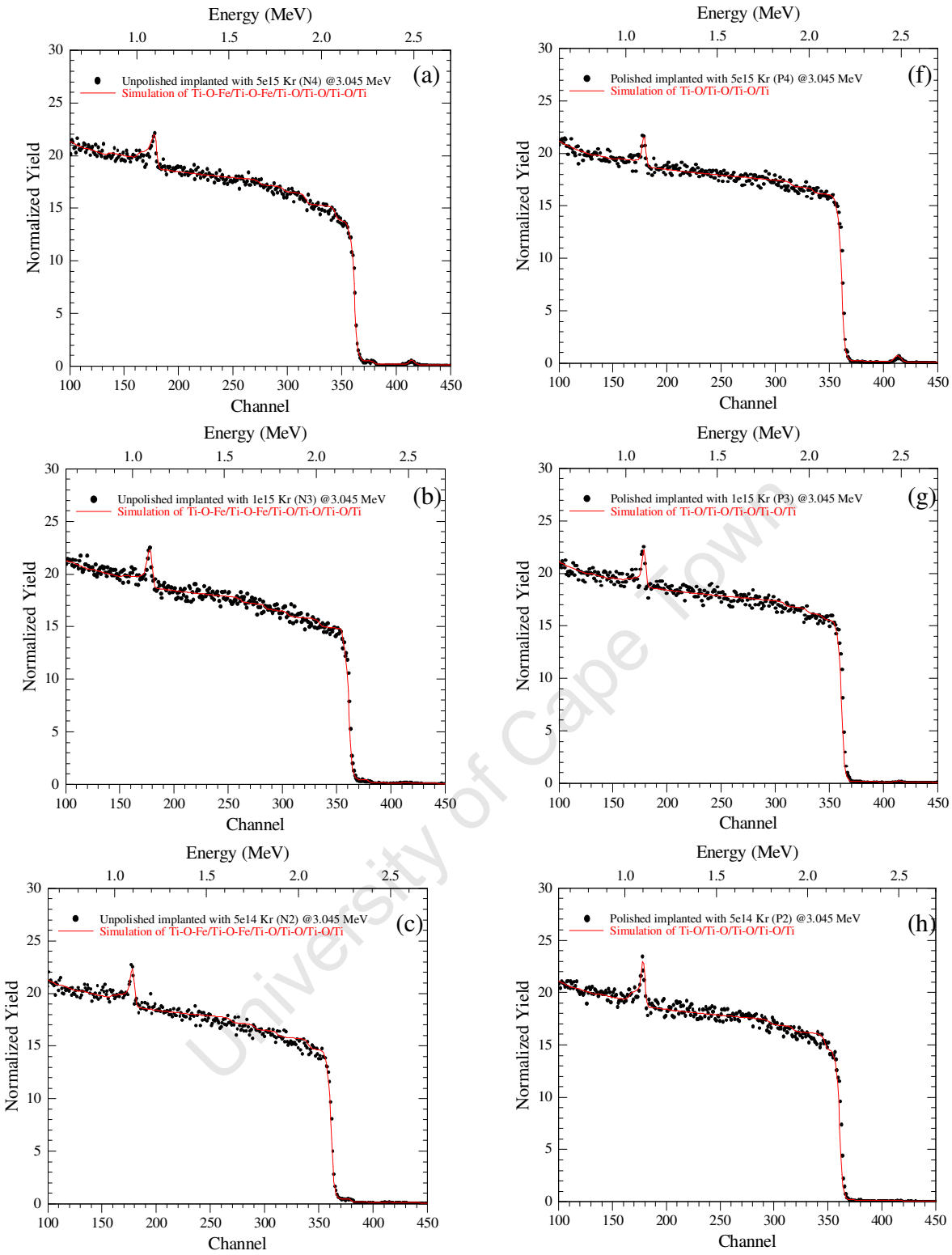

Figure 6.4: (a)-(e) RBS and resonance spectra for unpolished samples. (f)-(j) RBS and resonance spectra for polished samples (continued overleaf).

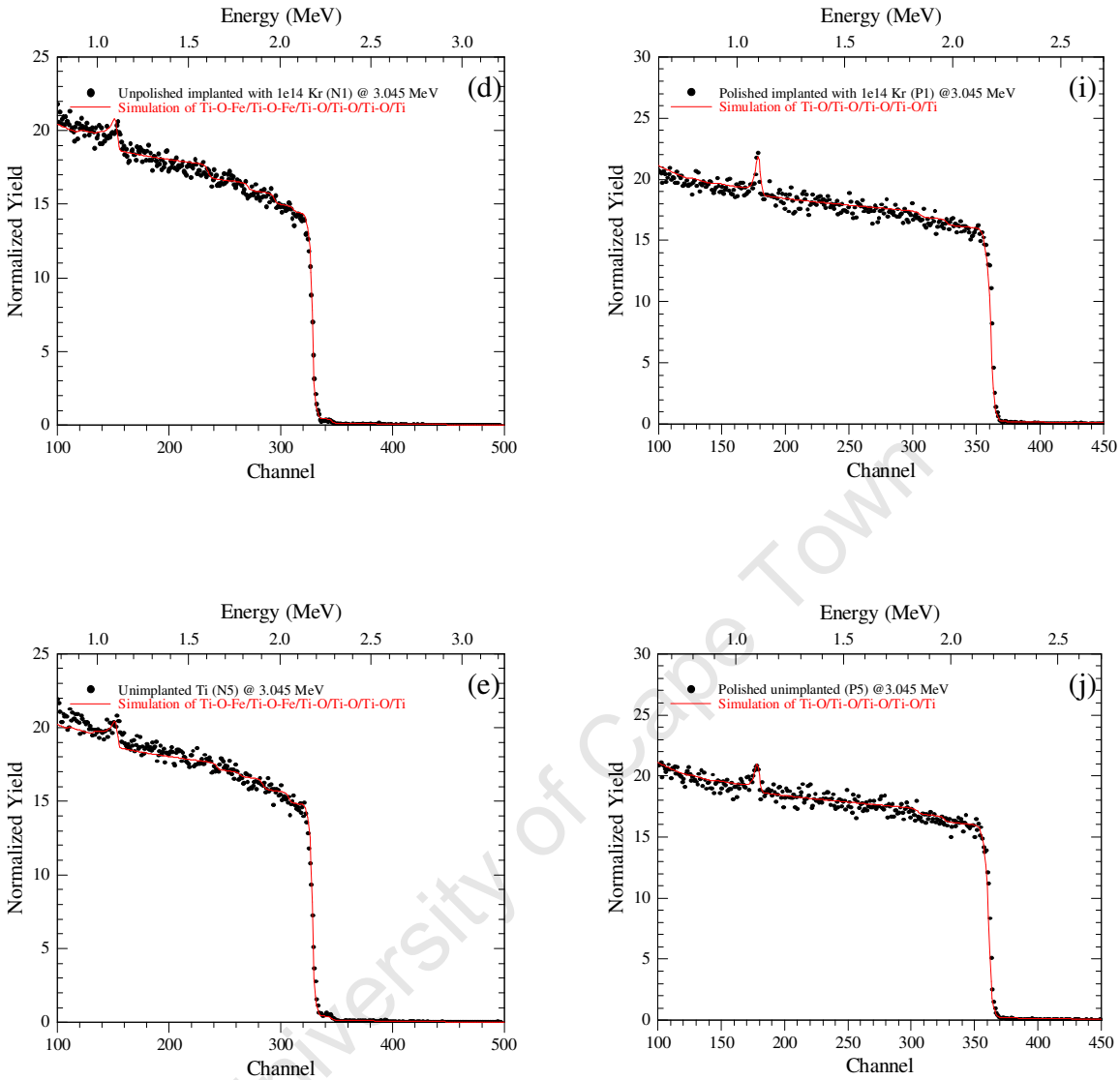

Figure 6.4: (a)-(e) RBS and resonance spectra for unpolished samples. (f)-(j) RBS and resonance spectra for polished samples (continued from previous page).

Scanning the projectile energy to higher energies allowed a profiling of the oxygen. Results are shown in Fig. 6.5, for the as-received and polished samples implanted with $5x10^{15}$ Kr^{+}/cm^{2}. It can be seen that the oxygen peak remains clearly visible in the data for the unpolished sample for incident beam energies

220 keV above resonance, indicating a deep distribution of oxygen. In contrast, in the polished sample the oxygen resonance peak ceases to be present for incident beam energies less than 100 keV above resonance, indicating that oxygen is present only at the surface.

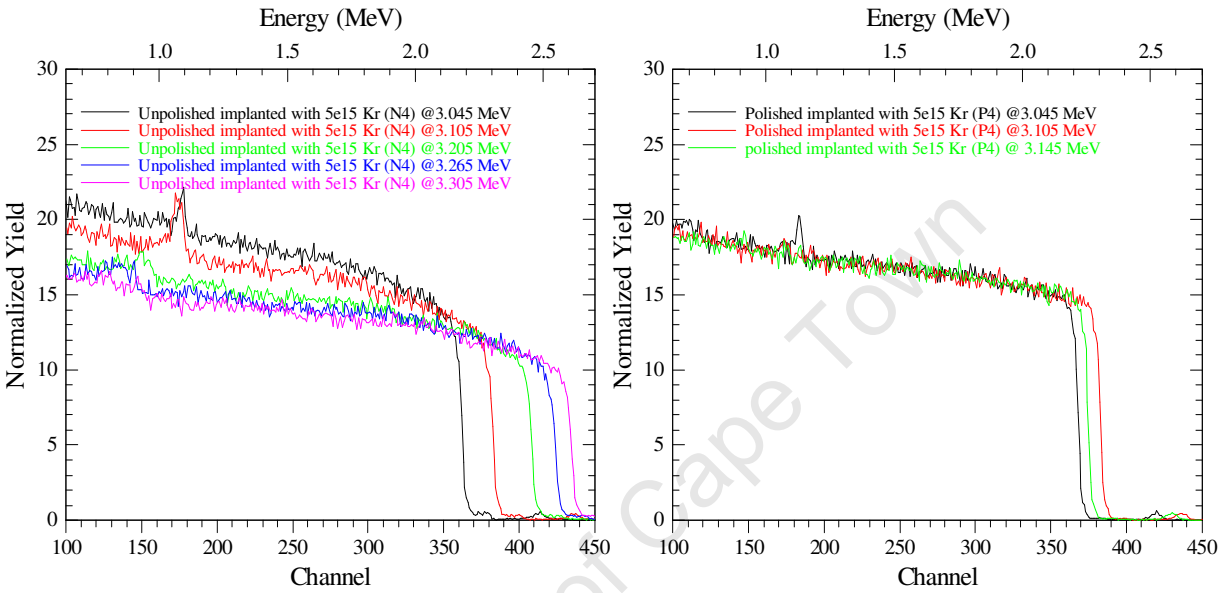

Figure 6.5: The effect of the projectile energy increase on the oxygen resonance peak. (a) Deep oxygen distribution and straggling effect leading to a broadening of the resonance peak for the as-received sample implanted with 5x10^{15} Kr^{+}/cm^{2}. (b) Shallow oxygen distribution for the polished sample implanted with 5x10^{15} Kr^{+}/cm^{2}.

Fig. 6.6 shows the calculated oxygen profile for unpolished and polished samples implanted with the same doses to illustrate the effect of polishing on the oxygen profile. As-received samples have a thick oxygen rich layer with a concentration gradient, and a half width of about 500 nm. This gradient indicates that this oxygen rich layer is not an oxide. The oxygen incorporated near the surface could be a source of micro-residual stress as discussed later. The polishing process has removed the oxygen rich layer, leaving a thin sub-stoichiometric

surface oxide layer of less than 30 nm thickness, corresponding to the resolution limit of the analysis.

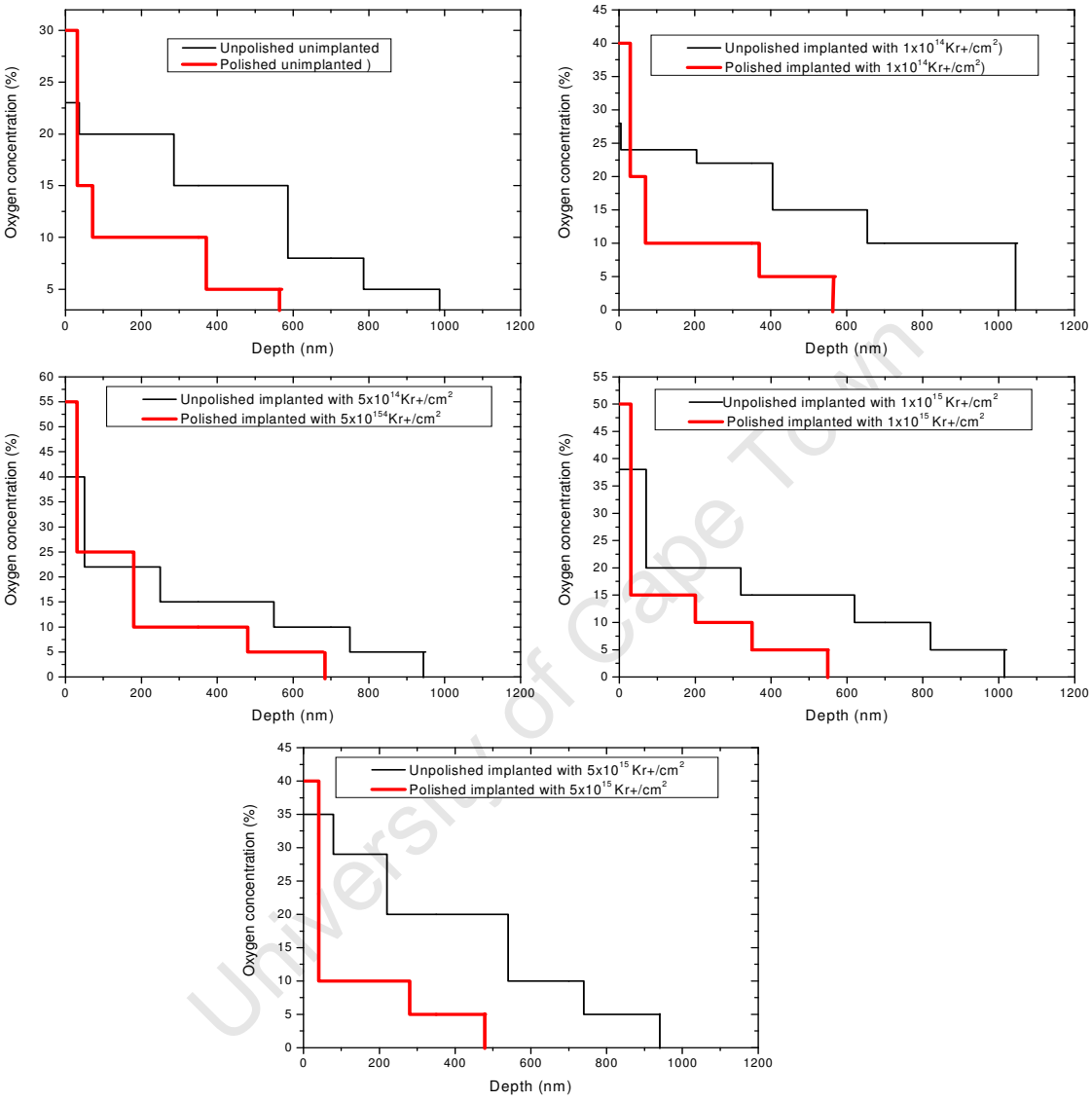

Figure 6.6: Oxygen depth profile for unpolished and polished samples.

6.3 Stress determination

In the following, the results for stress determination from two different analysis methods are presented. In the first case, biaxial stress states in the near surface are assumed, and the principal stresses are obtained from $\sin^2\psi$ plots. In the second, the whole fundamental equation of stress is taken into account for the determination of the depth of the triaxial stress tensor, as discussed in 5.3.5. In addition, a method of analysis to determine the projected strain as a function of penetration depth is presented. The analysis here focuses only on two reflections, *i.e.* the (101) and (100) lattice planes. The reason the (002) and (105) reflections were not considered in this analysis is the lack of sufficient statistics for the peak position determination, mainly at high ψ-tilts where very low scattered intensities are exhibited.

6.3.1 $\sin^2\psi$ curves

This approach uses Eq. (5.30) which relates the strain to stress, and Eq. (5.31), which gives the stress σ_ϕ in any direction defined by ϕ and ψ. This analysis serves as rough guide, in terms of stress magnitudes and length scales in the correct order of magnitude. As a first approximation, the X-ray elastic constants (XEC) were approximated by the macroscopic Lamé elastic constants, in which case $\frac{1}{2}s_2$ is replaced by $\frac{1+\nu}{E}$, and s_1 by $-\frac{\nu}{E}$. In this particular case the values of 120 GPa for Young's modulus E and 0.36 for Poison's ratio were used [6.4]. As seen in Table 6.2, this will lead to a small overestimate of 6 to 8 % in σ_ϕ, compared to using the accurate XEC. This is small compared to other sources of error. In this analysis, the unstressed lattice spacing d_0 for each reflection peak was obtained from the powder diffraction pattern in the ICDD database [6.5].

Table 6.2: X-ray elastic constants calculated according to the Kröner model [6.6, 6.7] for the two sets of lattice planes studied, and the corresponding macroscopic elastic constants.

Elastic constants	(100)	(101)	macroscopic
$\frac{1}{2}s_2$ (GPa^{-1})	0.01203	0.01232	0.01133
s_1 (GPa^{-1})	- 0.00297	- 0.00303	-0.00300

a) unpolished samples

The results that are presented below are for the (101) reflection. One ϕ rotation for unimplanted and implanted samples is shown in the plots in Figure 6.1. Similar plots for different azimuth angles can be found in Appendix E.

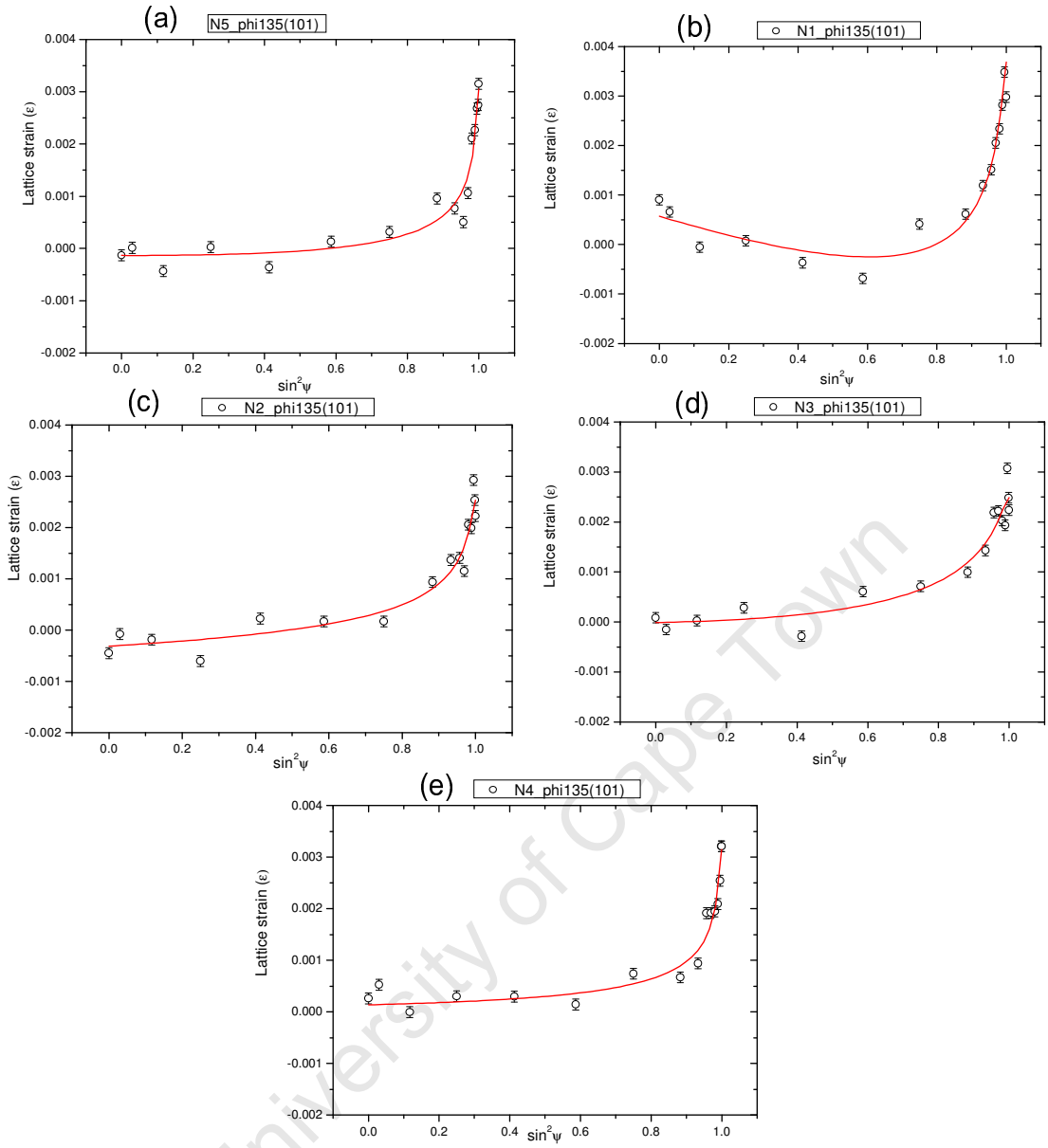

Figure 6.1: $\sin^2\psi$ *plots for the (101) reflection (*ϕ*=135°) in unpolished samples: (a) as-received and unimplanted sample, (b)-(e) samples implanted at fluences of 1x10¹⁴Kr⁺/cm², 5x10¹⁴Kr⁺/cm², 1x10¹⁵Kr⁺/cm², and 5x10¹⁵Kr⁺/cm² respectively.*

All the $\sin^2\psi$ plots for implanted samples have the same form as for the unimplanted sample, *i.e.* a strong curvature at $\sin^2\psi > 0.8$, indicating a stress gradient between the very near surface region and the deeper region

corresponding to the penetration of X-rays. There are therefore two distinct regions in the $\sin^2\psi$ plots which can be represented by a weighted superposition of two linear dependences, which take into account the absorption coefficient factor governing the depth of X-ray penetration. Generally the deeper region, corresponding to low ψ angles, exhibits a low tensile stress, and the near surface region, at high ψ, shows a strong tensile stress.

b) polished samples

In Fig. 6.2 the $\sin^2\psi$ plots show the effect of polishing and implantation compared to unpolished samples. The (101) reflection results for $\phi = 135°$ are shown. Despite a high scattering, there is indeed a difference between the unpolished and the polished samples. The form of the $\sin^2\psi$ plots for the 2 types of samples is quite different. While the gradient at high ψ tilt is positive in the unpolished samples, it is negative in the polished samples. The polishing process, therefore, not only removes the region of strong tensile stress, but also introduces a stress state with opposite sign.

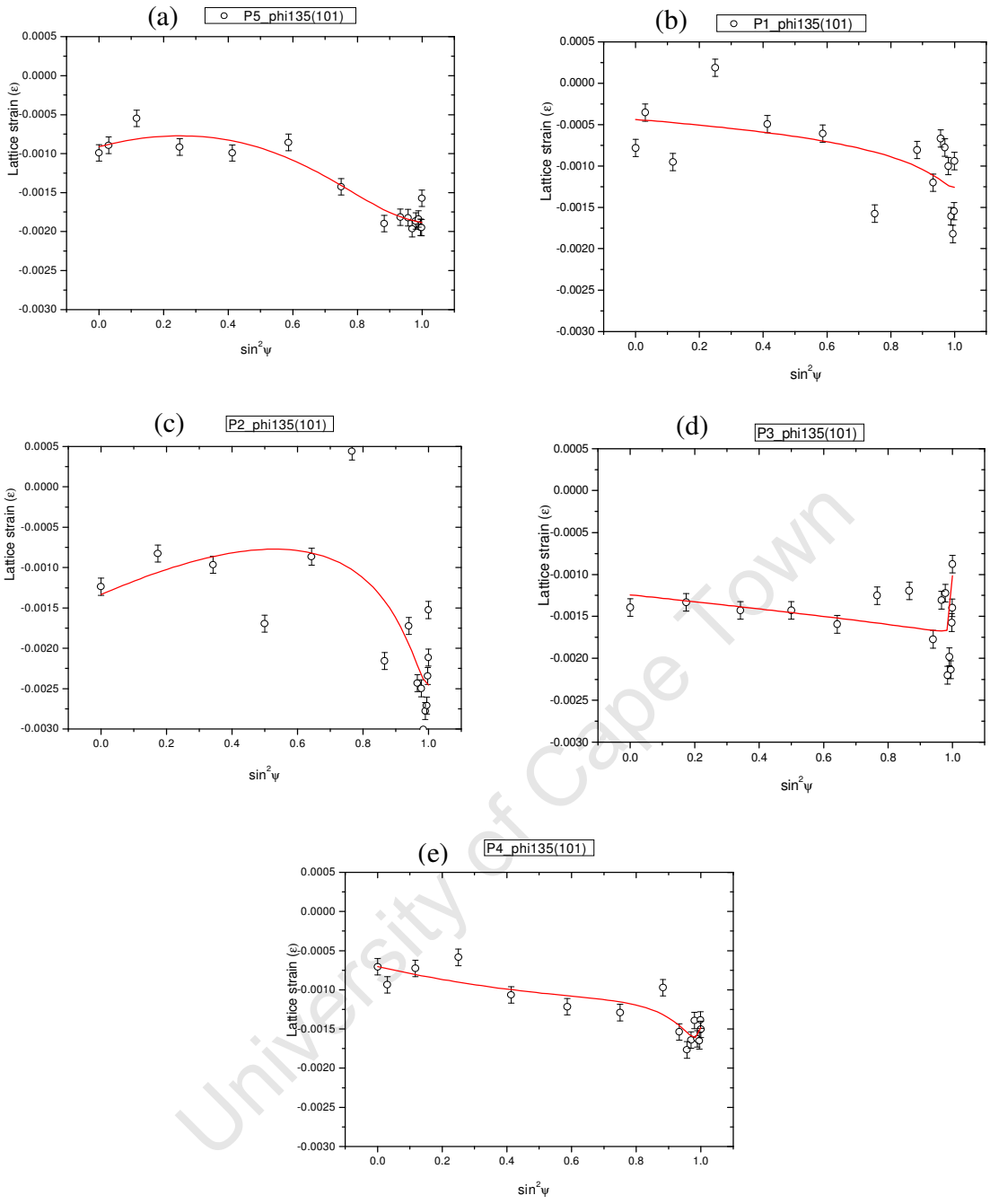

Figure 6.2: $\sin^2\psi$ *plots for the (101) reflection (*ϕ*=135°) in polished samples: (a) unimplanted sample, (b)-(e) samples implanted at fluences of* $1x10^{14}Kr^+/cm^2$, $5x10^{14}Kr^+/cm^2$, $1x10^{15}Kr^+/cm^2$, *and* $5x10^{15}Kr^+/cm^2$ *respectively.*

6.3.2 Depth analysis of $\sin^2\psi$ curves

In the following a 2-zone model [6.8] was used for the estimation of the stress, since the $\sin^2\psi$ curves exhibit a gradient near the surface. The first zone is referred to as the near surface region, and the second as the bulk region. It should be noted, however, that in this case bulk refers to the region up to only the maximum penetration depth of the X-rays. A sketch of the model is shown in Fig. 6.3 below. The $\sin^2\psi$ curves are then assumed to be a superposition of two linear curves weighted with the absorption factor for X-rays.

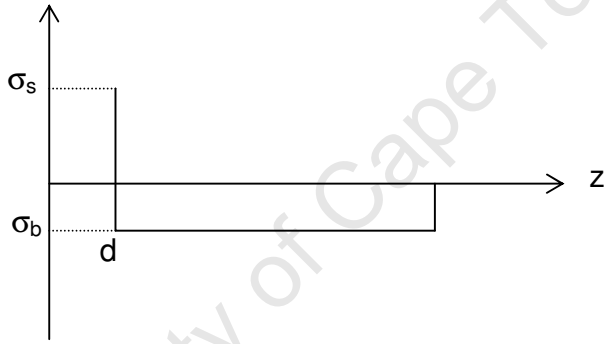

Figure 6.3: The 2-zone model of the stress distribution: σ_s is the near surface stress, and σ_b is the bulk stress.

The near surface and the bulk stresses are both assumed to result in a linear dependence of strain on $\sin^2\psi$, as described in Eq. (5.32). Combining these in a weighted average, yields for the measured strain,

$$\varepsilon_{\phi\psi} = \left(1 - e^{-\frac{d}{\tau\cos\psi}}\right)\left(a_s + b_s \sin^2\psi\right) + e^{-\frac{d}{\tau\cos\psi}}\left(a_b + b_b \sin^2\psi\right), \qquad (6.1)$$

where τ is the penetration of X-rays as given in Eq. (5.33), a_s and b_s, and a_b and b_s, are the intercept and the slope of the near surface strain and the bulk

strain, respectively. Of interest are the limiting values of the stress at the surface and deep in the bulk, corresponding to a depth around 1 μm near the maximum penetration of X-rays. d is a fitting parameter with limited physical significance because a sudden change between the two regions is unphysical. A non-linear fit to Eq. (6.1) is then used to obtain estimates of these parameters, which can then be used to determine σ_ϕ independently in both regions.

a) unpolished samples

The results of σ_ϕ versus ϕ for the (101) reflection are presented in the form of polar plots for the near surface and bulk regions in Fig. 6.4, and Fig. 6.5 respectively. The results from the (100) reflection are shown in Appendix F.

From Fig. 6.4, it can easily be seen that the surface stress decreases with the implantation. Initially, the near surface stress is highly tensile and anisotropic, whereas at the highest doses a roughly isotropic low tensile stress is observed. In contrast, for the bulk stress there is no clear trend. Overall the stress is slightly compressive and isotropic, with similar magnitudes in the sample implanted at the highest dose and in the unimplanted sample. An exception is the sample implanted at the lowest dose, in which a strongly compressive stress is observed. This is also seen in the $\sin^2\psi$ plots (Fig. 6.1) where there is definite negative slope at low ψ.

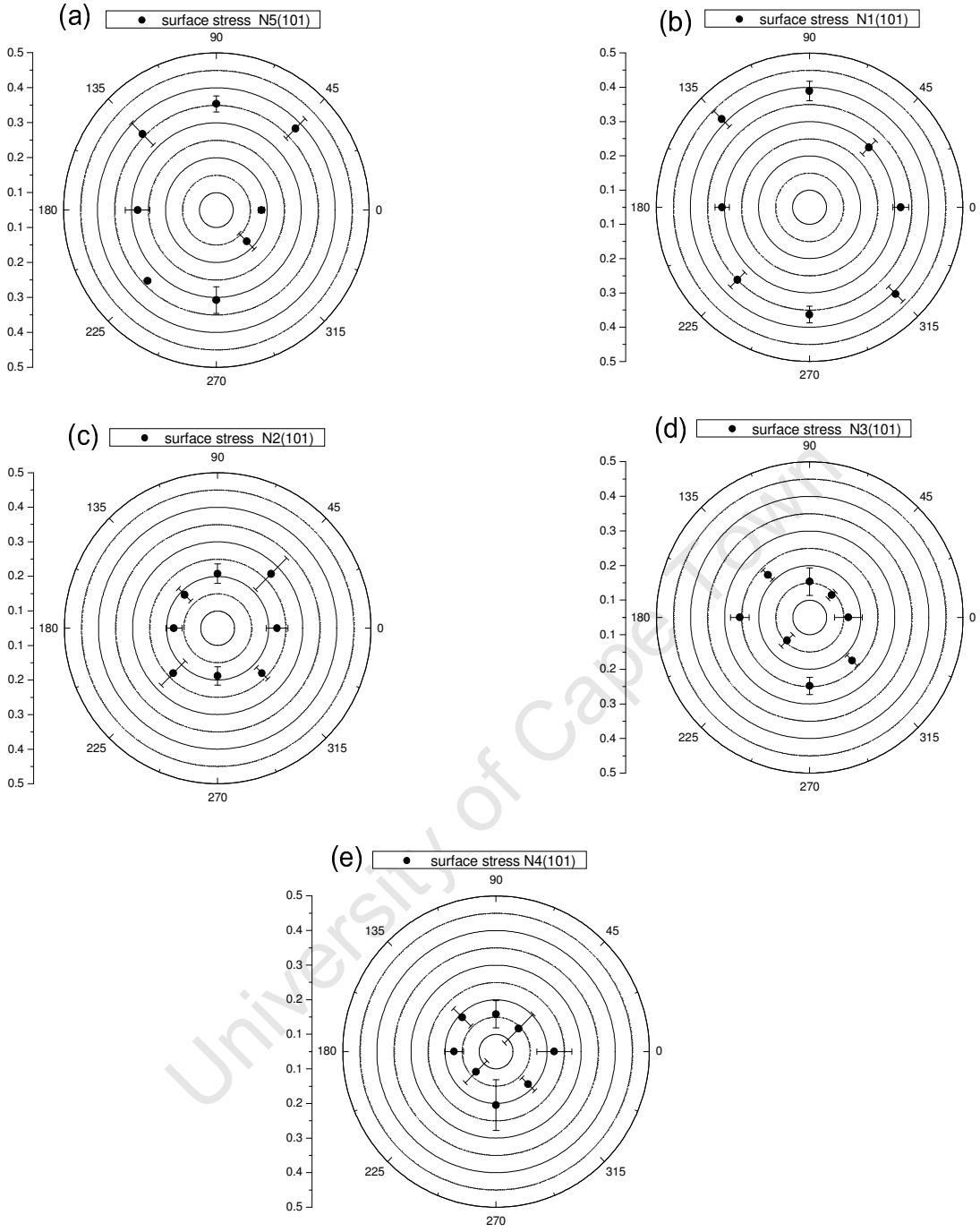

Figure 6.4: Polar plot representation of stress σ_ϕ versus ϕ-rotation for (101) reflection for the near surface region of unpolished samples: (a) unimplanted sample,(b)-(e) samples implanted at fluences of $1x10^{14}Kr^+/cm^2$, $5x10^{14}Kr^+/cm^2$, $1x10^{15}Kr^+/cm^2$, and $5x10^{15}Kr^+/cm^2$ respectively.

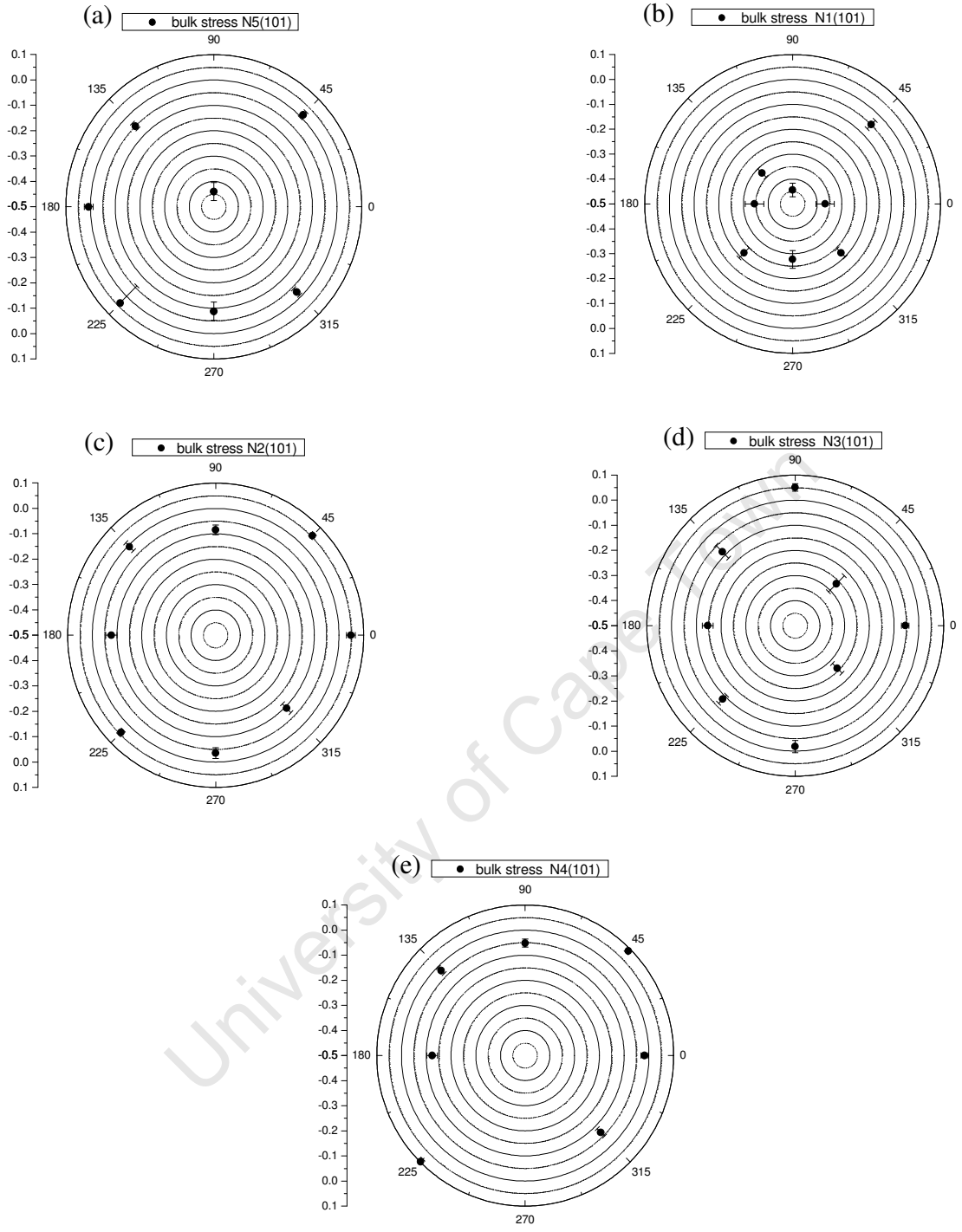

Figure 6.5: Polar plot representation of stress σ_ϕ versus ϕ-rotation for (101) reflection for the bulk region of unpolished samples: (a) unimplanted sample, (b)-(e) samples implanted at fluences of $1x10^{14}Kr^+/cm^2$, $5x10^{14}Kr^+/cm^2$, $1x10^{15}Kr^+/cm^2$, and $5x10^{15}Kr^+/cm^2$ respectively.

b) polished samples

The evolution of the stress σ_ϕ versus ϕ in the near surface and bulk regions with implantation is shown in Figs. 6.6 and 6.7 for the (101) reflection. As can be seen in the polar plots, the stress state is affected by the polishing process. The high tensile stresses observed in the unpolished samples near the surface are removed by the polishing process, and are replaced with a low compressive stress. This stress remains virtually unchanged on implantation. In the bulk, a compressive stress, which is generally isotropic, is seen. This appears to be reduced on implantation, until the highest dose, when it increases to the level of that in the unimplanted sample.

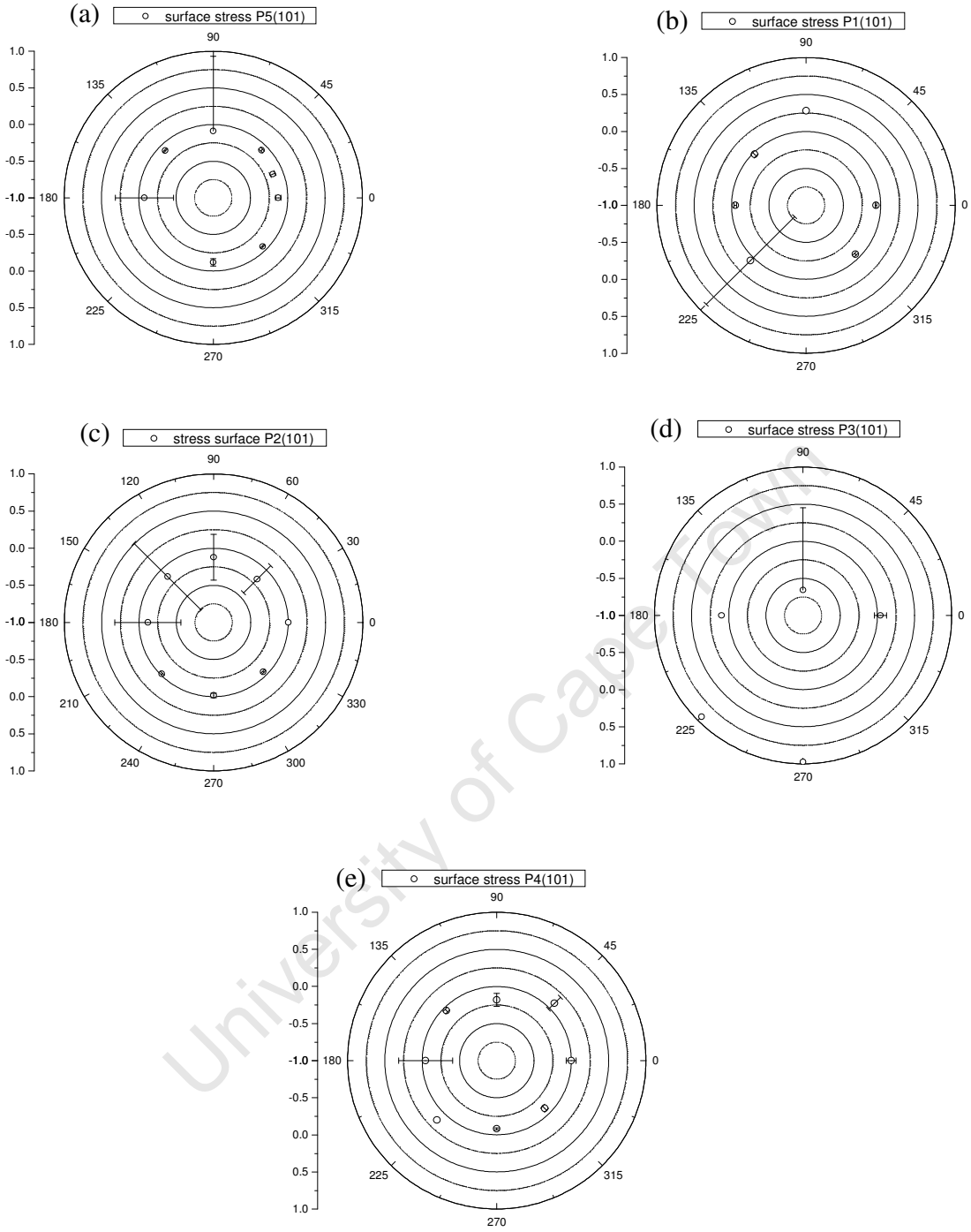

Figure 6.6: Polar plot representation of stress σ_ϕ versus ϕ-rotation for (101) reflection for the surface region: (a) polished sample, (b)-(e) polished samples implanted at fluences of $1x10^{14}Kr^+/cm^2$, $5x10^{14}Kr^+/cm^2$, $1x10^{15}Kr^+/cm^2$, and $5x10^{15}Kr^+/cm^2$ respectively.

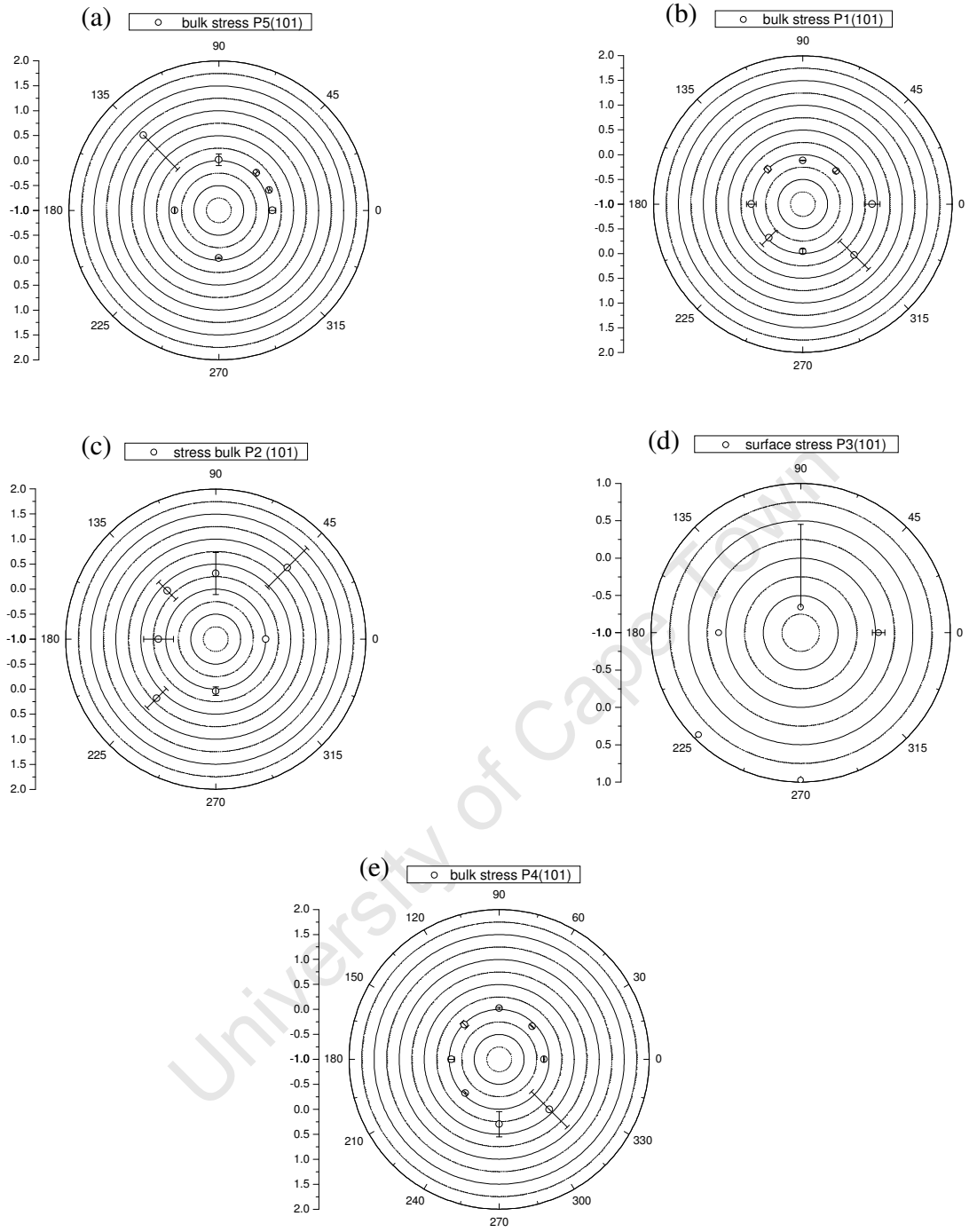

Figure 6.7: Polar plot representation of stress σ_ϕ versus ϕ-rotation for (101) reflection for the bulk region: (a) polished sample, (b)-(e) polished samples implanted at fluences of 1x10^{14}Kr$^+$/cm^2, 5x10^{14}Kr$^+$/cm^2, 1x10^{15}Kr$^+$/cm^2, and 5x10^{15}Kr$^+$/cm^2 respectively.

6.3.3 Principal stresses and asymmetries

The normal stresses σ_{11}, σ_{22}, and the shear component σ_{12} in Eq. (5.31) can be obtained by a non-linear fit to σ_ϕ as a function of ϕ. However, because the orientation of the sample is not known, the components of the stress tensors cannot be compared directly for different samples. It is therefore convenient to represent the stress by its principal stresses (Fig. 6.8), which are given by a principal axis transformation [6.9],

$$\sigma_1 = \left(\frac{\sigma_{11}+\sigma_{22}}{2}\right) + \sqrt{\left(\frac{\sigma_{11}-\sigma_{22}}{2}\right) + \sigma_{12}^2}, \qquad (6.2)$$

$$\sigma_2 = \left(\frac{\sigma_{11}+\sigma_{22}}{2}\right) - \sqrt{\left(\frac{\sigma_{11}-\sigma_{22}}{2}\right) + \sigma_{12}^2}. \qquad (6.3)$$

As shown in Fig. 6.8, σ_1, and σ_2 are the principal axes of the stress ellipse, and unlike σ_{11},and σ_{22} are independent of the sample orientation.

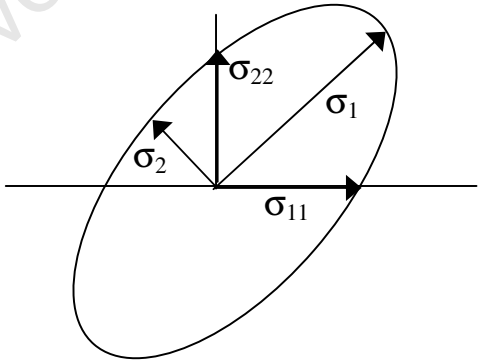

Fig. 6.8: Diagram showing the normal stresses σ_{11} and σ_{22}, and the principal stresses σ_1 and σ_2.

In order to investigate the effect of implantation on stress, the principal stresses, σ_1, σ_2, the normal stress $\sigma_1 + \sigma_2$, and the stress asymmetry $\sigma_1 - \sigma_2$ are plotted as a function of the fluence, for the (101) reflection. The values of principal stresses for (100) reflection are tabulated.

a) unpolished samples

In the surface region, Fig. 6.9 (a)-(c), the graph shows very interesting features of the stress change as a function of the fluence: an additional stress at the early stage of the implantation, and a stress reduction as the implantation dose increases. For instance, for σ_1 the unimplanted stress value is 0.37 GPa, at the following fluence it becomes 0.40 GPa, and 0.19 GPa for the highest fluence. This feature is the same for σ_2, and hence for $\sigma_1 + \sigma_2$. In the latter case, there is a reduction of 20% at the highest fluence, *i.e.* 5x10^{15} Kr$^+$/cm^2. For the asymmetry of $\sigma_1 - \sigma_2$, there is a general reduction for all fluences, but the reduction rate is higher for lower fluences than higher fluences.

A closer look at the bulk stress values, in Fig 6.9(b)-(d), leads to the following observations: there is a change in stress from 0.06 to -0.17 GPa for σ_1, and from -0.16 to -0.33 for σ_2 for the lowest fluence. From a fluence of 1x10^{15} Kr$^+$/cm^2, the stress starts to increase and becomes more tensile than the initial stress value of the unimplanted sample, 0.1GPa for σ_1, and -0.07 for σ_2.

For the (100) reflection surface stress shown in Table 6.3(a), similar features are observed as in the case of the (101) reflection. There is a stress reduction with increasing fluence but the reduction rate is slower than that observed in the (101) lattice planes.

For the (100) reflection bulk stress, which are tabulated in Table 6.3(b), there is generally an increase in the compressive stress and asymmetry with implantation

dose below 1x10^{15} Kr^{+}/cm^{2}. Both the stress magnitude and asymmetry relax to below their initial values at the highest fluence.

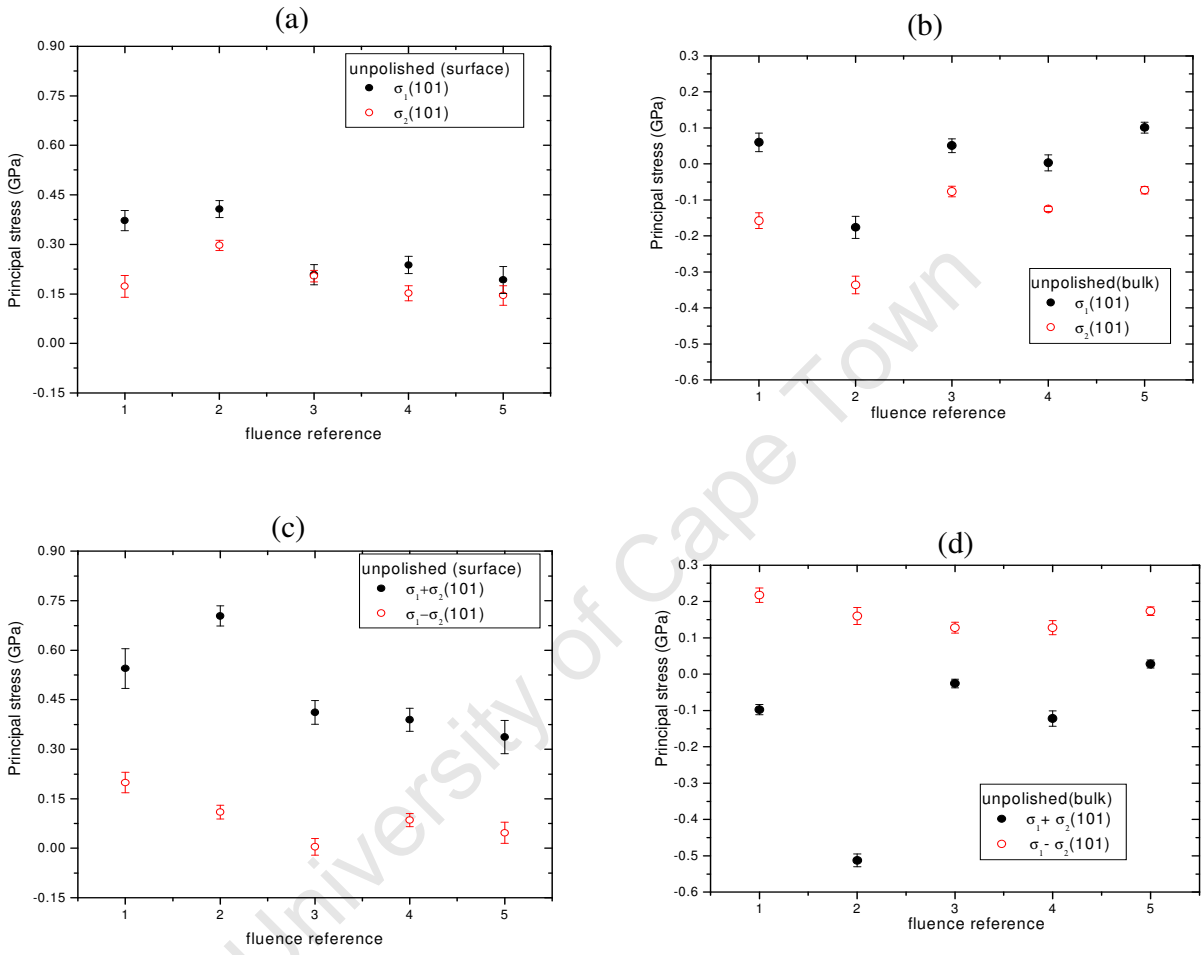

Figure 6.9: Principal stress versus fluence for unpolished samples: (a) and (c) surface stress. (b) and (d) bulk stress.

Table 6.3: Principal stress for the (100) reflection of unpolished samples

(a) surface

Principal stress (GPa)	Unimplanted (1)	1x10^{14}/cm^2 (2)	5x10^{14}/cm^2 (3)	1x10^{15}/cm^2 (4)	5x10^{15}/cm^2 (5)
$\sigma_1 \pm \Delta\sigma_1$	0.19±0.02	0.20±0.03	0.18±0.02	0.12±0.02	0.16±0.05
$\sigma_2 \pm \Delta\sigma_2$	0.04±0.02	0.13±0.03	0.09±0.01	0.09±0.01	0.07±0.02
$(\sigma_1+\sigma_2) \pm \Delta(\sigma_1+\sigma_2)$	0.23±0.03	0.33±0.04	0.27±0.03	0.22±0.02	0.22±0.02
$(\sigma_1-\sigma_2) \pm \Delta(\sigma_1-\sigma_2)$	0.14±0.02	0.06±0.02	0.08±0.02	0.03±0.01	0.09±0.01

(b) bulk

Principal stress (GPa)	Unimplanted (1)	1x10^{14}/cm^2 (2)	5x10^{14}/cm^2 (3)	1x10^{15}/cm^2 (4)	5x10^{15}/cm^2 (5)
$\sigma_1 \pm \Delta\sigma_1$	-0.03±0.02	0.02±0.01	0.04±0.02	-0.07±0.02	0.01±0.01
$\sigma_2 \pm \Delta\sigma_2$	-0.12±0.01	-0.16±0.01	-0.19±0.02	-0.13±0.01	-0.08±0.01
$(\sigma_1+\sigma_2) \pm \Delta(\sigma_1+\sigma_2)$	-0.15±0.02	-0.12±0.02	-0.15±0.03	-0.21±0.02	-0.07±0.01
$(\sigma_1-\sigma_2) \pm \Delta(\sigma_1-\sigma_2)$	0.09±0.01	0.17±0.01	0.23±0.01	0.06±0.02	0.08±0.01

b) polished samples

As for the unpolished samples, the principal stresses have been calculated using Equations (6.2) and (6.3) and graphs of principal stress versus fluence have been plotted to investigate the effect of implantation on the stress for polished samples. Fig. 6.10 shows the plots for (101) reflection. The results for the (100) reflection are tabulated in Table 6.4.

In the near surface, Fig. 6.10 (a)-(c), the low fluence introduces a slight additional stress and an overall reduction occurs as the fluence increases. This trend is the same for $\sigma_1 + \sigma_2$ as well as $\sigma_1 - \sigma_2$.

In the bulk, Fig. 6.10 (b)-(d), the graph of σ_1 versus fluence shows that stress becomes less tensile as the fluence increases, whereas for σ_2, there is rather an increase of the stress up to a fluence of 5x10^{14} Kr$^+$/cm^2. This behaviour is reflected in the curve for the asymmetry $\sigma_1 - \sigma_2$, which becomes less negative as the dose is increased.

Table 6.4 gives the stress values for the principal stress versus the implantation dose for (100) reflection. At low fluences there is an increase in both the compressive normal stress and the asymmetry with fluence. However, a further implantation both appear to relax.

In the bulk, the behaviour of σ_1, σ_2, $\sigma_1 + \sigma_2$, and $\sigma_1 - \sigma_2$ are similar. As the fluence increases, a compressive stress is introduced but at higher fluence, *i.e.*, 1x10^{15} Kr$^+$/cm^2, stress compensation is observed. The stress values approach the stress values of the unpolished sample.

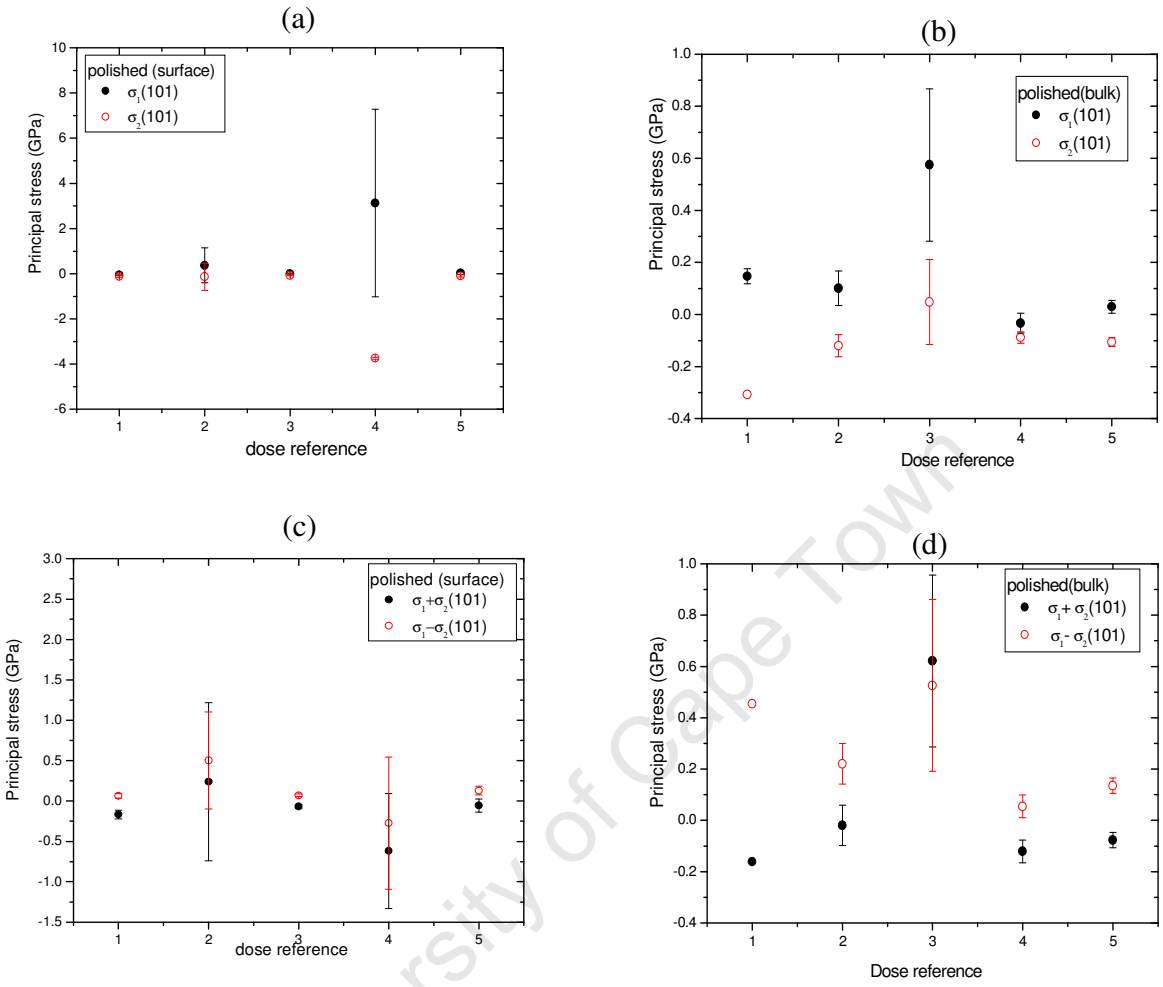

Figure 6.10: Principal stress versus fluence for polished samples: (a) and (c) surface stress. (b) and (d) bulk stress.

Table 6.4: Principal stress values for the (100) reflection of polished samples

(a) surface

Principal stress (GPa)	Unimplanted (1)	1x10^{14}/cm^2 (2)	5x10^{14}/cm^2 (3)	1x10^{15}/cm^2 (4)	5x10^{15}/cm^2 (5)
$\sigma_1 \pm \Delta\sigma_1$	0.03±0.03	-0.01±0.45	0.76±0.40	0.03±0.16	0.16±0.78
$\sigma_2 \pm \Delta\sigma_2$	-0.31±0.30	-0.46±0.34	-0.21±0.32	-0.11±.13	-0.03±0.73
$(\sigma_1+\sigma_2) \pm \Delta(\sigma_1+\sigma_2)$	-0.28±0.20	-0.48±0.46	0.55±0.98	-0.08±0.14	0.13±0.19
$(\sigma_1-\sigma_2) \pm \Delta(\sigma_1-\sigma_2)$	0.24±0.17	0.57±0.35	0.51±0.31	0.20±0.12	1.07±0.56

(b) bulk

Principal stress (GPa)	Unimplanted (1)	1x10^{14}/cm^2 (2)	5x10^{14}/cm^2 (3)	1x10^{15}/cm^2 (4)	5x10^{15}/cm^2 (5)
$\sigma_1 \pm \Delta\sigma_1$	0.05±0.015	-0.04±0.04	-0.15±0.05	-0.04±0.29	-0.02±0.01
$\sigma_2 \pm \Delta\sigma_2$	-0.16±0.01	-0.13±0.01	-0.18±0.04	-0.55±0.23	-0.20±0.01
$(\sigma_1+\sigma_2) \pm \Delta(\sigma_1+\sigma_2)$	-0.11±0.02	-0.17±0.04	-0.32±0.07	-0.58±0.37	-0.22±0.02
$(\sigma_1-\sigma_2) \pm \Delta(\sigma_1-\sigma_2)$	0.21±0.01	0.08±0.03	0.03±0.03	0.50±0.23	0.18±0.01

6.3.4 Uniaxial projected strain

It is recalled that for low index lattice planes, with a low Bragg angle, only the surface layer is probed. As the Bragg angle increases, the sample is probed deeper by the X-rays. Therefore the measurement of different reflections leads to different penetration depths. Moreover, for the same ψ tilt, the strains in different crystallographic directions are probed. To compare the same average penetration depth, we have suggested [6.10] a projected strain representation, whereby the projection of the uniaxial strain $\varepsilon_{\psi\phi}$ on the plane parallel to the sample surface is plotted as a function of the mean penetration depth given by Equation (5.31). The use of the projected strain shown in Fig. 6.11, is appropriate for the reason that $\varepsilon_{\psi\phi}$ is actually a vector, and not a tensor quantity. The projected strain $\varepsilon_{\phi} = \varepsilon_{\psi\phi} \sin\psi$ is the component of $\varepsilon_{\psi\phi}$ in the plane of the sample, and allows the observation of the uniaxial strain in the same direction over the same penetration depth. In the following, plots of the projected strain as a function of penetration depth are shown for unimplanted and implanted samples in (101) and (100) directions for the same azimuthal direction ϕ =135°.

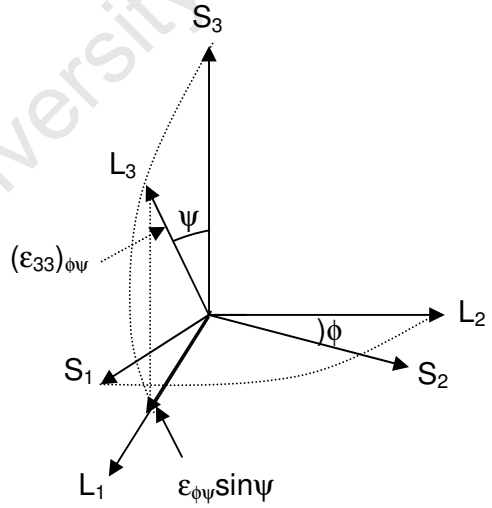

Fig 6.11: The geometry definition of the uniaxial strain projection $\varepsilon_{\phi} = \varepsilon_{\psi\phi} \sin\psi$.

a) unpolished samples

In the plots shown in Fig. 6.10, one can see clearly how the projected strain is affected by both the crystallographic direction and the implantation dose. For all five plots, the common feature is that there is a steep gradient in the region below around 1 μm. In both cases, the projected strain approaches zero at the deepest penetration depth sampled, due to the lack of sensitivity imposed as $\sin\psi$ approaches zero. However, neglecting the last few data points, the projected strain for the (100) reflection is systematically lower than that for the (101) reflection for the unimplanted sample, and a higher slope for the (101) is observed. The effect of implantation is also observable in both cases. The general trend is that as the implantation increases, the slope is reduced for both reflections in the region below 1 μm.

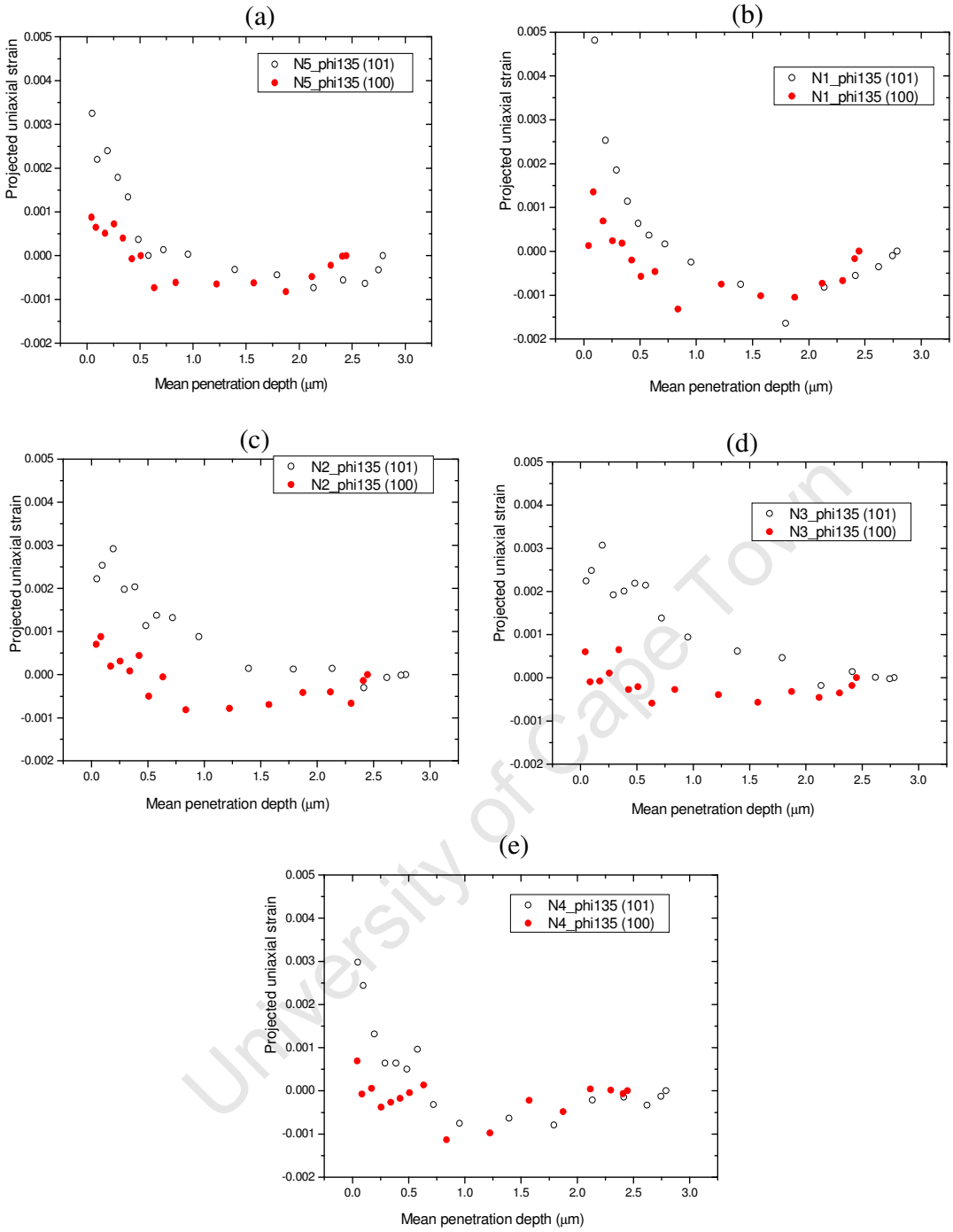

Figure 6.10: Uniaxial projected strain versus mean penetration depth for (101) and (100) reflections, for ϕ=135° in unpolished samples implanted at 1x10^{14}Kr^{+}/cm^{2} (N1), 5x10^{14}Kr^{+}/cm^{2} (N2), 1x10^{15}Kr^{+}/cm^{2} (N3), 5x10^{15}Kr^{+}/cm^{2} (N4).

b) polished samples

The uniaxial projected strain versus mean penetration depth graphs in the polished samples are plotted in Fig. 6.11 to show the effect of both the polishing process and the implantation. For comparison purpose, the graphs for the (101) and (100) reflections for ϕ=135° are presented, as in the case of the unpolished samples. As can be seen, the effect of polishing is manifest if one compares Fig 6.11 to Fig. 6.10. The steep gradient near the surface, which is seen in the unpolished samples, is not present in the polished samples. Instead, over the first 0.75 μm there is an almost constant compressive strain for the (101) direction and a decreasing compressive strain for (100). As the implantation dose is increased the two curves become more similar, with a constant weakly compressive strain in the near surface region.

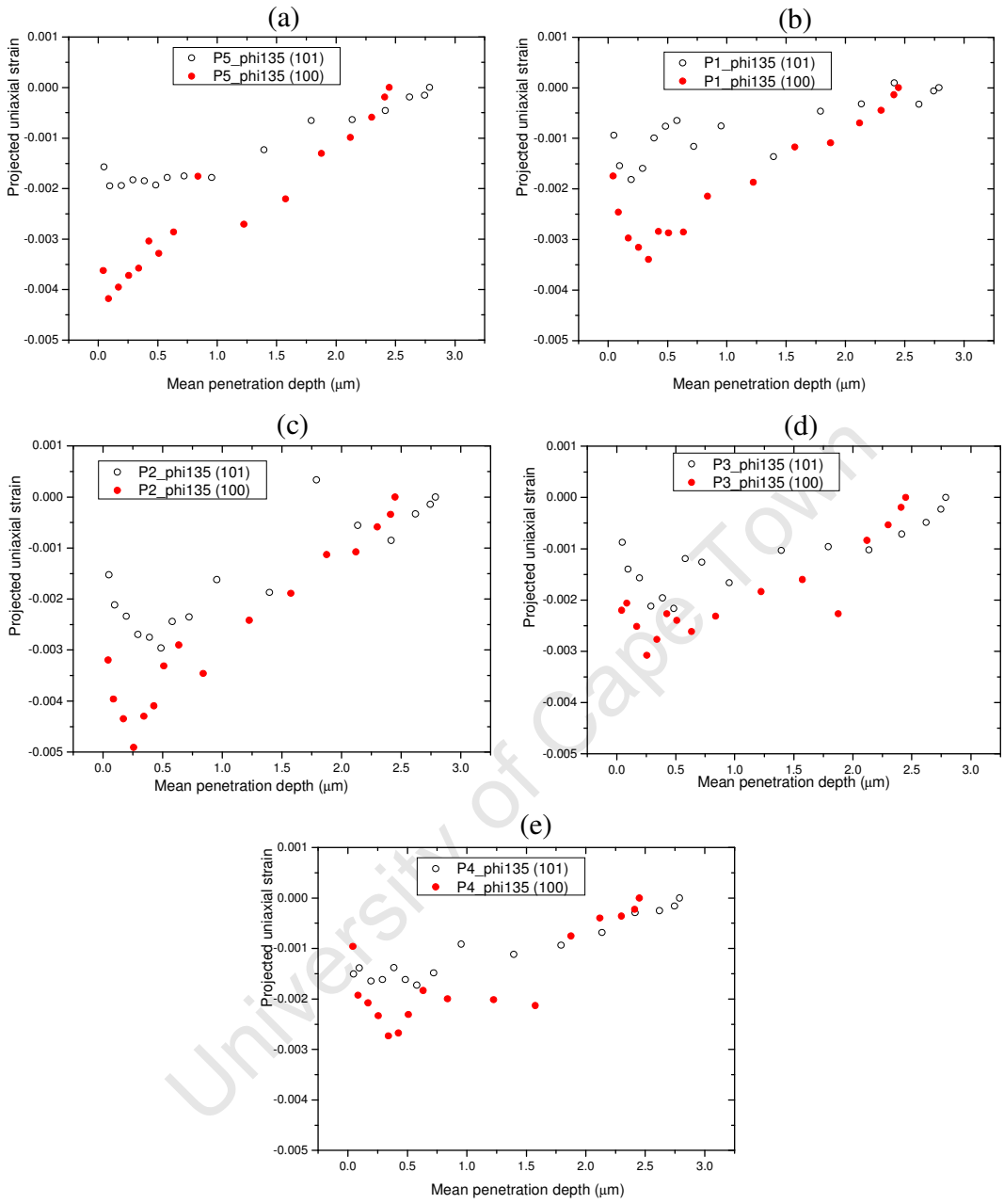

Figure 6.11: Uniaxial projected strain versus mean penetration depth for (101) and (100) reflections, for ϕ=135° in polished samples implanted at $1x10^{14}Kr^{+}/cm^{2}$ (N1), $5x10^{14}Kr^{+}/cm^{2}$ (N2), $1x10^{15}Kr^{+}/cm^{2}$ (N3), $5x10^{15}Kr^{+}/cm^{2}$ (N4).

6.3.5 Stress profile

In the analysis of $\sin^2\psi$ plots, a biaxial stress state is assumed, the information obtained is only partial since the tensor features of the stress profiles are not taken into account. In the following analysis, the depth resolution of the complete stress tensors is determined. From a set of diffraction data, the semi-numerical method as described in section 5.3.2 is used. This analysis takes into account the dependence of the stress with crystallographic orientation. The X-ray elastic constants used are determined according to the Kröner model [6.6, 6.7], and are given in Table 6.2 for the different peaks investigated.

Mathematica software is used for the non linear fit procedure. Input data comprises the experimental values of the strain corresponding to the different ψ tilts and ϕ rotations of the samples during the experiment. It is to be remembered that 16 ψ tilts and 8 ϕ rotations were performed on each sample. Therefore for each sample 128 strain values were obtained. For more accuracy both (100) and (101) reflections have been analysed together to obtain the stress profile. This implies that for each sample 256 independent strain values were used. For all samples the shear components are not considered in this analysis, due to the fact all the coefficients in the expansion were highly correlated, with an absolute correlation coefficient higher than 0.98, and correspondingly large errors, which are not reliable enough to say anything about depth, as seen in Appendix A. Hence, only the normal components will be shown. Furthermore, the discussion of this analysis concentrates on the first micron because of insufficient information and divergence of the power series at large depths.

a) Unpolished samples

A closer look at the normal stresses for the unimplanted and implanted samples (Figs. 6.12 to 6.16) shows a same behaviour for σ_{11} and σ_{22}. The stress profile

sharply decreases with the penetration depth and changes sign at different depths with fluence. The magnitudes of the stress at the near surface are nearly the same for the whole range of implantation but there is a slight decrease as the fluence increases. The slope of the stress depth profile is affected by the implantation. For the stress tensor component σ_{11}, there is a slight decrease in the slope at low fluences but at the highest fluence the slope becomes higher than that of the unimplanted sample. For the stress tensor σ_{22} there is sharp decrease in the slope and subsequent implantation increases the slope, but it remains lower than that of the unimplanted sample. The stress profile of the stress tensor component σ_{33} is nearly zero in the first micron.

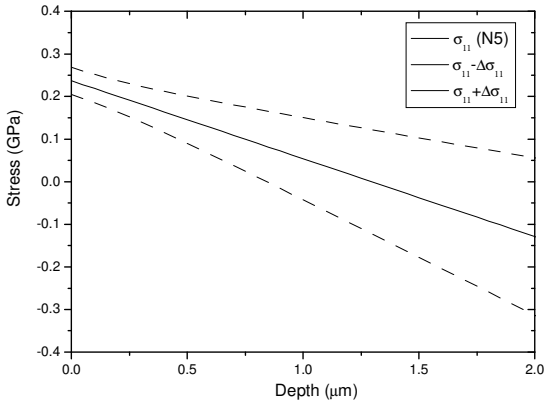

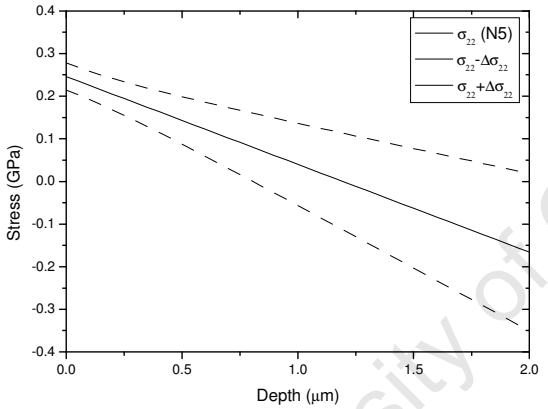

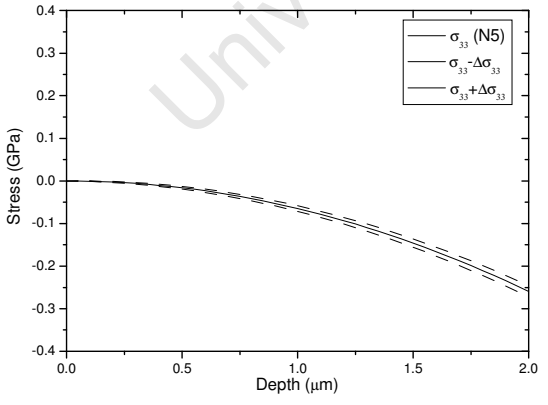

Figure 6.12: Stress depth profile of the normal components for the unimplanted sample.

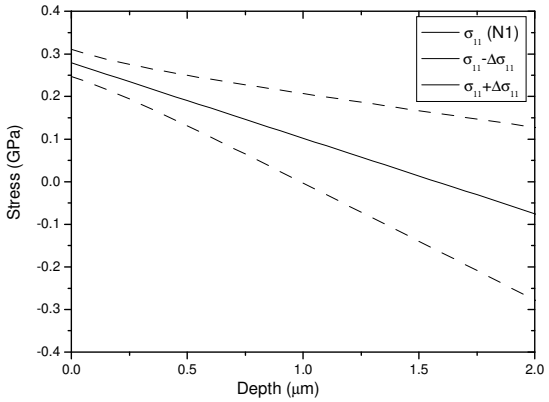

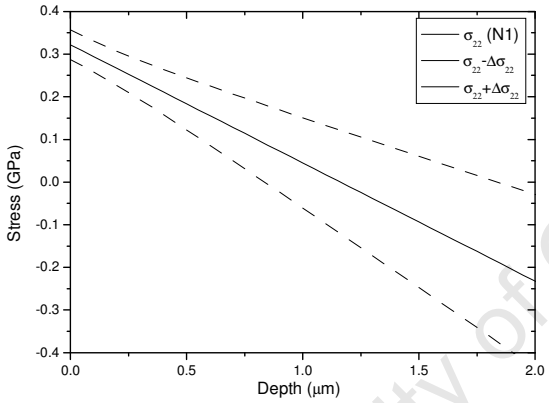

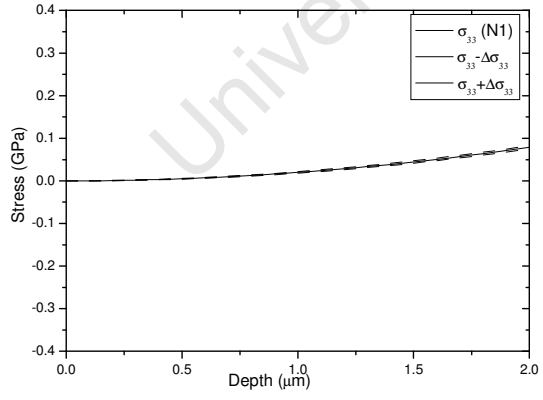

Figure 6.13: Stress depth profile of the normal components of the sample implanted at fluence of 1x10^{14} Kr^{+}/cm^{2}.

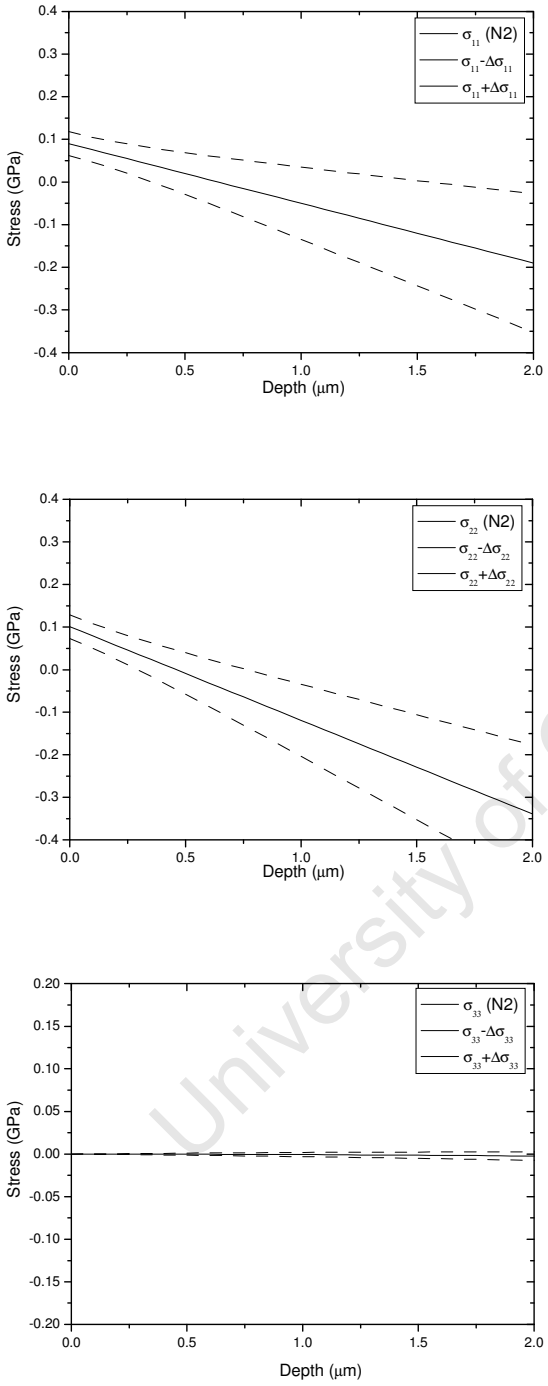

Figure 6.14: Stress depth profile of the normal components of the sample implanted at fluence of 5x10^{14} Kr^{+}/cm^{2}.

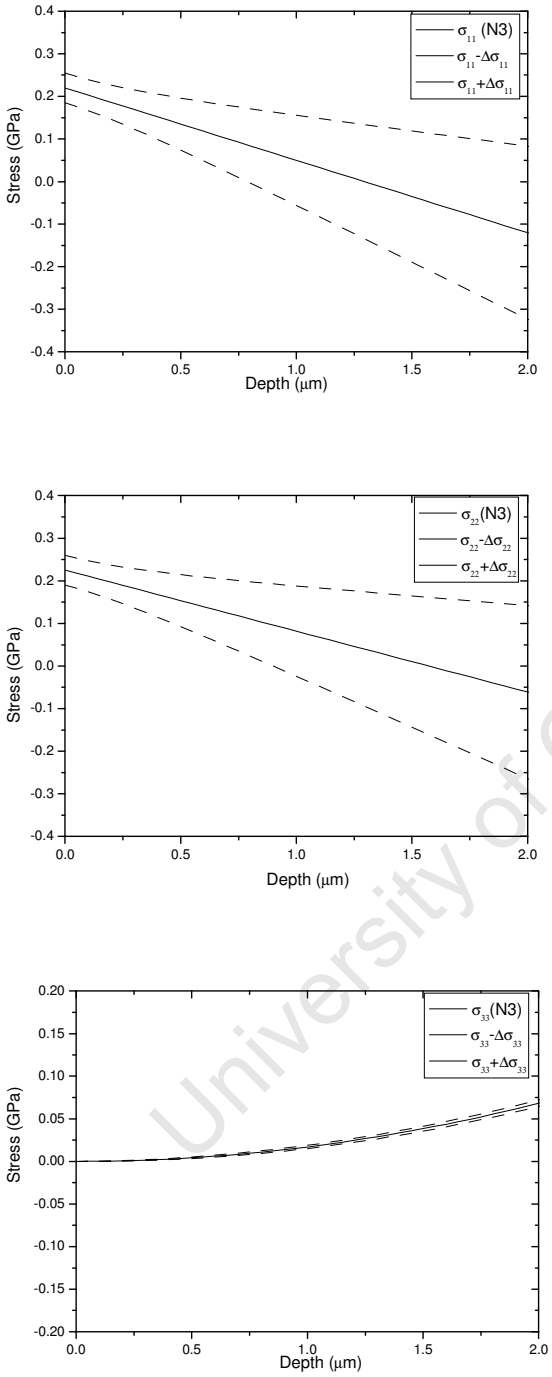

Figure 6.15: Stress depth profile of the normal components of the sample implanted at fluence of 1x10^{15} Kr^{+}/cm^{2}.

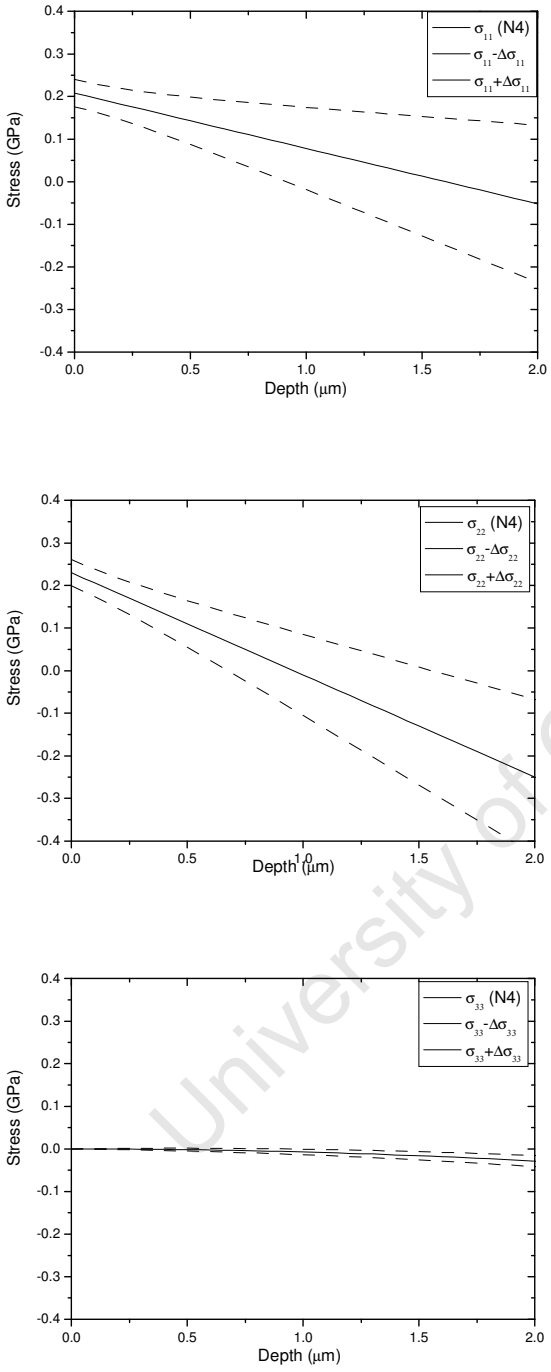

Figure 6.16: Stress depth profile of the normal components of the sample implanted at fluence of 5x10^{15} Kr^{+}/cm^{2}.

Principal stress versus fluence: comparison of the surface stress with the 2-zone model

In Fig. 6.17, the principal stresses versus fluence have been plotted for comparison with the biaxial principal stresses obtained from the $\sin^2\psi$ analysis (Fig. 6.9). Here the principal stresses at the surface for the (101) and (100) reflections combined are used for comparison. As can be seen in both analyses the behaviour of the principal stresses is similar, although the stress values and errors for the depth profiling are higher than those calculated in the case of the biaxial stress analysis. In both cases, the stress value increases in the first stage of implantation but after fluence of $1x10^{14}$ Kr^+/cm^2, it decreases. At the highest fluence, the stress reaches a value below that of the unimplanted sample. In other words, as the implantation dose increases, the stress is observed to rise to a maximum at an intermediate fluence. Thereafter, as the fluence is increased further, the residual stress is found to decrease.

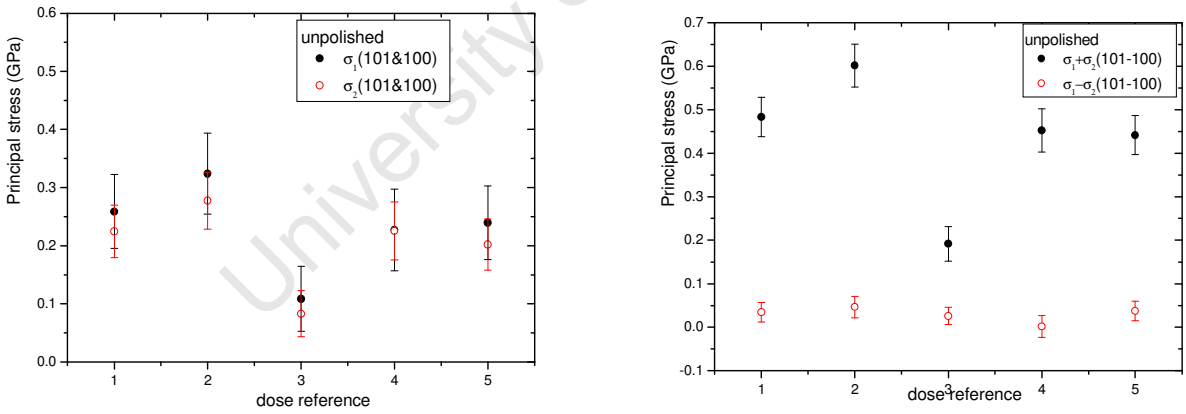

Figure 6.17: Principal stress versus implantation dose. The unimplanted sample corresponds to dose reference 1, $1x10^{14}$ Kr^+/cm^2 to 2, $5x10^{14}$ Kr^+/cm^2 to 3, $1x10^{15}$ Kr^+/cm^2 to 4, and $5x10^{15}$ Kr^+/cm^2 to 5.

b) polished samples

The stress profile of the normal stresses of the polished samples is different from that of the unpolished samples. The stress profiles do not change sign for either the unimplanted sample or for the implanted samples, shown in Figs 6.18 to 6.22. They remain compressive even under implantation. The sharpness of the stress profile observed in the unpolished samples is not reflected in the polished samples. The increase in the compressive stress is rather smooth except for the sample implanted at fluence of $1x10^{14}$ Kr^{+}/cm^{2}.

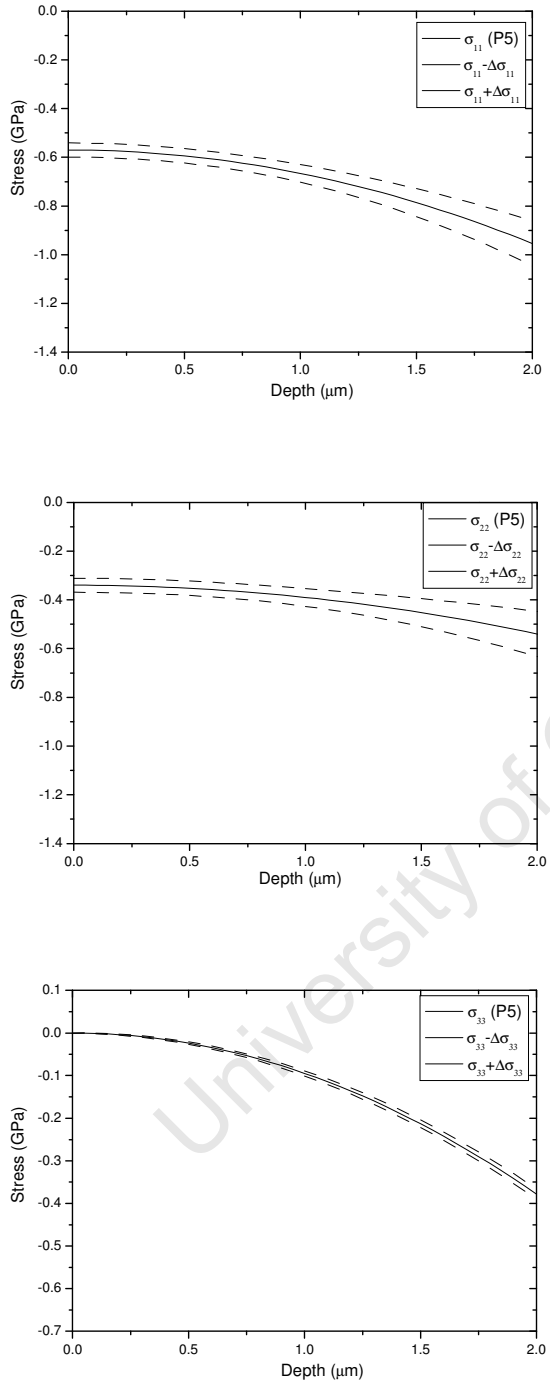

Figure 6.18: Stress depth profile of the normal components of the polished sample.

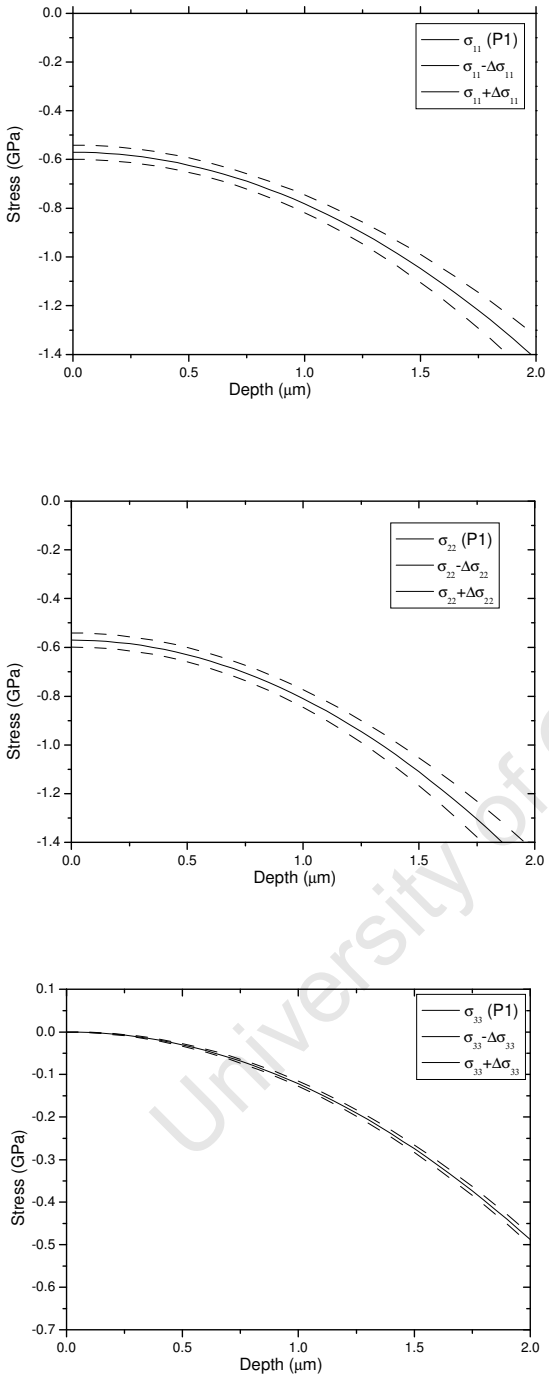

Figure 6.19: Stress depth profile of the normal components of the sample implanted at fluence of 1x10^{14} Kr^{+}/cm^{2}.

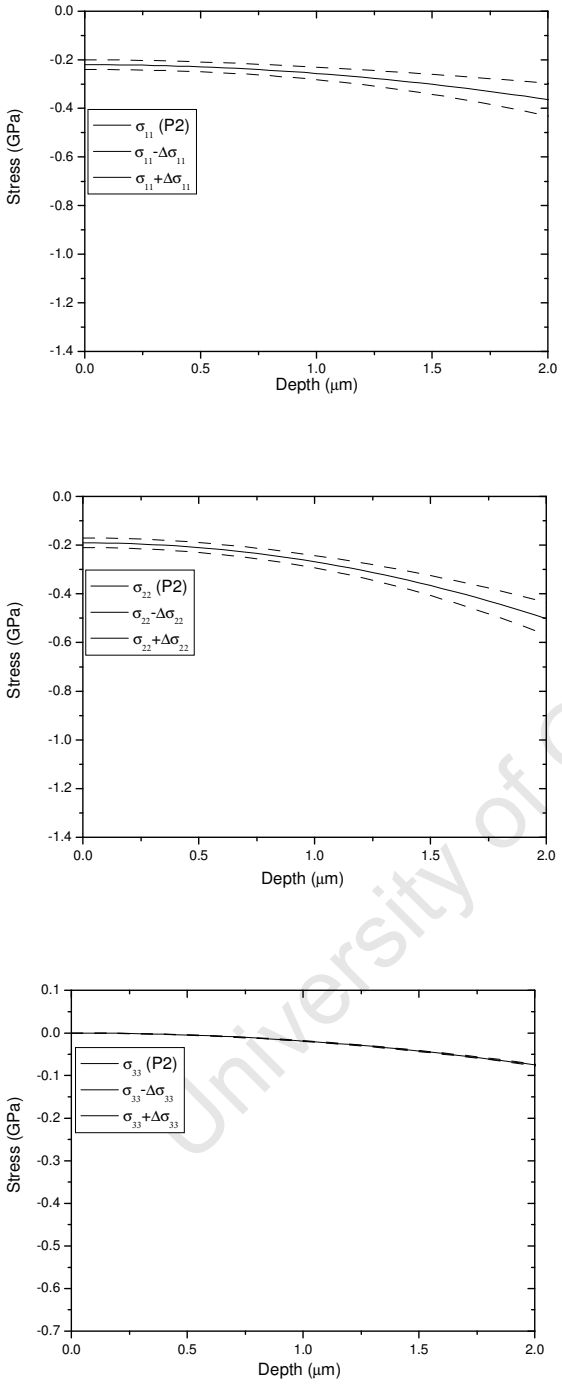

Figure 6.20: Stress depth profile of the normal components of the sample implanted at fluence of 5x10^{14} Kr^{+}/cm^{2}.

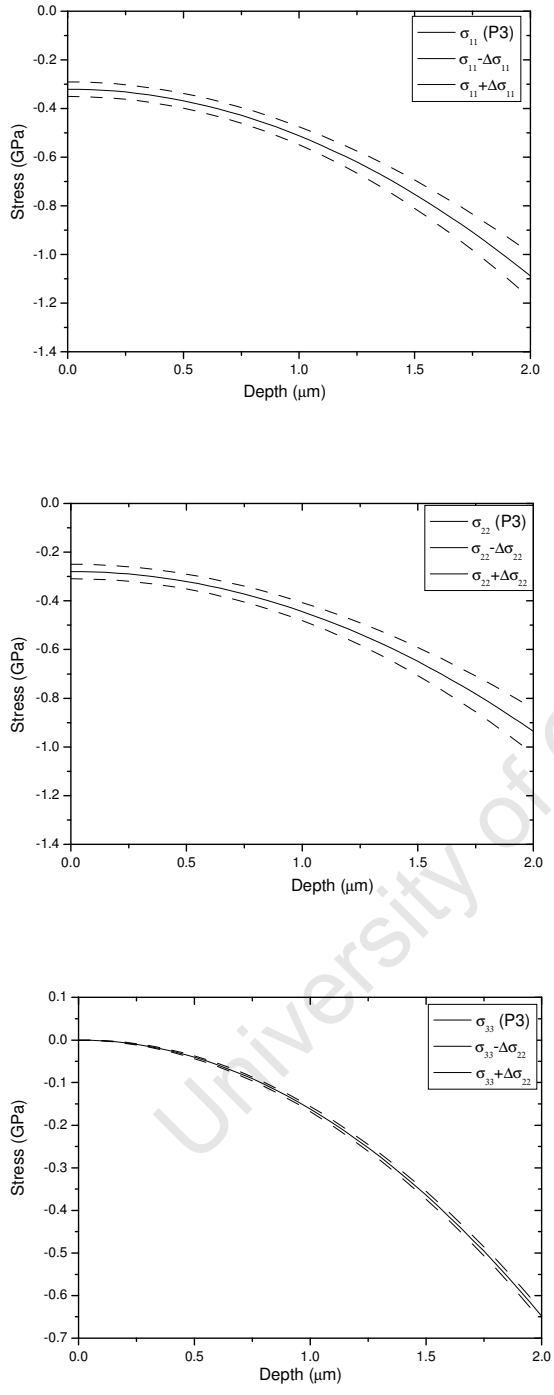

Figure 6.21: Stress depth profile of the normal components of the sample implanted at fluence of 1x10^{15} Kr^{+}/cm^{2}.

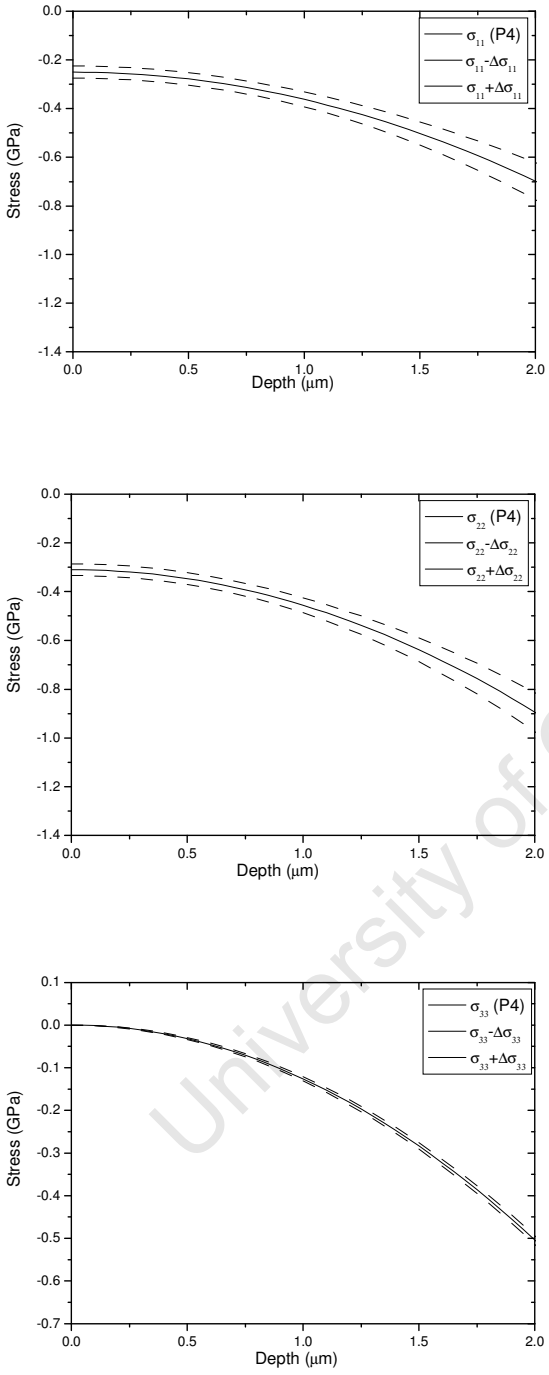

Figure 6.22: Stress depth profile of the normal components of the sample implanted at fluence of 5x10^{15} Kr^{+}/cm^{2}.

Principal stress versus fluence: comparison of the surface stress with the 2-zone model

Although the uncertainties are large compared to the unpolished samples, the surface stress components, in Fig. 6.23 show a similar trend to that observed for the surface region in the two-zone model, Fig. 6.10. On implantation there is a continuous decrease in the compressive stress. Similarly, there is only a slight anisotropy which decreases with fluence.

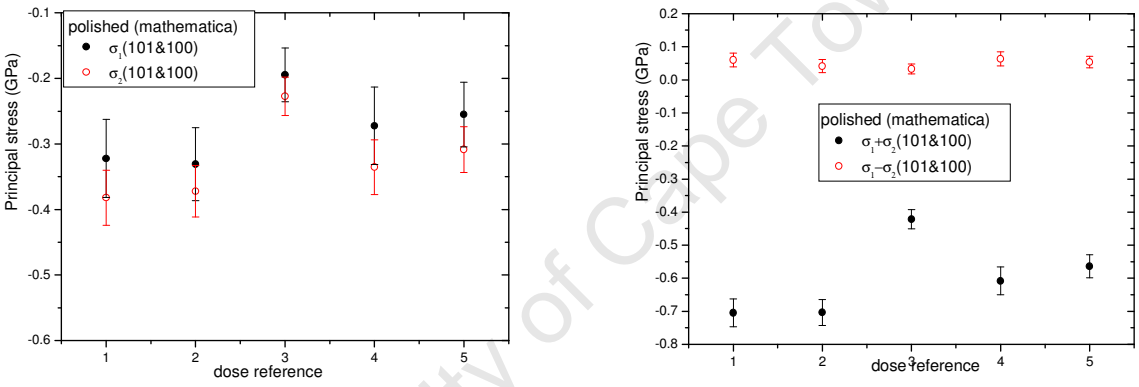

Figure 6.23: Principal stress versus implantation dose. The polished unimplanted sample corresponds to dose reference 1. Polished implanted: 1x10^{14} Kr^{+}/cm^{2} to 2, 5x10^{14} Kr^{+}/cm^{2} to 3, 1x10^{15} Kr^{+}/cm^{2} to 4, and 5x10^{15} Kr^{+}/cm^{2} to 5.

7 DISCUSSION

This thesis focuses on the mutual influence of strain fields and interstitial atom distributions in krypton implanted polycrystalline titanium. The as-received samples are pure α-titanium discs, of 25 mm diameter and 0.33 mm thickness, cut from rolled sheet in half-hard conditions. Before the implantation process, the samples were divided into two batches. The first batch consisted of five samples in their as-received condition, whereas the second batch consisted of five samples polished in order to obtain samples with a different stress distribution in the near surface region. The unpolished samples also had a higher concentration of oxygen impurities extending deeper into the sample. The discussion which follows is divided into three main parts. The first part will discuss the effect of implantation on the oxygen profile, the second part will discuss the effect of stress on the implanted ions, and the last part will focus on the effect of implantation on stress for both sets of samples.

7.1 Effect of implantation on the oxygen profile

The following analysis is based on the oxygen profile results obtained in section 6.2, and plotted in Fig. 6.4. Using these results, the oxygen mean concentration and the oxygen mean depth are calculated for each sample. The procedure followed is sketched in Fig. 7.1. The oxygen mean concentration C is calculated by averaging all areas A_i in the histogram of the depth profile, *i.e.* oxygen concentration c_i times the layer width w_i divided by the maximum oxygen depth L_{max},

$$C = \frac{\sum A_i}{L_{max}}. \qquad (7.1)$$

The oxygen mean depth D is calculated from the centroid of the distribution,

$$D = \frac{\sum (L_i - w_i/2) c_i}{\sum c_i}. \qquad (7.2)$$

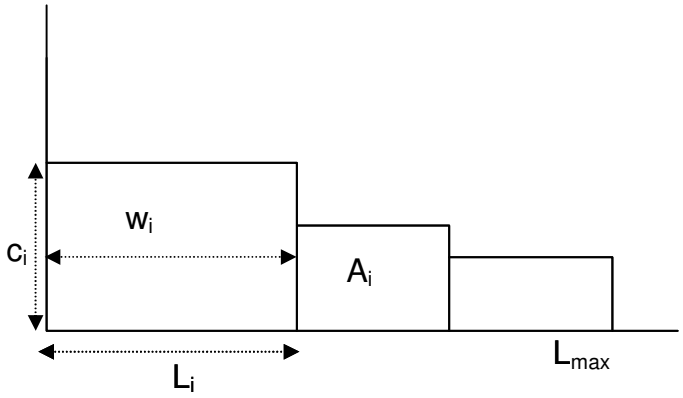

Figure 7.1: Sketch showing the parameters used to calculate the oxygen mean concentration and the oxygen mean depth. A_i is the area corresponding to the oxygen concentration c_i times the oxygen depth L_i for every layer, and w_i is the layer width.

To illustrate the effect of implantation on the oxygen profile, the mean oxygen concentration and the mean oxygen depth for both unpolished and polished samples are plotted as a function of fluence in Fig.7.2. The solid and dashed lines are guides to the eye. Three regimes, *i.e.* low fluence, intermediate fluence and high fluence, are apparent in the data.

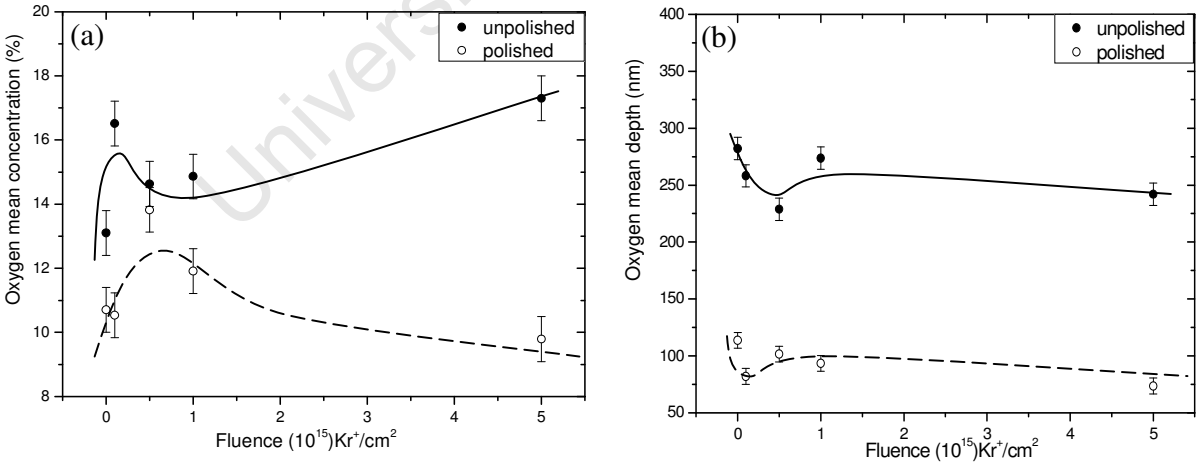

Figure 7.2: (a) *Oxygen mean concentration versus fluence; (b) Oxygen mean depth versus fluence, for both polished and polished samples. The lines are guides to the eye.*

At low fluence, there is an increase of the mean concentration of oxygen in both unpolished and polished samples. However in this regime, the mean depth of the oxygen decreases compared to the unimplanted samples. At intermediate fluence, there is a slight recovery in both mean depth and concentration. At higher fluences the depth of the oxygen distribution decreases slightly for both polished and unpolished samples. In contrast the average concentration of oxygen in the unpolished samples increases, whereas it decreases in the polished samples. The behaviour for low dose implantation suggests a knock-on implantation of surface oxygen atoms. In the second regime, and also at high dose for the polished sample, where an overall decrease in the mean concentration and mean depth of oxygen is observed, the suggestion is that an out-diffusion of near-surface oxygen atoms takes place.

7.2 Effect of stress on implanted krypton ions

Using SRIM [7.1], the krypton projected range and the straggling were calculated, and the values of 698 Å, and 271 Å respectively were obtained. Taking into account the sputtering process at the highest dose, these values are reduced to 673 Å and 246 Å but remain higher than the experimental values shown in Table 6.1. The projected range values of the samples implanted at higher fluence are about 15% lower than the calculated projected range. This indicates that the krypton ions do not implant as deep as expected. From the experimental results, it was observed that, as the fluence decreases the krypton concentration also decreases, leading to the increase in error of the projected range and the straggling. It was observed, on the other hand, that for the same fluence the projected range is deeper, and the straggling higher in the unpolished samples than in polished samples. With respect to the calculated projected range, at higher fluences the deviation from the expected range is less at high fluences than at lower fluences. The mechanism that leads to the shallower distribution of krypton ions is unlikely to result from back-scattering in the

collisions between krypton ions and the host target atoms, simply because the krypton atomic mass is higher than the titanium atomic mass, as discussed in section 5.2. There should therefore be other mechanisms involved which lead to a motion of the krypton ions towards the surface. A drift mechanism under local strain fields of other defects in titanium might be the cause of the out-diffusion of krypton ions. As discussed in section 4.3, the force on a defect can be calculated using Eq. (4.11),

$$F = \alpha \frac{4}{3} \pi r_0^3 \nabla Tr(\sigma) = \Delta V \nabla Tr(\sigma), \qquad (7.1)$$

where ΔV is the volume relaxation of the interstitial site around a krypton atom in titanium.

The value of ΔV used in the following discussion was 31.3(Å)^3, and was obtained from ab initio calculations by A.T. Raji in our research group [priv. com]. The trace of the stress was obtained from the coefficients of depth profiling in Eq. (5.47), and by differentiating the series expansion, $\partial Tr(\sigma)/\partial z$ was obtained at the experimentally determined projected range. The mobility is a measure of how fast a defect can be moved, on average, under the influence of an applied force. Its product with the average force gives the mean drift velocity,

$$< v >= \mu < F > . \qquad (7.2)$$

Multiplying by the time over which the drift occurs yields an estimate for the change in projected range,

$$\delta R_p = < v > t = \mu < F > t . \qquad (7.3)$$

In Fig 7.3, the projected range R_p versus $< F > t$ is plotted. The time t was assumed to be the implantation time for low dose implantation of each sample. In the figure, a linear dependence of R_p on $< F >$ is clearly seen, but it should be

noted that the approximation made here is only valid for low fluence. At high fluence, a strong deviation from the linear dependences arises due the higher stress relaxation and changes in the defect structure taking place in this regime.

From the slope of the graph, the value of the krypton mobility is estimated to be about 10^{12} $cm^2/J.s$. Using the Nernst-Einstein relation (Eq. (4.4)), the diffusion coefficient *D* of krypton in titanium was calculated assuming a temperature of 300K, and a value of about $4x10^{-9}cm^2/s$ was obtained. In comparison with the calculated diffusion coefficients of elements, such as boron and nickel diffusing in titanium, it is found that the krypton diffusion coefficient is in the same order of magnitude as boron diffusion coefficient, which value is about $1{\cdot}2x10^{-9}cm^2/s$ [7.2], but higher than of nickel in titanium [7.3], whose value is about $10^{-12}cm^2/s$. From this comparison, it can be seen that krypton may diffuse faster than boron, which is known to be a fast interstitial diffuser in titanium. Krypton is one of the noble gases, and is therefore very insoluble in metals. Owing to this property, fast diffusion should be expected. However, another factor which enhances drift could be a high local equilibrium temperature during the implantation, associated with the thermal spikes. It is important to bear in mind that the krypton profiles were determined long after implantation, so that the measured krypton profile is "frozen in" at room temperature. The absolute numerical value of the diffusion coefficient should therefore be treated with caution, as the mobility corresponds to an unknown temperature above room temperature. Nevertheless Fig. 7.4 is a clear indication of stress induced diffusion of interstitial krypton in titanium.

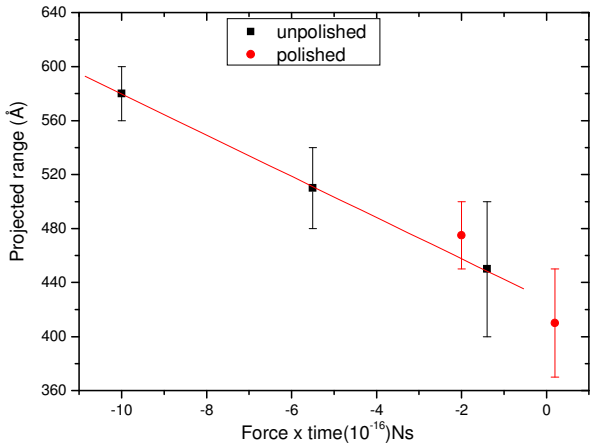

Figure 7.3: Projected range versus Force x time for unpolished and polished implanted at low fluence. From the slope of the graph, the mobility of krypton is obtained.

7.3 Effect of implantation on stress.

For unpolished samples, low fluence increases the near surface tensile stress, but further implantation reduces the tensile stress significantly. This reduction was observed in a previous study at higher fluences [7.4], whereby a tensile stress was reduced by about 30 % without any significant change in open-volume defect structure. This suggested that the main cause of this reduction was an implantation induced stress relaxation. Similar stress relaxation has been observed in other materials. For instance, with several hundreds keV energy of boron and phosphorus implanted tungsten [7.5], stress is reduced to about 10% of the original value. In argon implanted cubic boron nitride films [7.6], argon implanted copper foils [7.7], and argon zirconium nitride films [7.8], stress relaxation has also been observed. Mechanisms contributing to this relaxation are attributed to defect annealing mechanisms, or localized thermal effects [7.9], Newtonian viscous flow or creep [7.5, 7.10], deformation induced by the high energy ion [7.11].

In the present work, more extensive stress analysis was performed for lower dose implantation using a two-zone model for the biaxial stress, uniaxial projected strain representation, and a semi-numerical analysis to determine the stress profile. All analyses give similar consistent results for both polished and unpolished samples. The surface stress was found to become more isotropic with implantation. For low dose implantation, the stress becomes more tensile, whereas the magnitude of the stress relaxes for high dose. The dose range where stress becomes more tensile corresponds to the regime where the stress-induced diffusion relationship $\Delta R = < F > t$ holds. Overall this suggests that at low dose, implantation introduces a new source of tensile stress, whose origin might be due to the presence of point or open volume defects. At higher doses, stress relaxation is observed. The cause of this relaxation is probably annealing due to thermal spike effects [7.5-7.9], but there may be contributions from plastic flow, and dislocation movement during clustering [7.5,7.10]. However, to investigate this more fully a more extended series of experiments, utilizing other techniques sensitive to extended defects, in the higher dose regime would be necessary. Techniques which could be applied include positron beam life spectroscopy for open-volume defects, electron microscopy to investigate dislocation networks and krypton inclusions, and small angle scattering to study clustering and the ordering of krypton bubbles.

8 CONCLUSIONS

The purpose of this work was to enlighten the basic processes of defect interactions with strain fields using an experimental approach. In the results, both stress induced point defect diffusion and stress relaxation were observed. This has been achieved by creating a well designed model system of krypton implanted polycrystalline titanium. The specific features of this model system were 2-fold: firstly the implantation has been performed at low dose to avoid clustering and larger defect formation, and secondly the choice of inert insoluble species implantation does not bring about any phase change or substitution of the implanted ions into the structure. The experimental techniques therefore focused on how foreign interstitial atoms behave with respect to the pre-existing stress field and other stress fields. To carry out this investigation, two sets of samples were chosen, one having a high stress gradient and the second a low stress gradient, in the near surface region.

Two experimental methods were chosen very carefully in this investigation. To obtain the krypton profile, ion beam analysis using Rutherford backscattering spectrometry has been used. The study of the oxygen profile has also been investigated using resonance RBS. To obtain accurate determination of stress fields, numerical analysis of diffraction data from a 2nd generation synchrotron radiation facility was used. With this approach, we were able to investigate the near surface region, in a depth range where other established techniques such as etching, or modern techniques, such as strain scanning with synchrotron microbeams, cannot achieve.

The results obtained show clearly that the change in krypton range correlates with the stress gradient. This has been confirmed from the comparison of the calculated projected range values and the experimental projected range values of krypton ions in titanium. It was observed that the experimental values for all

set of samples are lower than the calculated values. The mechanism that leads to the shallower distribution of krypton ions is unlikely to result from back-scattering in the collisions between krypton ions and the host target atoms, for the simple reason that the krypton atomic mass is higher than the titanium atomic mass. A mechanism of forced diffusion of was proposed and tested. The linear dependence of the projected range R_p on the average force F on a defect, which yields the krypton mobility, is a clear indication of stress induced diffusion of interstitial krypton in titanium. This was observed at low fluence. At high fluence, a strong deviation from the linear dependence arises due the higher stress relaxation and changes in the defect structure taking place in this regime. Calculations based on this model showed that krypton diffusion coefficient was higher than that of other interstitials, such as boron and nickel diffusing in titanium. Another factor contributing to the high mobility is the high local equilibrium temperature during the implantation, associated with thermal spikes.

It was also observed in this work that implantation significantly reduces the tensile stress in the set of samples with a high pre-existing stress. All analyses, using both a two-zone model for the biaxial stress, and the stress profile for triaxial stress, convey similar consistent results for both types of samples. Upon implantation, the surface stress was found to become more isotropic. For low dose, the stress becomes more tensile, whereas the magnitude of stress relaxes for high dose. The dose range where stress becomes more tensile corresponds to the regime where the stress-induced diffusion relationship $\Delta R = < F > t$ holds. Overall this suggests that at low dose, implantation introduces a new source of tensile stress, whose origin might be the presence of point and open volume defects. At higher doses, stress relaxation is observed. The cause of this relaxation is probably due to a defect annealing mechanism, or localized thermal effects, or plastic flow [7.1 - 7.5].

The investigation carried of the oxygen profile, using oxygen resonance scattering shows that, at low fluence there is an increase of the mean concentration of oxygen in both sets of samples. This is attributed to a knock-on implantation of surface oxygen atoms. In the second regime, and also at high fluence for the materials with a deeper profile, an overall decrease in the mean concentration and mean depth of oxygen is observed. This suggests that an out-diffusion of near-surface oxygen atoms takes place.

For the study of extended defects in the high fluence regime, other techniques sensitive to such defects would be necessary. Techniques which could be applied include positron beam life spectroscopy for open-volume defects, electron microscopy to investigate dislocation networks and krypton inclusions, and small angle scattering to study clustering and the ordering of krypton bubbles. These should be combined with the techniques used in this work, including a more detailed description of the local strain fields around such defects.

REFERENCES

CHAPTER 1

[1.1] J.S. Williams, Materials modification with ion beams, Rep. Prog. Phys. **49** (1986) 491.

[1.2] C.A. dos Santos, B.A.S. de Barros, J.P. de Souza, and I.J.R. Baumvol, Iron nitride and carbonitride phases in a nitrogen implanted carbon steel, Appl. Phys. Lett. **41** (1982) 237.

[1.3] M. Carbucicchio, L. Bardani, and S. Tosto, Surface Mössbauer analysis of 38NCD4 steel ion implanted with nitrogen, J. Appl. Phys. **52** (1981) 4589.

[1.4] R. Frattini, G. Principi, S. Lo Russo, B. Tiveron and C. Tosello, Mössbauer surface study of a nitrogen-implanted medium-carbon, J. Mater. Sci. **17** (1982) 1683

[1.5] G. Dearnaley, Science of hard materials, Plenum, New York, 1983.

[1.6] R. Hutchings, A study of the improved wear performance of nitrogen-implanted Ti-6Al-4V, Wear, **92** (1983).

[1.7] S. Soritas, R.P.M. Procter, V. Ashworth, and W.A. Grant, The effect of ion implantation on the friction and wear behaviour of a phosphor bronze, Wear **82** (1982) 233.

[1.8] C.J. McHargue, Ion implantation in metals and ceramics, International Metals Reviews **31** (1986) 49.

[1.9] E.Yagi, Lattice location study on krypton atoms in aluminium by means of the channelling method, Nucl. Instr. Meth. B39 (1989) 68.

[1.10] A.D. Marwick, Ion beam characterization and treatment, Metallurgical Transactions A**20** (1989) 2627.

[1.11] J.H. Evans and D.J. Mazey, The formation of solid krypton bubbles in molybdenum, Scripta Metal. **19** (1985) 621.

[1.12] C. Ronchi, On diffusion and precipitation of gas-in-solid, J. Nucl. Mater. **148** (1987) 316.

[1.13] J.H. Evans and D.J. Mazey, Evidence for solid krypton bubbles in copper, nickel and gold at 293 K, J. Phy. F. **15** (1985) L1.

[1.14] C. Templier, H. Garem, J.P. Rivière, and J. Delafond, Solid and fluid Xenon in Xe implanted Aluminium, Nucl. Instr. Meth. **B18** (1986) 24.

[1.15] P.W. Winter and D.A. Macinnes, An analysis of the thermodynamics of gas atoms in very small bubbles, J. Nucl. Mater. **114** (1983) 7-14.

[1.16] D.J. Mazey and J.H. Evans, Solid bubble formation in titanium injected with krypton ions, J. Nucl. Mater. **138** (1986) 16.

[1.17] A. van Veen, Helium defect interactions in metals and silicon, Fundamental aspects of inert gases in solids, S.E. Donnelly and J.H. Evans (Ed), Plenum Press, New York, 1991, p41.

[1.18] P. Jung, Diffusion and clustering of helium in noble metals, Fundamental aspects of inert gases in solids, S.E. Donnelly and J.H. Evans (Ed), Plenum Press, New York, 1991, p59.

[1.19] D. Fink, L. Wang, and J. Martan, Mobility of helium and nitrogen implanted at high fluences into solids, as derived from their concentration profiles, Fundamental aspects of inert gases in solids, S.E. Donnelly and J.H. Evans (Ed),Plenum Press, New York, 1991, p67.

[1.20] B.O. Hall, Stress distribution in helium-ion implantations, J. Nucl. Mat **63** (1976) 285.

[1.21] D.S. Whitmell, Immobilization of krypton in a metallic matrix, Nucl. Energy, **21** (1982) 181.

[1.22] E. Snoeks, K.S. Boutros, and J. Barone, Stress relaxation in tungsten by ion irradiation, Appl. Phys. Lett. **71** (1997) 267.

[1.23] N. Durand, K.F. Badawi, and Ph. Goudeau, Residual stresses and microstructure in tungsten thin films analyzed by x-ray diffraction-evolution under ion irradiation, J. Appl. Phys. **80** (1996) 5021.

[1.24] M.Y. Inal, M. Alam, R.A. Peascoe, T.R. Watkins, Residual stress in deuterium implanted nominal copper coatings, J. Appl. Phys. **88** (2000) 3919.

[1.25] C.H. Woo, Defect accumulation behaviour in hcp metals and alloys, J. Nucl. Mater. **276** (2000) 90.

[1.26] G. Carter, Peening in ion-assisted thin-film deposition: a generalised model, J. Phys. D: Appl. Phys. **27** (1994) 1046.

[1.27] S.G. Mayr, and R.S. Averback, Effect of ion bombardment on stress in thin metal films, Phys. Rev. B **68** (2003) 214105.

[1.28] E. Snoeks, and A. Polman, Densification, anisotropic deformation, and plastic flow of SiO_2 during MeV heavy ion irradiation, Appl. Phys. Lett. **65** (1994) 2487.

[1.29] H. Trinkaus, Local stress-relaxation in thermal spikes as a possible cause for creep and macroscopic stress-relaxation of amorphous solids under irradiation, J. Nucl. Mater. **223** (1995) 196.

[1.30] T.D. de la Rubia, R.S. Averback, R. Benedek, and W.E. King, Role of thermal spikes in energetic displacement cascades, Phys. Rev. lett. **59** (1987) 1930.

[1.31] T. Leguey, N. Baluc, R. Schäublin, and M. Victoria, Structure-mechanisms relationships in proton irradiated pure titanium, J. Nucl. Mater. **307-311** (2002) 696-700.

[1.32] O. Tabata, S. Sugiyama, and M. Takigawa, Control of internal stress and Young's modulaus of Si_3N_4 and polycrystalline silicon thin films using ion implantation technique, Appl. Phys. Lett. **56** (1990) 1314.

[1.33] Q. Wang, H. Ogiso, S. Nakano, J. Akedo, and H. Ishikawa, Martensitic transformation and the stress induced by 3 MeV ion implantation in an austenite stainless steel sheet, Nucl. Instr. Meth. B. **206** (2003) 118.

[1.34] A.J. Perry, and D.E. Geist, On the residual stress profile developed in titanium nitride by ion implantation, Nucl. Instr. Meth. **B127/128** (1997) 967.

[1.35] M.J. Marques, J. Pina, A.M. Dias, J.L. Lebrun, and J. Feugeas, X-ray diffraction characterization of ion-implanted austenitic stainless steel, Surf. and Coat. Technol. **195** (2005) 8-16.

[1.36] W.J. Phythian, Collapse of displacement cascades in hcp metals, C.A. English, and D.H. Yellen, Phil. Mag. A **63** (1991) 821.

[1.37] B.L.Eyre, Transmission electron microscope studies of point defect clusters in fcc and bcc metals, J. Phys. F: Metal Phys. **3** (1973) 422.

[1.38] M. Griffiths, Evolution of microstructure in hcp metals during irradiation, J. Nucl. Mater. **205** (1993) 225.

[1.39] T. Leguey, N. Baluc, R. Schäublin, and M. Victoria, Temperature dependence of irradiation effects in pure titanium, Phil. Mag. **85** (2005) 689.

CHAPTER 2

[2.1] H. Bernas, and P. Nedellec, Structural and electronic properties of ion implanted superconductors, Nucl. Instr. Meth. **182-183** (1981) 845.

[2.2] J.M. Shanon, Shallow implanted layers in advanced silicon devices, Nucl. Instr.Meth. **182-183** (1981) 545.

[2.3] L. Rubin and J. Poate, Ion implantation in Silicon technology, The Industrial Physicist, June/July 2003.

[2.4] H. Trinkhaus, B.N. Singh, and I. Golubov, Progress in modeling the microstructural evolution in metals under cascade damage conditions, J. Nucl. Mater. **89** (2000) 283.

[2.5] S. T. Picraux, Ion implantation in metals, Ann. Rev. Mater. Sci. **14** (1984) 335.

[2.6] C.J. McHargue, Ion implantation in metals and ceramic, International Metals Reviews, **31** (1986) 49.

[2.7] K.E. Dickson, The development of ion implantation technology in the UK semiconductor industry, Phys. Technol., **16** (1985) 171.

[2.8] L.E. Rehn, R.S. Averback, and P.R. Okamato, Fundamental aspects of ion-beam surface modification – Defect production and migration processes, Mat. Sc. Eng. **69** (1985) 1.

[2.9] G. Dearnaley, The modification of materials by ion implantation, Phys. Technol. **14** (1983) 225.

[2.10] D. Fink, and Lewis T. Chadderton, Ion-solid interaction: status and perspectives, Brazilian Journal of Physics, **35**, 3B, (2005) 735.

[2.11] P. Sigmund, Stopping power: Wrong terminology, ICRU News June 2000, p.5-6.

[2.12] J.S. Williams, Materials modification with ion beams, Rep. Pro. Phys. **49** (1986) 491.

[2.13] A.D. Marwick, Ion Beam Characterisation and treatment, Metall. Trans. A **20** (1989) 2627.

[2.14] H. Amekura, and V. Voitsenya, T.T. Lay, Y. Takeda, and N. Kishimoto, X-ray emission induced by 60 keV high-flux copper negative ion implantation, Jpn. J. Appl, Phys. **40** (2001) 1094.

[2.15] V.Kh. Fergeler, S.F. Belykh, R.N. Evtukhov, and I.V. Redina, Ion-photon emission from metals implanted with ions of reactive elements, Nucl. Instr. Meth. B**95** (1995) 300.

[2.16] Z. Xiao, G. Cheng, T. Zhang, F. Xu, Up-conversion luminescence from neodymium ion implantation silicon, Surf. Coat. Technol. **128-129** (2000) 461.

[2.17] R.A. Baragiola, E.V. Alonso, and A. Oliva-Florio, Electron emission from clean metal surfaces induced by low-energy light ions, Phys. Rev. B **19** (1979) 121.

[2.18] M. Nastasi, J. Mayer, and J.K. Hirvonen, Ion-solid interactions: Fundamentals and Applications, Cambridge University Press, 1996.

[2.19] J. Lindhard and M. Scharff, Energy dissipation by ions in the keV region, Phys. Rev.**124** (1961) 128.

[2.20] S. Hofman, Sputter depth profile analysis of interfaces, Rep. Prog. Phys. **61** (1998) 827.

[2.21] J.F. Ziegler, J.P. Biersack. SRIM: the stopping and ranges of ions in matter, Pergamon Press, New York, 1985.

[2.22] D.J. Bacon, F. Gao, Yu. N. Osetsky, The primary damage state in fcc, bcc, and hcp metals as seen in molecular dynamics, J. Nucl. Mat. **276** (2000) 1.

[2.23] E.M. Bringa, B.D. Wirth, M.J. Caturla, J. Stolken, D. Kalantar, Metals far from equilibrium: From shocks to radiation damage, Nucl. Instr. Meth. B **202** (2003) 56.

[2.24] G.D. Watkins, Lattice vacancies and interstitials in silicon, Chinese Journal of Physics, **2** (1977) 92.

[2.25] D. K. Sood, and G. Dearnaley, Radiation damage in copper single crystals, J. Vac. Sci. Technol. **12** (1975) 463.

[2.26] Yu. P. Sharkeev, E.V. Kozlov, A.N. Didenko, S.N. Kolupaeva, N.A. Vihor, The mechanisms of the long-range effect in metals and alloys by ion implantation, Surf. Coat. Techno. **83** (1996) 15

[2.27] M. Vos and D.O. Boerma, Lattice damage in single crystals of Cu after self-implantation studied by channeling, Nucl. Instr. and Meth. B**15** (1986) 337.

[2.28] E. Friedland , N. G. van der Berg, O. Meyer and S. Kalbitzer J.B. Malherbe, Study of implantation damage ranges in metals at temperature ranging from 5 to 300 K, Nucl. Instr. and Meth. B **118** (1996) 29.

[2.29] E. Friedland and H.W. Alberts, Deep radiation damage in metals after ion implantation, Nucl. Instr. and Meth. B**33** (1988) 710.

[2.30] E. Gartstein, Y. Khait, and V. Richter, An X-ray diffraction of implantation damage in InSb reduced by a magnetic field, J. Phys. D: Appl. Phys. **28** (1996) A291.

[2.31] M. Holz, P. Ziemann, and W. Buckel, Direct evidence for amorphisation of pure gallium by low-temperature ion irradiation, Phys. Rev. Lett. **51** (1983) 1584.

[2.32] D.L. Smith, P.C. Rice-Evans, D.T. Britton, J.H. Evans, and A. Allen, Evidence for deep lattice damage in krypton-implanted titanium, revealed by positrons, Phil. Mag.**61** (1990) 839.

[2.33] K.D. Chtcherbatchev, V.T. Bublik, A.S. Markevich, V.N. Mordkovich, E. Alves, N.P. Barradas, and A.D. SequeirK.D. Chtcherbatechev, V.T. Bublik, A.S. Markevich, V.N. Mordkovich, E. Alves, N.P. Barradaa, The influence of in situ photoexcitation on a defect structure generation in Ar^+ implanted GaAs (001) crystals revealed by high-resolution X-ray diffraction and Rutherford backscattering spectroscopy, J. Phys. D: Appl. Phys. **36** (2003) A 43.

[2.34] M. Ali Omar, Elementary Solid State Physics: Principles and Applications, Addison Wesley, 1995, Massachusetts.

[2.35] W. Bolse, Ion-beam induced atomic transport through bi-layer interfaces of low and medium Z metals and their nitrides, Mat. Sci. Rep. R**12** (1994) 53.

[2.36] J.C. Jiménez-Sáez, J. Domínguez-Vázquez, A.M.C. Pérez-Martín, J.J. Jiménez-Rodríguez, Simulation of ion beam induced atomic mixing of interfaces, Vacuum **67** (2002) 635.

[2.37] T. Diaz de la Rubia and M.W. Guinan, New mechanism of defect production in metals: a molecular dynamics study of interstitial-dislocation-loop formation high-energy displacement cascades, Phys. Rev. Lett. **66** (1991) 2766.

[2.38] K. Saarinen, P. Hautojärvi, J. Keinonen, E. Rauhala, and J. Räisänen, Defect structure and recovery in hydrogen-implanted semi-insulating GaAs, Phys. Rev. B **43** (1991) 4249.

[2.39] D.J. Bacon and T.D. de la Rubia, Molecular dynamics computer simulations of displacement cascades in metals, J. Nucl. Mat, 216 (1994) 275.

[2.40] H.L. Heinisch, B.N. Singh, and T.D. de la Rubia, Calibrating a multi-model approach to defect production in high-energy collision cascades, J. Nucl. Mat. **212-215** (1994) 127.

CHAPTER 3

[3.1] J.F. Nye, Physical properties of crystals, their representation by tensors and matrices, Oxford, UK, 1967.

[3.2] I.C. Noyan, J.B. Cohen, Residual stress: Measurement by Diffraction and Interpretation, Springer, New York, 1987.

[3.3] L.D. Landau and E.M. Lifshitz, Course of Theoretical Physics: Vol 7: Theory of elasticity, Pergamon Press, Oxford, UK , 1970.

[3.4] V. Hauk, Structural and Residual Stress Analysis by Nondestructive Methods, Evaluation-Application-Assessment, Elsevier, Amsterdam, 1997.

[3.5] Aaron D. Krawitz, Introduction to diffraction in materials science and engineering, John Wiley & Sons, USA, 2001.

[3.6] B. Eigenmann, E. Macherauch, Mat. –wiss. U. Werkstofftech. **26** (1995) 199.

[3.7] A. Niku-Lari, J. Lu, and J Flavenot, Measurement of residual stress distribution by incremental hole-drilling method, Experimental mechanics, **25** (1985) 175.

[3.8] O. Vöhringer, in Shot Peening, Science-Technology-Application (H. Wohlfahrt, R. Koopp, and O. Vöhringer Eds), DGM Informationsgesellschaft, Oberursel, Germany, 1987, pp184-204.

[3.9] A.B. Sadat, and J.A. Bailey, Residual stress in turned AISI 4340, Experimental mechanics, **27** (1987) 80.

[3.10] J. Pavón, E. Jiménez-Piqué, M. Anglada, S. López-Esteban, E. Saiz and A.P. Tomsia, Stress-corrosion cracking by indentation techniques of a glass coating on Ti6Al4V for biomedical applications, Journal of the European Ceramic Society, **26** (2006) 1159.

[3.11] P. Juijerm, I. Altenberger, and B. Scholtes, Influence of ageing on cyclic deformation behaviour and residual stress relaxation of deep rolled as-quenched aluminium alloy AA6110, International Journal of fatigue, **29** (2007) 1374.

[3.12] J. Ding, R.F. Hall, J. Byrneand, and J. Tong, Fatigue crack growth from foreign object damage under combined low and high cycle loading. Part I: Experimental studies, International Journal of fatigue, **29** (2007) 1339.

[3.13] G. Kirchhoff, Th. Göbel, H. A. Bahr, H. Balke, K. Wetzig, and K. Bartsch, Damage analysis for thermall cycled (Ti, Al)N coatings-estimation of strength and interface toughness, Surf. and Coat. Techn. **179** (2004) 39.

[3.14] S. Hossain, C.E. Truman, D.J. Smith, R.L. Pengand, and U. Stuhr, A study of the generation and creep relaxation of triaxial residual stresses in stainless steel, International journal of solids and structures, **44** (2007) 3004.

[3.15] P. Streitenberger, The stress-driven diffusion of point defects to a slowly moving crack, Computational materials science, **32** (2005) 553.

[3.16] M.S. Daw, W. Winl, N.N. Carlson, M. Laudon, M.P. Masquelier, Effect of stress on dopant and defect diffusion in Si: A general treatment, Phys. Rev. B**64** (2001) 045205.

[3.17] K. Wang, K. Yao, and S. Jin Chua , Titanium diffusion and residual stress of platinum thin films on Ti/SiO2/Si substrate, J. Appl. Phys. **98** (2005) 013538-1.

[3.18] A.M. Simon, and Z.J. Grzywna, On the Larché-Cahn theory for stress-induced diffusion, Acta Metall. Mater.**40** (1992) 3465.

[3.19] B. Eigenmann and E. Macherauch, Determination of grinding residual stress states in surface layers of engineering ceramics using synchrotron X-rays, Z. Metallkd. **86** (1995) 84.

[3.20] P.J. Withers, H.K.D.H. Bhadesia, Residual Stress, Part 2, Nature and Origins, Mat. Sci. Tech. **17**(2005) 366.

CHAPTER 4

[4.1] J. Rottler, David J. Srolovitz, and R. Car, Point defect dynamics in bcc metals, cond-mat, **1** (2004) 1.

[4.2] L.A. Girifalco, and D.O. Welch, Point Defects and Diffusion in Strained Metals, Gordon and Breach, Science Publishers, UK, 1967.

[4.3] S. Mrowec, Defects and diffusion in solids: An introduction, Elsevier Scientific Publishing Company, Poland, 1980.

[4.4] J.R. Manning, Diffusion kinetics for atoms in crystals, Van Nostrand Company, New York, 1968.

[4.5] R.A. Johnson, and A.N. Orlov, Physics of radiation effects in crystals, North-Holland, Amsterdam, 1986.

[4.6] M. Ali Omar. Elementary Solid State Physics: Principles and Applications, Addison-Wesley, California, 1975.

[4.7] D.T. Britton, and M. Härting, The influence of strain on point defect dynamics, Adv. Eng. Mat. **4** (2002) 629.

[4.8] L. Shao, J. Liu, Quark Y. Chen, and Wei-Kan Chu, Boron diffusion in silicon: the anomalies and control by point defect engineering, Mat. Sci. Eng. R, **42** (2003) 65.

[4.9] A.J. Smith, B. Colombeau, R. Gwilliam, N.E.B. Cowern, B.J. Sealy, M. Milosavljevic, E. Collart, S. Gennaro, M. Bersani, M. Barozzi, Suppression of boron interstitial clusters in SOI using vacancy engineering, Mat. Sci. Eng. B, **124-125** (2005) 210.

[4.10] V. Moroz, Yong-Seog Oh, D. Pramanik, H. Graoui, M.A. Foad, Optimizing boron junctions through point defect and stress engineering using carbon and germanium co-implants, Appl. Phys. Lett., **78** (1995) 3664.

[4.11] S. Chaudhry, M.E. Law, The stress assisted evolution of point defect and extended defects in silicon, J. Appl. Phys. **82** (1997) 1138.

[4.12] M.S. Daw, W. Winl, N.N. Carlson, M. Laudon, and M.P. Masquelier, Effect of stress on dopant and defect diffusion in Si: A general treatment, Phy. Rev. B **64** (2001) 045205.

[4.13] P.I. Gaiduk, J. Lundsgaard Hansen, and A. Nylandsted Larsen, Monitoring interstitial fluxes by self-assembled nanovoids in ion-implanted Si/SiGe/Si strained structures, Nucl.Instr.Methods Phys. Res. B**230** (2005) 214.

[4.14] H. Park, K.S. Jones, J.A. Slinkman, and M.E. Law, The stress assisted evolution of point and extended defects in silicon, J. Appl. Phys. **78** (1995) 1138.

[4.15] H. Wipf, The Gorsky effect, electro-transport and thermo-transport of hydrogen in metals, J. Less-Common Metals, **49** (1976) 291.

[4.16] A. C. Lund and P. W. Voorhees, The effects of elastic stress on coarsening in the Ni-Al system, Acta Mater. **50** (2002) 2085.

[4.17] H. Trinkaus, B.N. Singh, and S.I. Gobulov, Progress in modeling the microstructural evolution in metals under cascade damage conditions, J. Nucl. Mater. **89** (2000) 283.

[4.18] D.L. Beke and I.A. Szabó, Diffusion and Stresses, Defect and Diffusion Forum **129-130** (1995)1.

[4.19] M.J. Aziz, Stress effects on defects and dopant diffusion in Si, Materials Science in semiconductor processing **4** (2001) 397.

[4.20] M.J. Aziz, Thermodynamics of diffusion under pressure and stress: Relation to point defect mechanisms, Appl. Phys. Lett. **70** (1997) 2810.

[4.21] P.H. Dererichs, K. Schroeder. Anisotropic diffusion in stress fields, Phys. Rev. B **17** (1978) 2524.

[4.22] M.J. Aziz, P.C. Sabin, G. Lu, The activation strain tensor: Nonhydrostatic stress effects on crystal-growth kinetics Phys. Rev. B**44** (1991) 9812.

[4.23] B.S. Tanenbaum, Plasma Physics, McGraw-Hill, New York, 1938.

[4.24] K. Seeger, Semiconductor Physics, an Introduction 5th, ed., Springer, Berlin, 1991.

[4.25] Qing Ma, S. Chiras, D.R. Clarke, Z. Suo, High-resolution determination of the stress in individual interconnect lines and the variation due to electromigration, J. Appl. Phys. **78** (1995) 1614.

[4.26] J.D. Eshelby, The force on an elastic singularity, Phil. Trans. Roy. Soc. Lond. A **244** (1952) 87.

[4.27] N.F. Mott, F.R.N. Nabarro, An attempt to estimate the degree of precipitation hardening, with a simple model, Proc. Phy. Soc. **52** (1940) 86.

[4.28] J.D. Eshelby, The determination of the elastic field of an ellipsoidal inclusion, and related problems, Proc. Roy. Soc. Lond. A **241** (1957) 376.

[4.29] M. Härting, D.T. Britton, A. Härting, J.M. Schneider, and G. Kostorz, Proc. ECRS-4 (Eds. S. Denis, J.L. Lebrun, B. Bourniquel, M. Barral, J.F. Flavenot), Societé Française de Metallurgie ae de Matériaux, Paris, 1988, 863.

[4.30] F.R.N. Nabarro, The strains produced by precipitation in alloys, Proc. Roy. Soc. Lond. A **175** (1940) 519.

[4.31] L.E. Rehn, R.S. Averback, and P.R. Okamoto, Fundamental of ion beam surface modification: defect production and migration processes, Mat. Sci. Eng. **69** (1985) 1.

[4.32] G.K. Hubler, C.W. White, O.W. Holland, and C.R. Clayton (eds), Ion implantation and ion beam processing of materials, Materials research Society Symp. Proc., vol. 27, Elsevier, New York, 1984.

[4.33] J.W. Mayer (ed.), Proc.4th Int. Conf. On Ion Beam Modification of Materials, Cornell University, Ithaca, New York, July 16-20, 1984.

CHAPTER 5

[5.1] A.T. Raji, Changes in the near-surface stress in titanium caused by krypton ion-implantation, MSc thesis, University of Cape Town (2006).

[5.2] Laboratoire de Physique des Materiaux UMR 6630-CNRS available at http://lmp.sp2mi.univ-poitiers.fr [Accessed on 08 May 2008].

[5.3] W.K. Chu, J.W. Mayer, and M.A. Nicolet, Backscattering Spectrometry, Academic Press, USA, 1978.

[5.4] J.R. Tesmer, M. Nastasi, Handbook of modern Ion Beam Materials Analysis, MRS, Pittsburg, USA, 1995.

[5.5] J.Y. Hsu, J.H. Liang, Y.C. Yu, K.M. Chen, Energy Straggling of He, Li, and B isotopes in Al and Ag, Nucl. Instr. Meth. B **241** (2005) 160.

[5.6] W.K. Chu, Calculation of energy straggling fro protons and helium ions, Phys. Rev. A**13** (1976) 2057.

[5.7] S. Honda, A. Tsujimoto, M. Watamori, and K. Oura, Depth Profiling of Oxygen Concentration of Indium Tin Oxide Films fabricated by Reactive Sputtering, Jpn. J. Appl. Phys. **33** (1994) L 1257.

[5.8] V. Havránek, V. Hnatowicz, J. Kvítek, I. Obsrusník, V. Rybka, and V. Švorčik, Characterisation of thin Si_1O_n surface layers on Si by proton and alpha particle backscattering, Nucl. Instr. and Meth. B**68** (1992) 223.

[5.9] Y.Z. Huang, and D.J. Blackwood, The influence of dissolved oxygen in solution on the titanium oxide growth at different sweep rates, Electrochimica Acta **51** (2006) 3521.

[5.10] K.G. Prasad, M.B. Kurup, P. Singh, G. V. Subba Rao, and A.K. Grover, Estimation of Oxygen content in high Tc superconductors: an accelerator based method, Nucl. Instr. and Meth. B **36** (1989) 485.

[5.11] A. Barcz, A. Panas, and R. Jakiela, Out-and in-diffusion of Oxygen ^{16}O in silicon, Semicond. Sci. Technol. **19** (2004) 1311.

[5.12] G. Mezey, E. Kótai, T. Nagy, L. Lohner, A. Manuba, J. Gyulai, V.R. Deline, C.A. Evans, and R.J. Blattner, A comparisonof techniques for depth profiling oxygen in silicon, Nucl. Instr. and Meth. **167** (1979) 279.

[5.13] M. Heintze, A. Cantana, P.E. Schmidt, F. Lévy, P. Stadelmann, and P. Weiss, Oxygen impurity effects on the formation of thin titanium silicide films by rapid thermal annealing, J. Phys. D: Appl. Phys. **23** (1990) 1076.

[5.14] H.B. Kim, M.H. Cho, S.W. Whangbo, C.N. Whang, S.C. Choi, W.K. Choi, J.H. Song, S.O. Kim, Oxygen distribution in the heteroepitaxially grown Y2O3 films on Si substrates, Nucl. Instr. and Meth. B**142** (1998) 393.

[5.15] A. Vomiero, S. Modena, G.D. Soraru, R. Raj, Y. Blum, G. Della Mea, Investigation on the oxidation of non-Rutheford backscattering spectrometry, Nucl. Instr. and Meth. B**211** (2003) 401.

[5.16] J.R. Cameron, Elastic scattering of alpha-particles by Oxygen, Phys. Rev. **90** (1953) 839.

[5.17] J.F. Ziegler, J.E.E. Baglin, Determination of surface impurity concentration profiles by nuclear backscattering, J. Appl. Phys. **42** (1971) 2031.

[5.18] B. Blanpain, P. Revesz, L.R. Doolittle, K.H. Purser, and J.W. Mayer, The use of the 3.05 MeV oxygen resonance for 4He backscattering near surface analysis of oxygen-containing high Z compounds, Nucl. Instr. and Meth. B**34** (1988) 459.

[5.19] K.K. Bourdelle, Oxygen measurements by elastic backscattering, Nucl. Instr. and Meth. B**66** (1992) 274.

[5.20] W. De Coster, B. Brijs, J. Goemans, and W. Vandervorst, Depth profiling of light-Z elements with elastic resonances: Oxygen profiling with the 3.045 MeV $^{16}O(\alpha,\alpha)^{16}O$ resonance, Nucl. Instr. and Meth. B**66** (1992) 283.

[5.21] M.E.M. Eisa, Optimisation of accelerator optics and the application of nuclear microscopy to the biomedical field. PhD thesis. UCT 2005.

[5.22] L.R. Doolittle, Algorithms for the rapid simulation of Rutherford Backscattering spectra, Nucl. Instr. Meth. B **9** (1985) 291.

[5.23] http://www-nds.iaea.org/. International atomic energy agency website.

[5.24] IC. Noyan, and J.B. Cohen, Residual Stress Measurement by Diffraction and Interpretation, Springer-Verlag, New York, 1987.

[5.25] U. Welzel, J. Ligot, P. Lamparter, A.C. Vermeulen, and E.J. Mittemeijer, Stress analysis of polycrystalline thin films and surface regions by X-ray diffraction, J. Appl. Cryst. **38** (2005) 1.

[5.26] T. Mura, Micromechanics of defects in Solids, Martinus Nijhoff Publishers, Hague, The Netherlands, 1982.

[5.27] I.C. Noyan, Equilibrium conditions for the average stresses measured by X-rays, Met. Trans A **14** (1983) 1907.

[5.28] H. Dölle, The influence of multiaxial stress states, stress gradients and elastic anisotropy on the evaluation of (residual) stresses by X-rays, J. Appl. Crystallography, **12** (1979) 489.

[5.29] V. Hauk, Structural and Residual Stress Analysis by Nondestructive Methods, Evaluation, Application, Assessment, Elsevier, Amsterdam, 1997.

[5.30] A.D. Krawitz, Introduction to Diffraction in Materials Science and Engineering, John Wiley & Sons, Inc, USA, 2001.

[5.31] M. Härting, A seminumerical method to determine the depth profile of the three dimensional residual stress state with X-ray diffraction, Acta Mater. **46** (1998) 1427.

[5.32] V.E. Macherauch, and P. Müller, Das $\sin^2\psi$-Verfahren der, röntgenographischen Spannungsmessung, Z.f. angew. Physik, Bd **13** (1961) 304-312.

[5.33] B.D. Cullity, Elements of X-ray diffraction, 2nd ed., Addison-Wesley, New York, 1978.

[5.34] C.S. Barret, and T.B. Massalski, Structure of Metals, 3rd ed., McGraw-Hill, New York, 1966.

[5.35] M.F. Doerner, and S. Brennan, Strain distribution in thin aluminum films using x-ray depth profiling, J. Appl. Phys. **63** (1988) 126-131.

[5.36] C.J. Shute, and J.B. Cohen, Strain gradients in Al-2% Cu thin films, J. Appl. Phys. **70** (1991) 2104-2110.

[5.37] A. Kumar, U. Welzel* and E. J. Mitteme, A method for the non-destructive analysis of gradients of mechanical stresses by X-ray diffraction measurements at fixed penetration/information depths**,** J. Appl. Cryst. **39** (2006) 633.

[5.38] R.Y. Fillit, and A.J. Perry, Residual stress and X-ray elastic constants in highly textured physically vapor deposited coatings, Surf. and Coat. Technol. **36** (1988) 647.

[5.39] B. Eigenmann, B. Scholtes, and F. Macherauch, Determination of residual stresses in ceramics and ceramic-metal composites by X-ray diffraction methods, Mater. Sci. Eng. A**118** (1989) 1.

[5.40] X. Zhu, P. Predecki, Development of a numerical procedure for determining the depth profiles of X-ray diffraction data, Adv. X-Ray Anal. **37** (1994) 197.

[5.41] C. Genzel, Formalism for the evaluation of strongly non-linear surface stress fields by X-ray diffraction performed in the scattering vector mode, Phys. Stat. Sol. (a) **146** (1994) 629.

[5.42] H. Wern, L. Suominen, Selfconsistent evaluation of non-uniform stress profiles and X-ray elastic constants for X-ray diffraction experiments, Adv. X-ray Anal. **39** (1997) 339.

[5.43] M. Härting, Zertörungsfreie Ermittlung des vollständigen dreidimensionalen Spannungszustandes mit Tiefenauflösung durch Röntgendiffraktion, Ph.D. Thesis, Universität der Bundeswehr München (1994).

[5.44] *Mathematica* ™ software, © 2006 Wolfram Research, Inc. http://www.wolfram.com.

[5.45] D.M. Bates, D.G. Watts, Nonlinear Regression Analysis and Its Applications, John Wiley & Sons, New York, 1988.

[5.46] E. Kröner, Berechnung der elastischen Konstanten des Vielkristalls, Z. Phys. **151** (1958) 504.

[5.47] H. Behnken, and V. Hauk, Berechnung der röntgenographischen Elastizitätskonstanten (REK) des Vielkristalls aus den Einkristalldaten für beliebige Kristallsymmetrie, Z. Metal. **77** (1986) 620.

[5.48] K. Wille, Synchrotron radiation sources, Rep. Prog. Phys. **54** (1991) 1005.

[5.49] www.lnls.br [Accessed on 10 June 2008].

[5.50] 23. IFF-Ferienkurs, Synchrotronstrahlung zur Erforschung kondensierter Materie, 23. März – 3. April 1992, Jülich, Germany.

[5.51] J. Als-Nielsen, and Des McMorrow, Elements of Modern X-Ray Physics, John Wiley & sons, England, 2001.

[5.52] C. Giles, F. Yokaichiya, S.W. Kycia, L.C. Sampaio, D.C. Ardiles-Saravia, M.K.K. Franco, and R.T. Neuenschwander, High –resolution X-ray diffraction beamline at the LNLS for the study of charge, orbital and magnetic structures, J. Synchrotron Rad. **10** (2003) 430.

[5.53] M Härting, S. Nsengiyumva, A.T.Raji, G. Dollinger, P. Sperr, S.R. Naidoo, T.E. Derry, C.M. Comrie, and D.T. Britton, Near Surface Stress Determination in Kr-implanted Polycrystalline Titanium by the X-Ray $\sin^2\Psi$-Method, Surf. and Coat. Technol. **201** (2007) 8237.

[5.54] Certified Scientific Software (1992). SPEC. Certified Scientific Software, PO Box 802168, Chicago, IL 60680, USA.

[5.55] M.C. Correa, H. Tolentino, A.F. Craievich, and A.F. Cusati, Rev, Sci. Instr. **63** (1992) 896.

[5.56] D. Londsale, The accuracy of stress measurement using the X-ray diffraction method, J. Appl. Cryst. **19** (1986) 300.

[5.57] P.S. Prevéy, The use of Pearson VII distribution functions in X-ray diffraction residual stress measurement, Adv. X-ay Anal. **29** (1986) 103.

[5.58] F. Sánchez-Bajo, and F.L. Cumbrera, The use of the Pseudo-Voigt function in the variance method of X-ray line-broadening analysis, J. Appl. Cryst. **30** (1997) 427.

[5.59] H.K. Tönshoff, E. Brinksmeier, and H.H. Nölke, Application of the correlation method in the X-ray residual stress measurement, Z. Metallkde **72** (1981) 349.

[5.60] B.W. Delf, The practical determination of lattice parameters using the centroid method, Brit. J. Appl. Phys. **14** (1963) 345.

[5.61] J.S. Thomsen, Simplified method of computing centroids of X-ray profiles, Acta Cryst. A **24** (1968) 702.

[5.62] W.R. Falk, Data reduction from experimental histograms, Nucl. Instr. Meth. **220** (1984) 473.

[5.63] S. Ergun and M. Berman, Strain effects on diffraction profiles on random-layer lattices, Acta Cryst. A **29** (1973) 12.

[5.64] V.M. Hauk, and E. Macherauch, A useful guide for X-ray stress evaluation (XSE), Adv. X-ray Anal. **27** (1983) 82.

[5.65] A. Fry, Sensitivity Evaluation for X-Ray Diffraction Residual Stress Measurements, NPL Report MATC(A) 104, April 2002.

[5.66] H.P. Klug, and L.E. Alexander, X-ray diffraction procedures for polycrystalline and amorphous materials, 2nd ed., John Wiley & sons, New York, 1974.

[5.67] J. Ladell, W. Parrish, and J. Taylor, Center-of-gravity method of precision lattice parameter determination, Acta Cryst. **12** (1959) 253.

[5.68] R.A. Young, R.J. Gerdes, and J.C. Wilson, Propagation of some systematic errors in X-ray line profile analysis, Acta Cryst. **22** (1967) 155.

CHAPTER 6

[6.1] L.R. Doolittle , Nucl. Instr. Meth. B **9** (1985) 291

[6.2] J.F. Ziegler, J.P. Biersack. SRIM: The stopping and Ranges of Ions in Matter, Pergamon Press, New York, 1985.

[6.3] http://www-nds.iaea.org/. International atomic energy agency website.

[6.4] www.goodfellow.com [Accessed on 16 May 2008].

[6.5] The International Centre for Diffraction data (ICDD)- 1998. Powder Diffraction File-Hexagonal Titanium 5.

[6.6] E. Kröner, Berechnung der elastischen Konstanten des Vielkristalls, Z. Phys. **151** (1958) 504.

[6.7] H. Behnken, and V. Hauk, Berechnung der röntgenographischen Elastizitätskonstanten (REK) des Vielkristalls aus den Einkristalldaten für beliebige Kristallsymmetrie, Z. Metal. **77** (1986) 620.

[6.8] M Härting, S. Nsengiyumva, A.T.Raji, G. Dollinger, P. Sperr, S.R. Naidoo, T.E. Derry, C.M. Comrie, and D.T. Britton, Near Surface Stress Determination in Kr-implanted Polycrystalline Titanium by the X-Ray $\sin^2\Psi$-Method, Surf. and Coat. Technol. **201** (2007) 8237.

[6.9] I.C. Noyan, J.B. Cohen, Residual stress: Measurement by Diffraction and Interpretation, Springer, New York, 1987.

[6.10] M. Yaman, M. Härting, S. Nsengiyumva, and D.T. Britton, Scientific visualization: Analysis, exploration and presentation of tri-axial stress states of Kr^+ implanted titanium determined by X-ray diffraction, Surf. Coat. Tech. **201** (2007) 8431.

CHAPTER 7

[7.1] J.F. Ziegler, J.P. Biersack. SRIM: The stopping and Ranges of Ions in Matter, Pergamon Press, New York, 1985.

[7.2] S.V. Divinski, F. Hisker, T. Wigler, M. Friesel, and Chr. Herzig, Tracer diffusion of boron in α-Ti and γ-TiAl, Intermetallics **16** (2008) 148.

[7.3] H. Nakajima, and M. Koiwa, Diffusion in Titanium, ISIJ International, **31** (1991) 757.

[7.4] M Härting, S. Nsengiyumva, A.T.Raji, G. Dollinger, P. Sperr, S.R. Naidoo, T.E. Derry, C.M. Comrie, and D.T. Britton, Near Surface Stress Determination in Kr-implanted Polycrystalline Titanium by the X-Ray $\sin^2\Psi$-Method, Surf. and Coat. Technol. **201** (2007) 8237.

[7.5] E. Snoeks, K.S. Boutros, and J. Barone, Stress relaxation in tungsten films by ion irradiation, Appl. Phys. Lett. **71** (1997) 267.

[7.6] B. Abendroth, R. Gapo, F. Eichhorn, and W. Möller, X-ray diffraction study of stress relaxation in cubic boron nitride films grown with simultaneous medium-energy ion bombardment, Appl. Phys. Lett. **85** (2004) 5905.

[7.7] W. L. Chan, E. Chason, C. Iamsumang, Surface stress induced in Cu foils during and after low energy ion bombardment, Nucl. Instr. Meth. B **257** (2007) 428.

[7.8] A.J. Pery, B.D. Sartwell, V. Vavolda, D. Rafaja, D.L. William, A.J. Nelson, Residual stress and the effect of implanted argon in films of zirconium nitride made by physical vapour deposition, J. Vac. Sci. Technol. A **10** (1992) 1446.

[7.9] M.Y. Inal, M. Alam, R.A. Peascoe, T.R. Watkins, Residual stress in deuterium implanted nominal copper coatings, J. Appl. Phys. **88** (2000) 3919.

[7.10] C. A. Volkert, Stress and plastic flow in silicon during amorphization by ion bombardment, J. Appl. Phys. **70** (1991).

[7.11] E. Snoeks, and A. Polman, Densification, anisotropic deformation, and plastic flow of SiO_2 during MeV heavy ion irradiation, Appl. Phys. Lett. **65** (1994) 2487.

CHAPTER 8

[8.1] E. Snoeks, K.S. Boutros, and J. Barone, Stress relaxation in tungsten films by ion irradiation, Appl. Phys. Lett. **71** (1997) 267.

[8.2] B. Abendroth, R. Gapo, F. Eichhorn, and W. Möller, X-ray diffraction study of stress relaxation in cubic boron nitride films grown with simultaneous medium-energy ion bombardment, Appl. Phys. Lett. **85** (2004) 5905.

[8.3] W. L. Chan, E. Chason, C. Iamsumang, Surface stress induced in Cu foils during and after low energy ion bombardment, Nucl. Instr. Meth. B **257** (2007) 428.

[8.4] A.J. Pery, B.D. Sartwell, V. Vavolda, D. Rafaja, D.L. William, A.J. Nelson, Residual stress and the effect of implanted argon in films of zirconium nitride made by physical vapour deposition, J. Vac. Sci. Technol. A **10** (1992) 1446.

[8.5] M.Y. Inal, M. Alam, R.A. Peascoe, T.R. Watkins, Residual stress in deuterium implanted nominal copper coatings, J. Appl. Phys. **88** (2000) 3919.

Appendix A Fitting procedure for depth profiling of stress

NonlinearFit[*data*, *model*, *variables*, *parameters*]	fit the data to the model with the named variables and parameters, returning the model evaluated at the parameter estimates achieving the least-squares fit
NonlinearRegress[*data*, *model*, *variables*, *parameters*]	fit the data to the model with the named variables and parameters, returning a list of rules expressing the fit parameter estimates and fit diagnostics

```
<< Statistics`NonlinearFit`
```

$u = 0.01232;$
$v = -0.003032;$
$\mu = 450 * 10^2;$

$$\tau = \frac{\text{Sin}[\theta]\ \text{Cos}[\psi]}{2\,\mu};$$

$\sigma_{11} = c_{11} + \alpha_{11}\,\tau + 2\,\beta_{11}\,\tau^2 + 6\,u_{11}\,\tau^3;$
$\sigma_{22} = c_{22} + \alpha_{22}\,\tau + 2\,\beta_{22}\,\tau^2 + 6\,u_{22}\,\tau^3;$
$\sigma_{33} = 2\,\beta_{33}\,\tau^2 + 6\,u_{33}\,\tau^3;$
$\sigma_{12} = c_{12} + \alpha_{12}\,\tau + 2\,\beta_{12}\,\tau^2 + 6\,u_{12}\,\tau^3;$
$\sigma_{13} = \alpha_{13}\,\tau + 2\,\beta_{13}\,\tau^2 + 6\,u_{13}\,\tau^3;$
$\sigma_{23} = \alpha_{23}\,\tau + 2\,\beta_{23}\,\tau^2 + 6\,u_{23}\,\tau^3;$

$$\epsilon_{33} = u\left(\sigma_{11}\,\text{Cos}[\phi]^2 + \sigma_{12}\,\text{Sin}[2\,\phi] + \sigma_{22}\,\text{Sin}[\phi]^2 - \sigma_{33}\right)\text{Sin}[\psi]^2 + u\,(\sigma_{13}\,\text{Cos}[\phi] + \sigma_{23}\,\text{Sin}[\phi])\,\text{Sin}[2\,\psi] + u\,(\sigma_{33}) + v\,(\sigma_{11} + \sigma_{22} + \sigma_{33});$$

$u\left(=\frac{1}{2}\,S_2\right)$ and $v\ (=S_1)$ are compliances

```
param = {c11, α11, β11, u11, c22, α22, β22, u22, β33, u33, c12, α12, β12, u12, α13, β13, u13, α23, β23, u23};
Length[param]
NonlinearRegress[data, ϵ33, {ϕ, ψ, θ}, param]
```

```
data = {{2.356194, 0, 0.253892993, -0.00201}, {2.356194, 0.174532889, 0.25384936, -0.00185},
  {2.356194, 0.349065778, 0.25384936, -0.00185}, {2.356194, 0.523598667, 0.253657374, -0.00111},
  {2.356194, 0.698131556, 0.253666101, -0.00114}, {2.356194, 0.872664444, 0.253517748, -0.00057},
```

	Estimate	Asymptotic SE	CI
c_{11}	0.278701	0.0349383	{0.20987, 0.347531}
α_{11}	-176717.	100259.	{-374234., 20800.1}
β_{11}	3.60591×10^{9}	2.20276×10^{10}	$\{-3.97899\times10^{10}, 4.70017\times10^{10}\}$
u_{11}	71981.1	226871.	{-374969., 518931.}
c_{22}	0.322779	0.0349363	{0.253952, 0.391605}
α_{22}	-276991.	100264.	{-474519., -79463.3}
β_{22}	2.6474×10^{10}	2.20295×10^{10}	$\{-1.69257\times10^{10}, 6.98737\times10^{10}\}$
u_{22}	279127.	226886.	{-167853., 726107.}
β_{33}	9.86927×10^{9}	1.89052×10^{9}	$\{6.14481\times10^{9}, 1.35937\times10^{10}\}$
u_{33}	51346.2	13437.5	{24873.4, 77819.1}
c_{12}	-0.00747285	0.0209707	{-0.0487865, 0.0338408}
α_{12}	6883.7	63204.4	{-117633., 131401.}
β_{12}	1.96932×10^{9}	1.6492×10^{10}	$\{-3.0521\times10^{10}, 3.44597\times10^{10}\}$
u_{12}	17853.6	149297.	{-276271., 311979.}
α_{13}	-79297.7	153419.	{-381543., 222948.}
β_{13}	1.92157×10^{10}	3.68491×10^{10}	$\{-5.33794\times10^{10}, 9.18109\times10^{10}\}$
u_{13}	213612.	409643.	$\{-593412., 1.02064\times10^{6}\}$
α_{23}	127563.	153430.	{-174704., 429831.}
β_{23}	-2.82935×10^{10}	3.68556×10^{10}	$\{-1.00902\times10^{11}, 4.43146\times10^{10}\}$
u_{23}	-314519.	409719.	$\{-1.12169\times10^{6}, 492654.\}$

EstimatedVariance → 1.00807×10^{-6}, ANOVATable →

	DF	SumOfSq	MeanSq
Model	20	0.000195884	9.79421×10^{-6}
Error	236	0.000237905	1.00807×10^{-6}
Uncorrected Total	256	0.000433789	
Corrected Total	255	0.000421204	

AsymptoticCorrelationMatrix →

1.	-0.813416	0.601707	0.590333	0.279709	-0.187751	0.0823152	0.159228
-0.813416	1.	-0.869601	-0.854037	-0.187735	0.206923	-0.123465	-0.234731
0.601707	-0.869601	1.	0.991395	0.0822154	-0.123318	0.205361	0.331839
0.590333	-0.854037	0.991395	1.	0.15905	-0.234471	0.3317	0.452466
0.279709	-0.187735	0.0822154	0.15905	1.	-0.813398	0.601722	0.590315
-0.187751	0.206923	-0.123318	-0.234471	-0.813398	1.	-0.86962	-0.854009
0.0823152	-0.123465	0.205361	0.3317	0.601722	-0.86962	1.	0.991375
0.159228	-0.234731	0.331839	0.452466	0.590315	-0.854009	0.991375	1.
0.0746003	-0.214278	0.589893	0.648568	0.0743989	-0.213931	0.589539	0.648335
-0.473346	0.673218	-0.773586	-0.848967	-0.473117	0.672892	-0.773333	-0.848834
-0.000206051	0.000309833	-0.000401711	-0.000414153	0.0000170969	-0.0000105449	-0.000060586	-0.000112018
-0.0000296871	0.0000163463	0.0000442447	0.0000663323	-0.0000688535	0.0000726103	-0.0000157184	-9.44898×10^{-6}
0.0000180326	1.52608×10^{-6}	-0.0000582932	-0.0000820839	0.0000634261	-0.000063749	0.0000113395	3.38453×10^{-6}
0.0000952556	-0.000111229	0.0000778091	0.0000605371	0.000107486	-0.000128859	0.0000967076	0.000103902
-0.0000264052	5.00035×10^{-6}	0.000152093	0.00016016	-0.000140602	0.000191614	-0.0000794456	-0.0000315206
0.0000546283	-0.000042059	-0.000140184	-0.000144088	0.000187605	-0.000255871	0.000118994	0.0000705256
0.000245857	-0.000323195	0.000189371	0.000162059	0.000106819	-0.00014624	0.000032436	0.0000312792
0.0000585156	-0.000110096	0.000173414	0.000192283	0.0000598406	-0.000144265	0.000309858	0.000315441
-0.0000354278	0.000074429	-0.000139663	-0.000168647	-0.0000854505	0.000190781	-0.000379028	-0.000377475
0.000176478	-0.000236169	0.000248321	0.000261645	0.000147918	-0.000150646	0.0000418302	0.0000801603

0.0746003	-0.473346	-0.000206051	-0.0000296871	0.0000180326	0.0000952556	-0.0000264052	0.0000546283
-0.214278	0.673218	0.000309833	0.0000163463	1.52608×10^{-6}	-0.000111229	5.00035×10^{-6}	-0.000042059
0.589893	-0.773586	-0.000401711	0.0000442447	-0.0000582932	0.0000778091	0.000152093	-0.000140184
0.648568	-0.848967	-0.000414153	0.0000663323	-0.0000820839	0.0000605371	0.00016016	-0.000144088
0.0743989	-0.473117	0.0000170969	-0.0000688535	0.0000634261	0.000107486	-0.000140602	0.000187605
-0.213931	0.672892	-0.0000105449	0.0000726103	-0.000063749	-0.000128859	0.000191614	-0.000255871
0.589539	-0.773333	-0.000060586	-0.0000157184	0.0000113395	0.0000967076	-0.0000794456	0.000118994
0.648335	-0.848834	-0.000112018	-9.44898×10^{-6}	3.38453×10^{-6}	0.000103902	-0.0000315206	0.0000705256
1.	-0.700997	-0.000299475	0.000116895	-0.00012379	-0.0000118612	0.000336632	-0.000367013
-0.700997	1.	0.00029785	-0.0000195275	0.0000325739	-0.000109077	-0.000121326	0.0000836774
-0.000299475	0.00029785	1.	-0.827812	0.686616	0.686616	0.000137357	-0.000154813
0.000116895	-0.0000195275	-0.827812	1.	-0.940002	-0.940002	-0.000236302	0.000260945
-0.00012379	0.0000325739	0.686616	-0.940002	1.	1.	0.000306611	-0.000332434
-0.0000118612	-0.000109077	0.686616	-0.940002	1.	1.	0.000287689	-0.000313067
0.000336632	-0.000121326	0.000137357	-0.000236302	0.000306611	0.000287689	1.	-0.976963
-0.000367013	0.0000836774	-0.000154813	0.000260945	-0.000332434	-0.000313067	-0.976963	1.
-0.000225747	-0.0000693733	-0.0000928422	0.000175937	-0.000242004	-0.000222601	-0.976963	1.
0.000347872	-0.000280197	0.000334259	-0.000547263	0.000704961	0.000617222	-0.0000186004	0.0000685634
-0.00038094	0.000300463	-0.00039165	0.000638981	-0.000819904	-0.000730096	0.0000685322	-0.000125002
0.0000259081	-0.000217074	-0.0000434871	0.00016214	-0.000312632	-0.000222752	0.0000628033	-0.000119131

0.000245857	0.0000585156	-0.0000354278	0.000176478
-0.000323195	-0.000110096	0.000074429	-0.000236169
0.000189371	0.000173414	-0.000139663	0.000248321
0.000162059	0.000192283	-0.000168647	0.000261645
0.000106819	0.0000598406	-0.0000854505	0.000147918
-0.00014624	-0.000144265	0.000190781	-0.000150646
0.000032436	0.000309858	-0.000379028	0.0000418302
0.0000312792	0.000315441	-0.000377475	0.0000801603
-0.000225747	0.000347872	-0.00038094	0.0000259081
-0.0000693733	-0.000280197	0.000300463	-0.000217074
-0.0000928422	0.000334259	-0.00039165	-0.0000434871
0.000175937	-0.000547263	0.000638981	0.00016214
-0.000242004	0.000704961	-0.000819904	-0.000312632
-0.000222601	0.000617222	-0.000730096	-0.000222752
-0.976963	-0.0000186004	0.0000685322	0.0000628033
1.	0.0000685634	-0.000125002	-0.000119131
1.	0.0000627416	-0.000119029	-0.000113038
0.0000627416	1.	-0.976973	-0.976972
-0.000119029	-0.976973	1.	1.
-0.000113038	-0.976972	1.	1.

Appendix B Macro for diffraction measurement

```
def Ti_scan '
a2scan tth 24.0 31.0 th 12.0 15.5 350 -50000
'
def Ti_scan_opp '
a2scan tth 31.0 24.0 th 15.5 12.0 350 -50000
'
def Ti_scanL '
a2scan tth 24.0 31.0 th 12.0 15.5 350 -150000
'
def Ti_scanL_opp '
a2scan tth 31.0 24.0 th 15.5 12.0 350 -150000
'
def Ti_scanVL '
a2scan tth 24.0 31.0 th 12.0 15.5 350 -250000
'
def Ti_scanVL_opp '
a2scan tth 31.0 24.0 th 15.5 12.0 350 -250000
'
def psi_scanup '
umv chi 0
Ti_scan
umv chi 10
Ti_scan_opp
umv chi 20
Ti_scan
umv chi 30
Ti_scan_opp
umv chi 40
Ti_scan
umv chi 50
Ti_scan_opp
umv chi 60
Ti_scan
umv chi 70
```

```
Ti_scan_opp
umv chi 75
Ti_scan
umv chi 78
Ti_scan_opp
umv chi 80
Ti_scanL
umv chi 82
Ti_scanL_opp
umv chi 84
Ti_scanL
umv chi 86
Ti_scanL_opp
umv chi 88
Ti_scanVL
umv chi 89
Ti_scanVL_opp
'
def psi_scandown '
umv chi 89
Ti_scanVL
umv chi 88
Ti_scanL_opp
umv chi 86
Ti_scanL
umv chi 84
Ti_scanL_opp
umv chi 82
Ti_scanL
umv chi 80
Ti_scan_opp
umv chi 78
Ti_scan
umv chi 75
Ti_scan_opp
umv chi 70
Ti_scan
```

```
umv chi 60
Ti_scan_opp
umv chi 50
Ti_scan
umv chi 40
Ti_scan_opp
umv chi 30
Ti_scan
umv chi 20
Ti_scan_opp
umv chi 10
Ti_scan
umv chi 0
Ti_scan_opp
'
def Ti_azimuth '
umv phi 0
psi_scanup
umv phi 45
psi_scandown
umv phi 90
psi_scanup
umv phi 135
psi_scandown
umv phi 180
psi_scanup
umv phi 225
psi_scandown
umv phi 270
psi_scanup
umv phi 315
psi_scanup
umv phi 0
umv psi 0
an 40 0
'Ti_azimuth
```

Appendix C RBS simulation procedure for krypton profile for sample implanted at a fluence of $5x10^{15}$ Kr^{+}/cm^{2} fluence.

SIM Command: sim

SIM Command: la 1 th 1400 a comp ti 0.805 o 0.18 fe 0.015 /

SIM Command: species

Element name (/ to end)? kr 1 /

SIM Command: equation gaussian

Integral of Gaussian (dflt units = 1E15 atoms/cm^2): 5 /cm2

Depth of layer (Angstroms): 570 645

SIM Command: la 2 th 3000 a comp ti 0.86 o 0.14 /

SIM Command: la 3 th 20000 a comp ti 1 /

SIM Command: pl 1 ov 0

Automatic simulation .Created new stopping power table: 2 4.00 0.080 2.300

MSG: Increased SIM sublayer limit to 150

Fitting particle 4He for Z = 22 ... zsf ... max error: 0.61%

Fitting particle 4He for Z = 8 ... zsf ... max error: 1.18%

Fitting particle 4He for Z = 36 ... zsf ... max error: 0.48%

Fitting particle 4He for Z = 26 ... zsf ... max error: 1.35%

fwhm(0.000) . pileup(0.000) . all(0.078) . performed.

Appendix D Resonance scattering simulation procedure

a) unpolished sample implanted with $5x10^{15}$ Kr^{+}/cm^{2}

SIM Command: read scha0045
File: c:\rumpfiles\resonance050906\scha0045.rbs
Id: Unpolished implanted with 5e15 Kr (N4) @3.045 MeV
You called? sim
SIM Command: resread o165sigma(bis).txt
INFO: Overwriting old resonance table from c:\rumpfiles\resonance050906\o165sa(bis).txt
Resonance data: z1=2 m1=4 z2=8 m2=16 phi= 15.00 npt=206
SIM Command: la 1 th 800 a comp ti 0.640 o 0.35 fe 0.01 /
SIM Command: species
Element name (/ to end)? kr 1 /
SIM Command: equation gaussian
Integral of Gaussian(dflt units =1E15 atoms/cm^2): la 1 th 800 a comp ti 0.5 /cm2
Depth of layer (Angstroms): 570 645
SIM Command: la 2 th 1400 a comp ti 0.7 o 0.29 fe 0.005 /
SIM Command: la 3 th 3200 a comp ti 0.8 o 0.2 /
SIM Command: la 4 th 2000 a comp ti 0.9 o 0.1 /
SIM Command: la 5 th 2000 a comp ti 0.95 o 0.05 /
SIM Command: la 6 th 30000 a comp ti 1 /
SIM Command: pl 1 ov 0
Automatic simulation .Created new stopping power table: 2 4.00 0.121 3.487
Fitting particle 4He for Z = 22 ... zsf ... max error: 0.47%
Fitting particle 4He for Z = 8 ... zsf ... max error: 0.29%
Fitting particle 4He for Z = 26 ... zsf ... max error: 1.25%
Fitting particle 4He for Z = 36 ... zsf ... max error: 1.59%
fwhm(0.000) . pileup(0.000) . all(0.125) . performed.

b) polished sample implanted with $5x10^{15}$ K^+/cm^2

Your wish? read scha0046

File: c:\rumpfiles\resonance050906\scha0046.rbs

Id: Polished implanted with 5e15 Kr (P4) @3.045 MeV

Your wish? pl 1

Yes Master? sim

SIM Command: resread o165sigma(bis).txt

Resonance data: z1=2 m1=4 z2=8 m2=16 phi= 15.00 npt=206

SIM Command: la 1 th 300 a comp ti 0.6 o 0.4 /

SIM Command: species

Element name (/ to end)? kr 1 /

SIM Command: equation gaussian

Integral of Gaussian (dflt units = 1E15 atoms/cm^2): 5 /cm2

Depth of layer (Angstroms): 540 550

SIM Command: la 2 th 2500 a comp ti 0.9 o 0.1 /

SIM Command: species

Element name (/ to end)? kr 1 /

SIM Command: equation gaussian

Integral of Gaussian (dflt units = 1E15 atoms/cm^2): 5 /cm2

Depth of layer (Angstroms): 240 550

SIM Command: la 3 th 2000 a comp ti 0.95 o 0.05 /

SIM Command: la 4 th 30000 a comp ti 1 /

SIM Command: pl 1 ov 0

Automatic simulation .Created new stopping power table: 2 4.00 0.121 3.487

MSG: Increased SIM sublayer limit to 150

Fitting particle 4He for Z = 22 ... zsf ... max error: 0.47%

Fitting particle 4He for Z = 8 ... zsf ... max error: 0.29%

Fitting particle 4He for Z = 36 ... zsf ... max error: 1.59%

fwhm(0.000) . pileup(0.000) . all(0.032)

Appendix E $\sin^2\psi$ curves

a) $\phi = 0°$

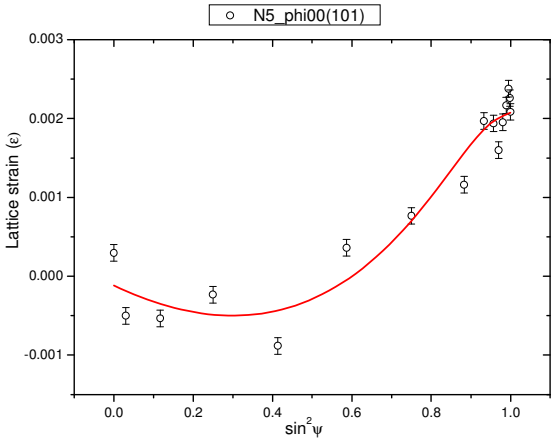

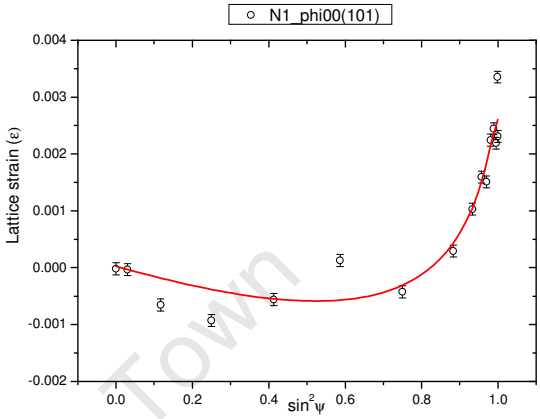

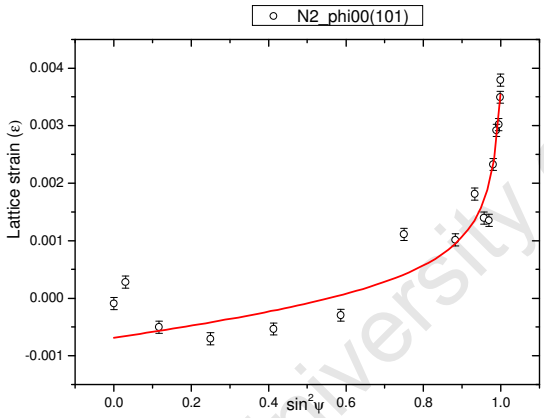

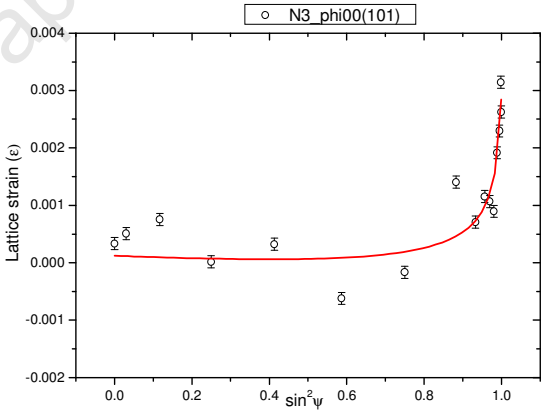

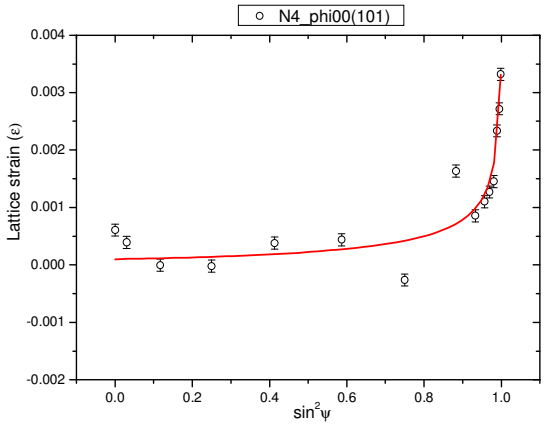

b) ϕ =90°

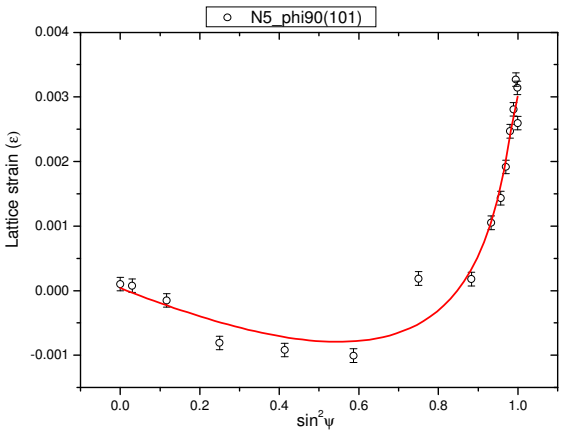

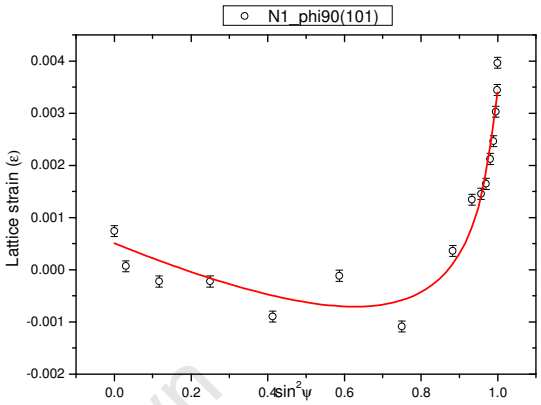

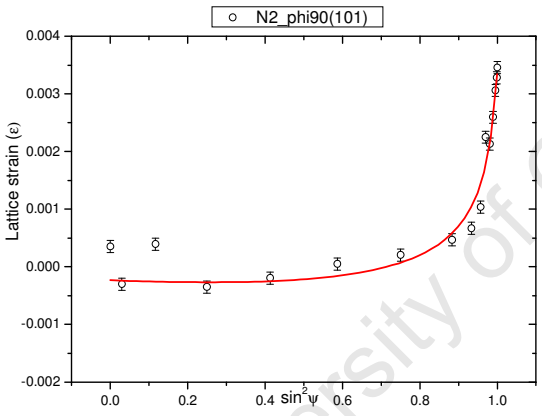

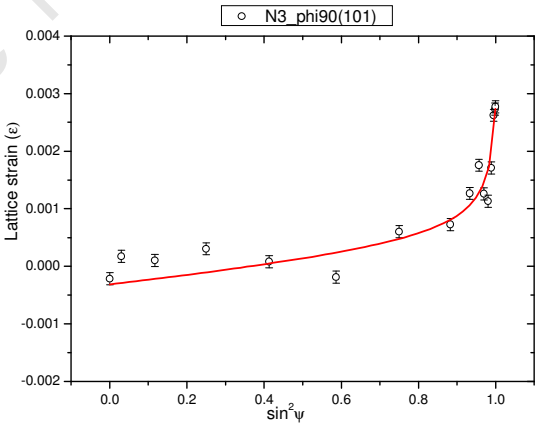

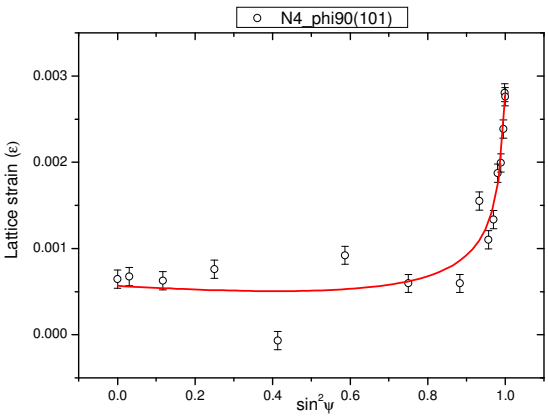

c) ϕ =180°

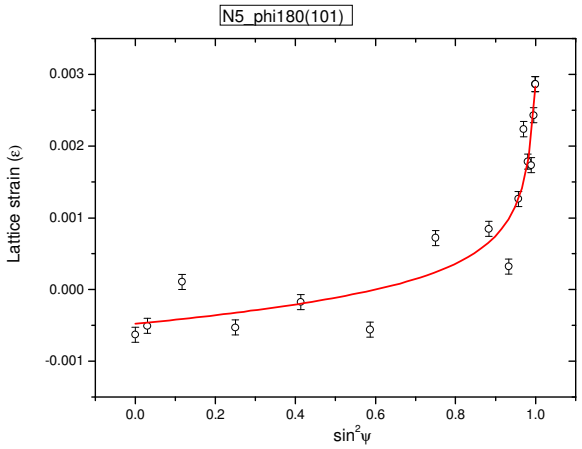

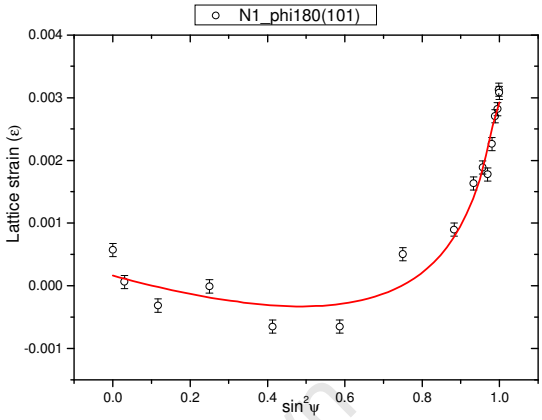

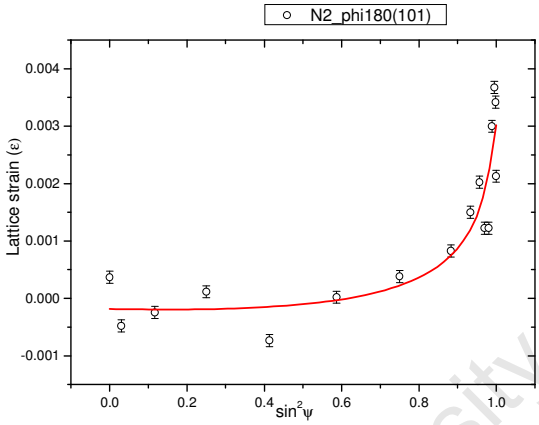

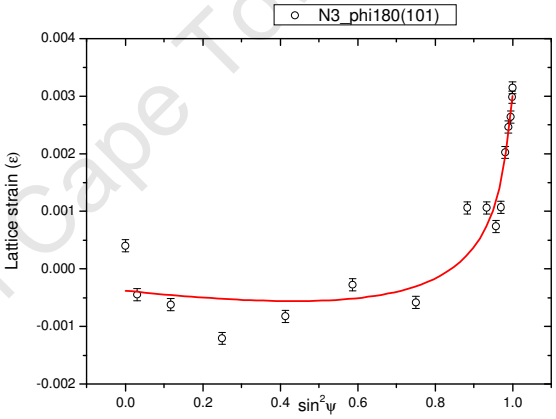

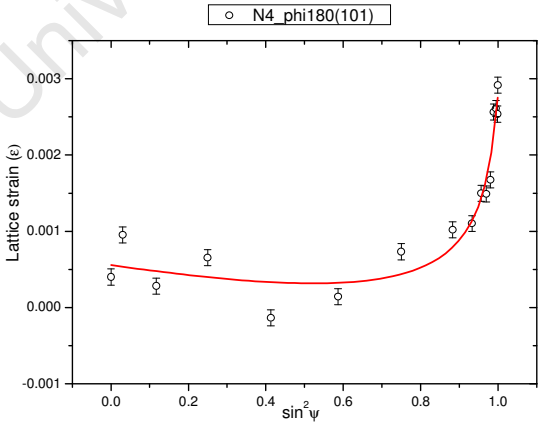

d) ϕ =225°

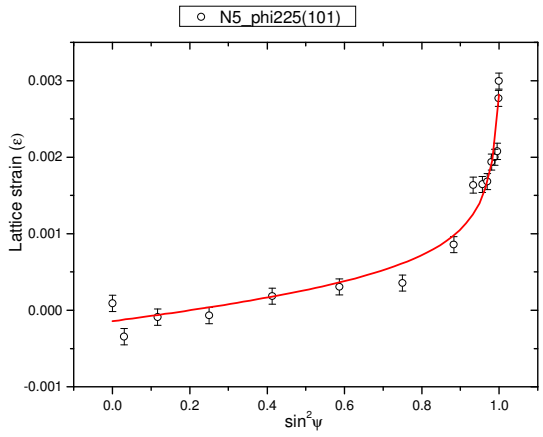

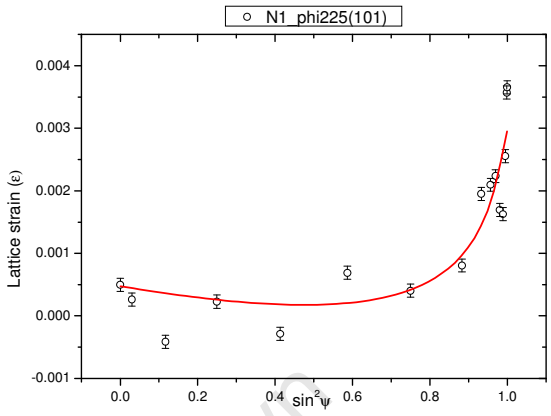

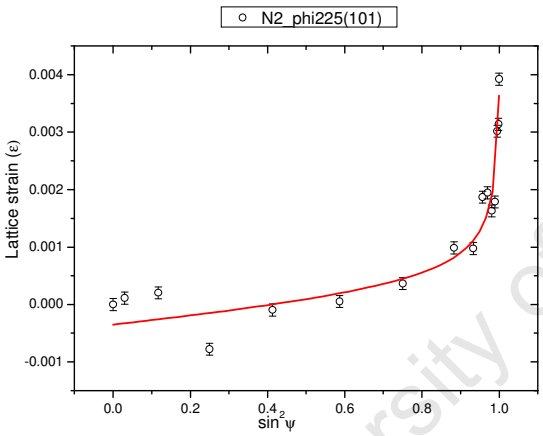

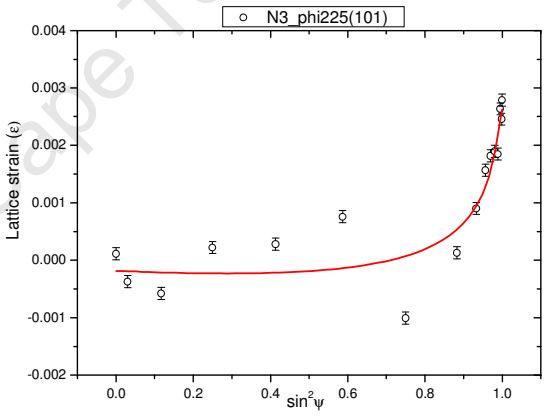

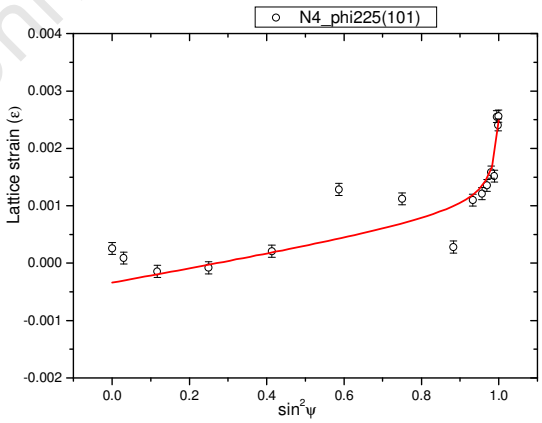

e) ϕ =270°

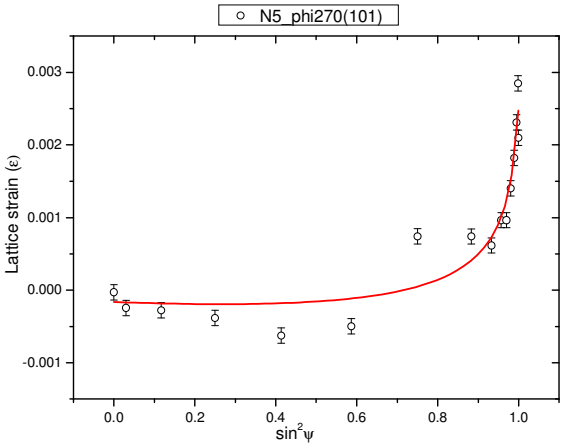

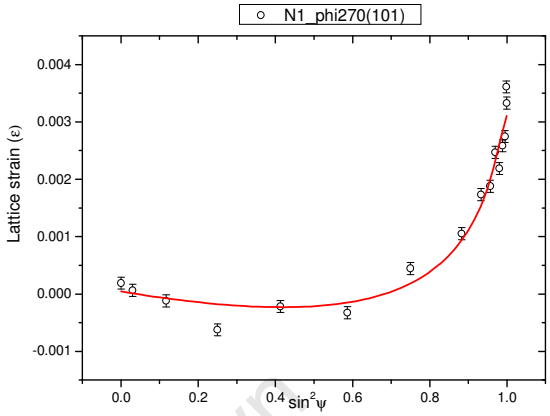

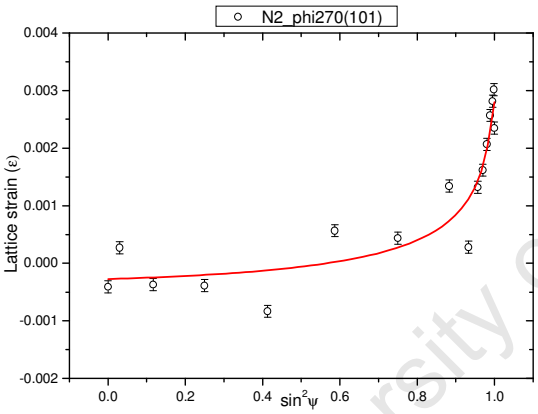

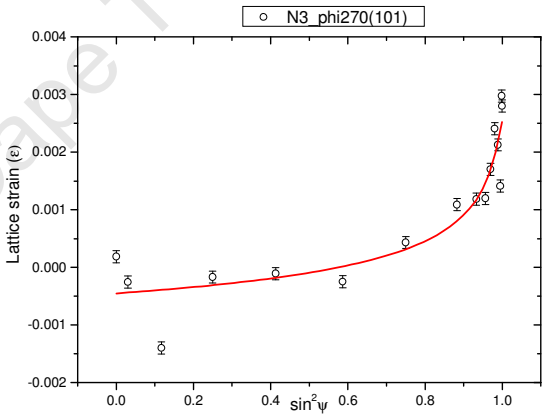

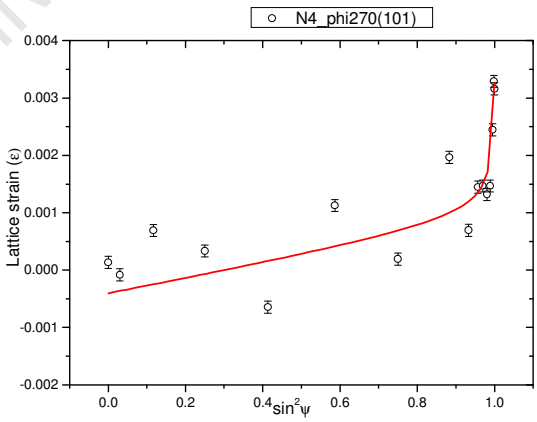

f) ϕ=315°

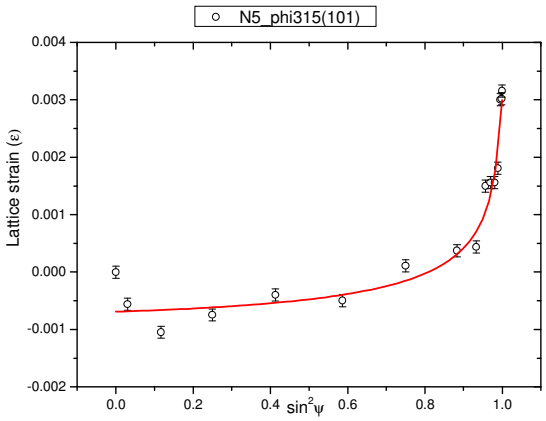

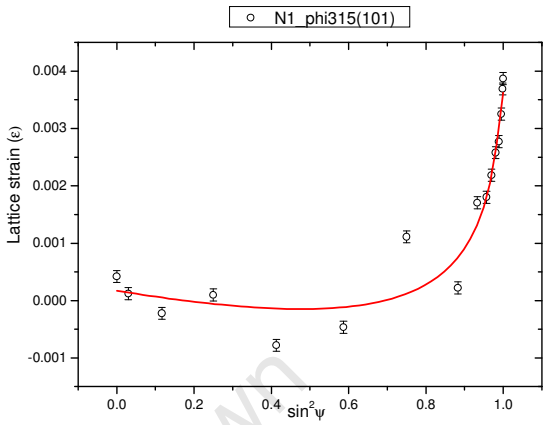

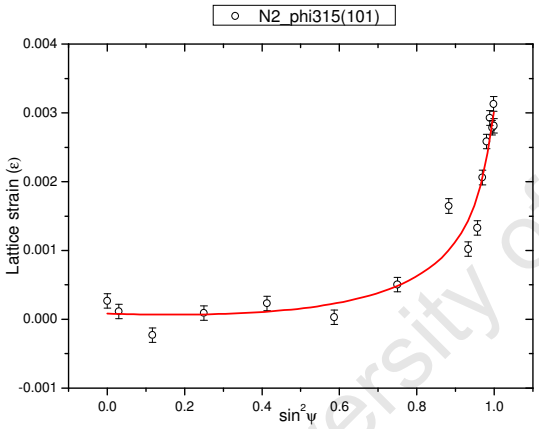

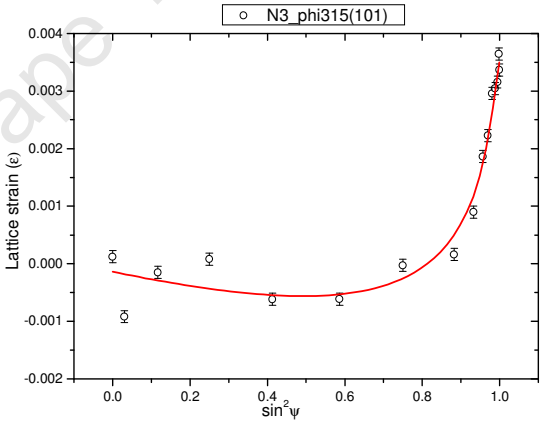

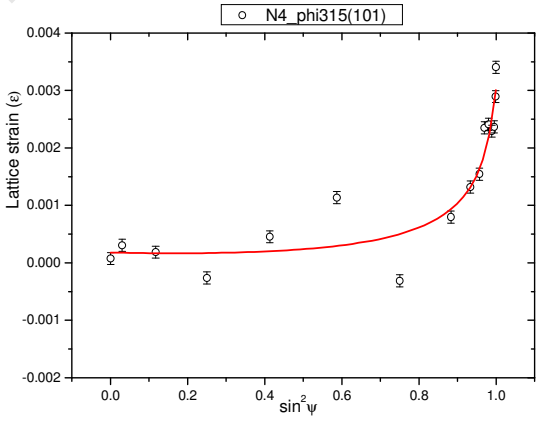

Appendix F Polar plots for the (100) reflection for unpolished samples

a) surface stress

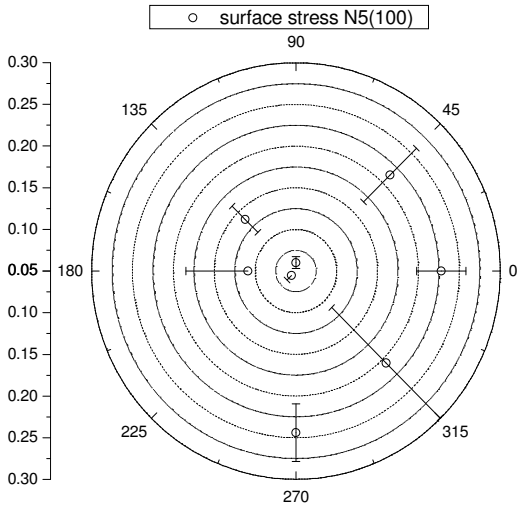

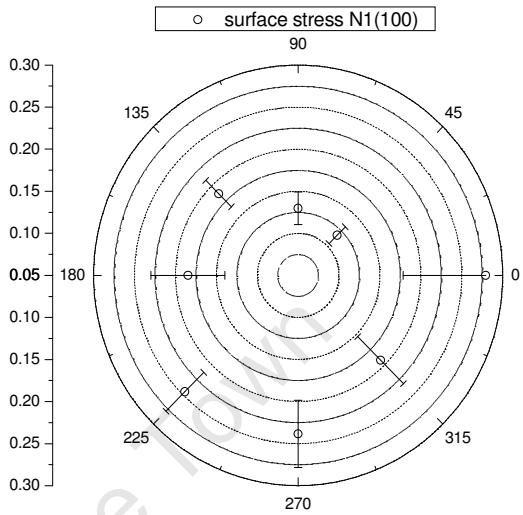

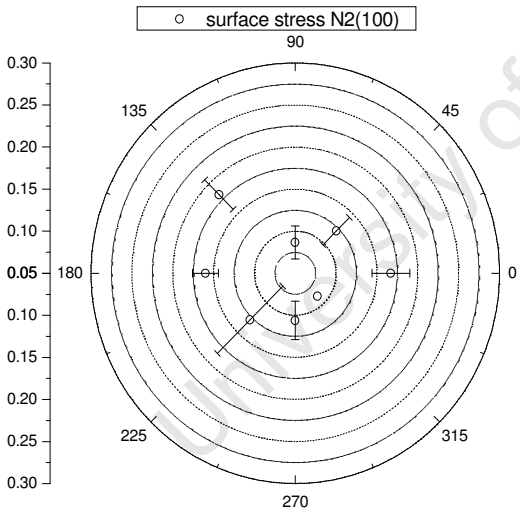

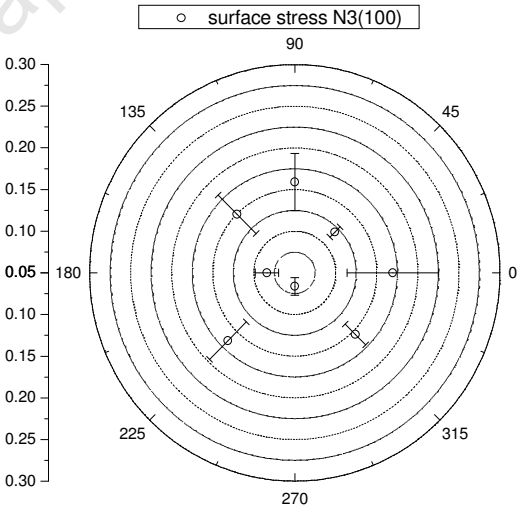

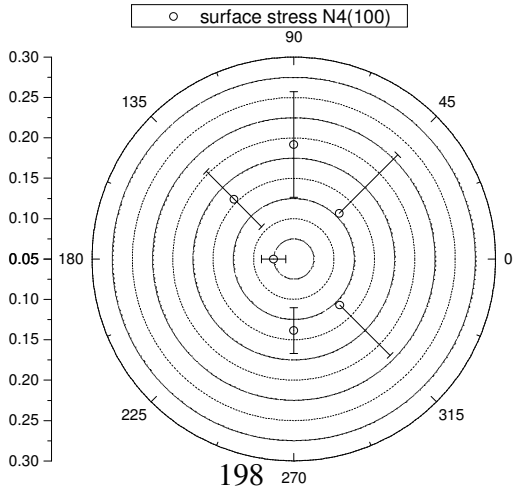

b) bulk stress